Characterization of HIV accessory protein interactions using NMR and microscale thermophoresis

Inaugural-Dissertation

zur Erlangung des Doktorgrades
der Mathematisch-Naturwissenschaftlichen Fakultät
der Heinrich-Heine-Universität Düsseldorf

vorgelegt von

Sameer Kumar Singh
aus Neu-Delhi

Düsseldorf, Mai 2012

aus dem Institut für Physikalische Biologie
der Heinrich-Heine Universität Düsseldorf

Gedruckt mit der Genehmigung der
Mathematisch-Naturwissenschaftlichen Fakultät der

Heinrich-Heine-Universität Düsseldorf

Referent: Prof. Dr. Dieter Willbold

Korreferent: PD. Dr. Bernd W. König

Tag der mündlichen Prüfung: 26th June, 2012

My Parents

Hyperboloids of Wondrous Light
Rolling for aye through space and time
Harbour those waves which somehow might
Play out gods holy Pantomime.

- Alan Turing's epitaph

Index

1 Introduction

1.1 Structure and genome organization of HIV-1 1
1.1.1 Human CD4 receptor and its role in HIV-1 infection 2
1.1.2 Virus protein U (VpU) 3
1.1.2.1 Downregulation of CD4 by VpU 4
1.1.2.2 VpU as a tetherin antagonist 5
1.1.3 Negative factor (Nef) 6
1.2 Membrane Proteins 6
1.3 Nuclear magnetic resonance (NMR) spectroscopy for studying protein-protein interactions 8
1.4 Thermophoresis 9
1.4.1 Thermophoresis and convection 10
1.4.2 Microscale thermophoresis 12
1.4.2.1 Theoretical Background 13
1.4.2.2 Instrumentation 15
1.4.2.3 Thermophoretic Signals 16
1.5 Nanodiscs 17

2 Materials and Methods 19

2.1 Materials 19
2.1.1 Chemicals, biochemicals and reagents 19
2.1.2 Enzymes and synthetic peptides 21
2.1.3 Bacterial Strains 21
2.1.4 Vectors 22
2.1.5 Media 23
2.1.5.1 Lysogeny broth (LB) 23
2.1.5.2 Minimal medium (M9) 23
2.1.6 Lipids 24
2.1.7 Standard laboratory instrumentation and miscellaneous equipment 25
2.1.8 Consumables 26
2.1.9 Nanotemper equipment 26
2.1.10 Chromatographic equipment 27
2.1.11 NMR instrumentation and equipment 27
2.1.12 Software 28

2.2 Methods 29
2.2.1 DNA methods 29
2.2.1.1 Plasmid isolation 29
2.2.1.2 DNA gel electrophoresis 29
2.2.1.3 DNA concentration determination 30
2.2.1.4 DNA sequencing 30
2.2.2 Protein analysis techniques 30
2.2.2.1 SDS-PAGE 30
2.2.2.2 Protein concentration determination 32
2.2.3 Protein expression and purification 33
2.2.3.1 Membrane scaffold protein (MSP) 33
2.2.3.2 CD4mut and HisUbiquitinCD4mut 34
2.2.3.3 CD4mut single cysteine mutants 36
2.2.3.4 Nef 36

2.2.3.5 VpUcyt 38
2.2.4 Preparation of nanodiscs 39
2.2.4.1 Preparation of lipids 39
2.2.4.2 Preparation of unloaded (empty) nanodiscs 40
2.2.4.3 Preparation of loaded nanodiscs 41
2.2.4.4 Separation of loaded from unloaded nanodiscs 41
2.2.5 Microscale Thermophoresis (MST) 41
2.2.5.1 Sample preparation 42
2.2.5.2 Capillary selection 42
2.2.5.3 Capillary scan 43
2.2.5.4 Supplementation with additives 43
2.2.5.5 Filtration 43
2.2.5.6 Laser power and laser intervals 44
2.2.5.7 Data analysis 44
2.2.6 NMR spectroscopy 45
2.2.6.1 Chemical shift 46
2.2.6.2 Different implementations of NMR spectroscopy 47
2.2.6.3 Heteronuclear single quantum coherence (HSQC) 47
2.2.6.4 Chemical shift perturbation (CSP) 48
2.2.6.5 Paramagnetic relaxation enhancement (PRE) 48
2.2.7 NMR sample preparation 48
2.2.7.1 CSP experiments 48
2.2.7.2 PRE experiments 49

3 Results 51

3.1 Protein production and modification 51
3.1.1 CD4mut, HisUbiquitinCD4mut and CD4 single cysteine mutants 51
3.1.2 Labelling of CD4 single cysteine mutants with MTSL 53
3.1.3 Nef 55
3.1.4 VpUcyt 55
3.1.5 MSP 57
3.2 Characterizing the CD4-VpU interaction using NMR 58
3.2.1 $^{1}H,^{15}N$ HSQC of VpUcyt 58
3.2.2 Measurement of chemical shift perturbations (CSPs) 59
3.2.3 Binding affinity of the CD4mut-VpUcyt interaction 60
3.2.4 Quantification of paramagnetic relaxation enhancement (PRE) 61
3.3 Nanodisc assembly 64
3.3.1 Nanodisc stability and storage 67
3.4 Microscale thermophoresis (MST) 68
3.4.1 Establishing a protocol to employ nanodiscs in MST studies 68
3.4.1.1 Nanodiscs adsorb to capillary walls 68
3.4.1.2 Strategies to prevent nanodisc adsorption 69
3.4.1.2.1 Supplementation with additives 69
3.4.1.2.2 Filtration of nanodiscs 71
3.4.1.3 Laser Power 72
3.4.1.4 Establishing parameters to study nanodiscs 73
3.4.1.5 Nanodisc storage 73
3.4.2 Interaction studies involving nanodiscs and MST 74
3.4.2.1 Interaction between Nef and HisUbiquitinCD4mut loaded POPC nanodiscs 74
3.4.2.2 Interaction between a p6 peptide and Vpr loaded DMPC-Atto 488 nanodiscs 75

4 Discussion 77

4.1 CD4-VpU interaction 77
4.1.1 Rationale for employing NMR 77
4.1.2 Chemical shift perturbation analysis (CSP) 78
4.1.3 Affinity of binding 81
4.1.4 Paramagnetic relaxation enhancement (PRE) analysis 81
4.1.5 Dynamic equilibrium of VpUcyt conformations and binding to CD4mut 85
4.1.6 Biological context 87
4.2 Microscale Thermophoresis (MST) 90
4.2.1 Rationale for employing nanodiscs in microscale thermophoresis (MST) 90
4.2.2 Protocol 90
4.2.2.1 Strategies to prevent nanodisc adsorption 91
4.2.2.2 Laser power 92
4.2.3 Interaction studies 94
4.2.3.1 Nef binding to CD4mut 94
4.2.3.2 Binding of the p6 peptide to Vpr 95

5 Summary 97
6 Appendix 100
7 Bibliography 108
8 Acknowledgement 116
9 Eidesstattliche Erklärung 117

1 Introduction

1.1 Structure and genome organization of HIV-1

According to the Baltimore convention, HIV-1 is a class VI virus, belonging to the family retroviridae, genus Lentivirus. Structurally, mature HIV-1 virons are ~145 nm in diameter (*1*). A mature virion contains a capsid protein (CA) enclosed core, that contains two copies of a single stranded RNA genome. The RNA molecules are bound to the nucleocapsid protein (NC). Additionally, the core contains the enzymes protease (PR), integrase (IN) and reverse transcriptase (RT), along with the accessory proteins viral infectivity factor (Vif), viral protein R (Vpr) and negative factor (Nef). The HIV-1 genome is ~9.7 kb in size, and consists of a positive single stranded RNA. The genome includes nine open reading frames that code for 15 proteins. Of these, the Gag, Pol and Env polyproteins are proteolysed into individual proteins common to all retroviruses (*2-4*). The Gag polyprotein precursor is proteolytically processed to generate the matrix (MA), CA, NC, and p6 proteins. Proteolytic cleavage of the Pol polyprotein yields the three enzymes, RT, PR and IN. RT reverse transcribes single stranded RNA to double stranded cDNA, PR facilitates cleavage of Gag, Pol and Env, while IN aids in integration of cDNA into the host genome. The env gene encodes a 30 amino acid signal peptide (SP), and two glycoproteins (gp); gp120, and gp41.

HIV-1 also encodes six accessory proteins. Transactivator of transcription (Tat) enhances the processivity of transcribing RNA polymerases, and increases production of viral mRNA ~100 fold. It may also enhance transcription initiation (*3*).
Regulator of virion expression (Rev) overcomes the default pathway in which mRNAs are spliced prior to nuclear export. This allows unspliced RNAs to be transported to the cytoplasm, where they are either packaged or translated (*3*).
The remaining accessory proteins, namely Vif, Vpr, Nef and viral protein U (VpU) have been the focus of extensive research in the recent past. It is now becoming increasingly clear that these proteins play important roles in ensuring efficient viral infectivity, survival and replication. They are primarily dedicated to evading various adaptive and innate immune responses (*5*).
A schematic representation of HIV-1 structure and genome organization is given in figure 1.

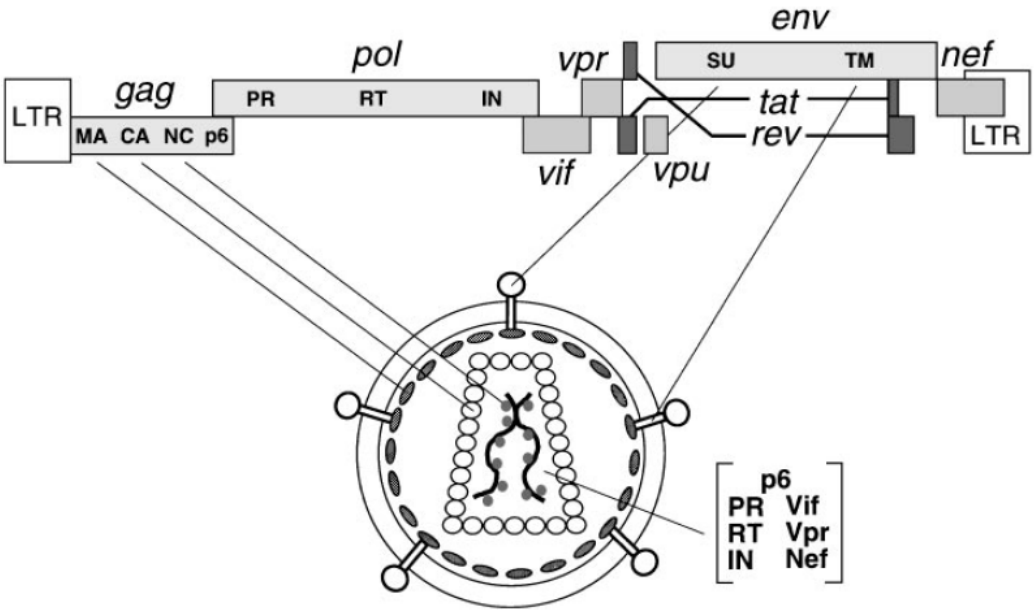

Figure 1: Pictorial representation of the structure and genome organization of HIV-1. Figure taken from (*3*), with permission of the publisher. LTR stands for long terminal repeat. SU and TM denote the gp120 and gp 41 proteins, respectively.

1.1.1 Human CD4 receptor and its role in HIV-1 infection

Cluster of differentiation 4 (CD4) is a 58 kDa transmembrane (TM) glycoprotein, that plays a vital role in the body's immune response. Structurally, it comprises four extracellular domains (D1-D4) that include the first 371 amino acids, followed by relatively short transmembrane (amino acids 372-395), and cytoplasmic (amino acids 396-433) domains.

CD4 is mainly expressed on the surfaces of helper T cells, macrophages, monocytes and dendritic cells. CD4 acts as a co-receptor for the T cell receptor (TCR) by directly interacting with MHC class II molecules on the surface of the antigen-presenting cell using its extracellular domain. The cytoplasmic domain of CD4 physically interacts with the p56Lck (leukocyte-specific protein tyrosine kinase), thereby bringing it in close proximity to the TCR complex. This activates a transmembrane signalling cascade that contributes to enhancing the T cell response and efficient T cell activation (*6, 7*). In the context of HIV-1 infection, CD4 acts as the primary receptor for virus entry into host cells (*8*). CD4 interacts with the gp120 viral envelope protein via the most amino terminal of its four extracellular immunoglobulin like domains (*9*).

In the most favoured model, CD4 binding induces conformational changes in the gp120 structure, enabling it to bind certain co-receptor molecules. One of the two

chemokine receptors, C-X-C chemokine receptor 4 (CXCR4), or C-C chemokine receptor type 5 (CCR5), usually serves as the co-receptor for HIV-1 entry. Gp120 binding also activates the viral transmembrane protein gp41, and together they facilitate fusion of the viral and host cell membranes (*10, 11*).

While the CD4 molecule is paramount for virus entry, its continual expression seems to be detrimental for efficient viral replication and spread. This may be due to the fact that a newly synthesized CD4 molecule is capable of retaining the entire Env precursor protein (gp160) in the ER through its high Env binding affinity, thereby preventing its (Env) processing and transport to the site of virus assembly (*12-15*). Additionally, the expression of CD4 at the cell surface also promotes superinfection of cells, which interferes with efficient release of progeny virions from the cell surface (*16*).

In order to overcome these effects, the virus devotes two of its accessory proteins, Nef and VpU, to the downregulation and degradation of CD4.

1.1.2 Virus protein U (VpU)

VpU was first discovered as the product of an open reading frame (ORF), referred to as U ORF, located between the first exon of the tat and env genes of HIV-1 (*17, 18*). VpU is an 81 amino acid membrane protein which features three specific sequence regions: The N-terminal transmembrane domain (I6-V26, notation reflects HIV-1 strain HV1S1) is followed by a short stretch rich in basic residues (Y27-K38) and the very acidic cytoplasmic tail (I39-L81). In a membrane or a membrane mimetic environment VpU adopts a transmembrane helix (helix 1) and two cytoplasmic helices (helices 2, 3) linked by a flexible loop (*19-21*). The exact length, position, and occupation of the cytoplasmic helices, in particularly helix 3, are sensitive to the buffer conditions and the type of membrane or membrane mimetic used (various detergents, trifluoroethanol, high salt buffer) (*20-23*). In the absence of membrane mimics and other special buffer components, the cytoplasmic domain of VpU remains unstructured (*21*). Figure 2 depicts the solution NMR structure of a section of the cytoplasmic domain of VpU, in the presence of membrane mimicking dodecylphosphocholine (DPC) micelles. The presence of two helices, separated by an interhelical linker is observed. The extreme C-terminal end is shown to form a tight loop (*21*).

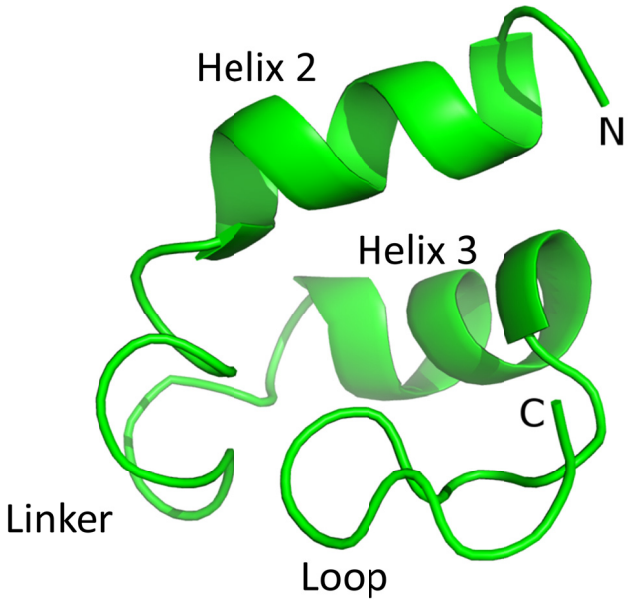

Figure 2: Solution NMR structure corresponding to amino acids 39-81 of the cytoplasmic domain of VpU, in the presence of membrane mimicking DPC micelles. The fractional helicities of helix 2 (residues 39-48) and helix 3 (residues 64-70) are 80% and 40%, respectively (*21*). Figure adapted from (*24*).

1.1.2.1 Downregulation of CD4 by VpU

Downregulation of CD4 by VpU employs a complex degradation pathway, initiated by physical binding of VpU to CD4. Mutational studies thus far have identified regions in the cytoplasmic domain of CD4 as instrumental in binding VpU. Specifically, CD4 residues 414-419 (LSEKKT), as well as a putative α-helical structure in the membrane proximal part of the cytoplasmic region of CD4 are critical for binding VpU (*25-28*). There is recent evidence that G390 in the transmembrane helix of CD4 contributes to VpU binding in a specific way (*29*). Binding of CD4 to VpU is followed by recruitment of the Beta-transducin repeat containing protein (βTrCP) by VpU at its $DS_PG\ \Phi\ XS_P$ motif (S_P-phosphorylated serine, Φ-hydrophobic residue, X-variable residue), forming a CD4-VpU-βTrCP ternary complex. The CD4-VpU-βTrCP complex triggers the recruitment of an E3 ubiquitin ligase, thus facilitating the trans ubiquitination, and eventual degradation of CD4 (*30*).

1.1.2.2 VpU as a tetherin antagonist

Tetherin has been recently identified as the cellular factor responsible for inhibition of HIV-1 particle release (*31, 32*). Tetherin prevents viral release by directly cross linking virions to host cell membranes (*33, 34*). The exact structural mechanism by which it carries out this function, however remains unclear. The VpU-mediated antagonism of tetherin is dependent on the physical binding of the two proteins, most likely via their transmembrane domains (*35-39*).

One model suggests that VpU degrades tetherin via the E3 ubiquitin ligase pathway, akin to VpU induced CD4 degradation (*35, 40*). Another model suggests that VpU causes intracellular sequestration of tetherin (*41, 42*).

Structurally, tetherin is a glycosylated type II integral membrane protein of between 28 and 36 kDa. Topologically, it consists of a short N-terminal cytoplasmic tail followed by a TM anchor, a central extracellular domain, and a putative C-terminal glycophosphatidylinositol (GPI)-linked lipid anchor (*43, 44*). X-ray crystallography showed that the extracellular domain of tetherin forms a long parallel coiled coil, stabilized by three intermolecular disulphide bonds (*45-48*). A schematic of tetherin secondary and tertiary structure is given in figure 3. Tetherin is alternately known as CD317 or the bone marrow stromal antigen 2 (BST2).

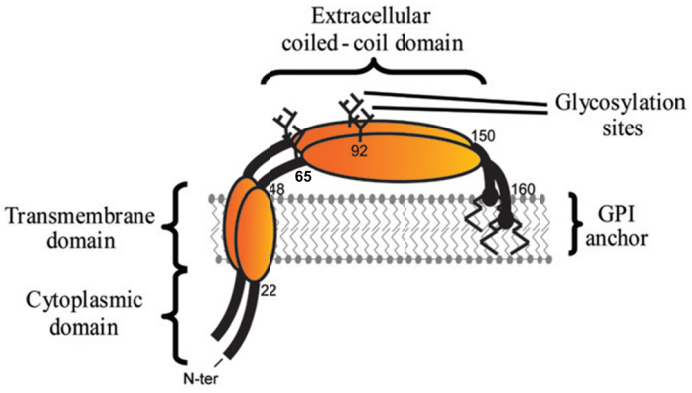

Figure 3: Schematic representation of a secondary and tertiary structure model of tetherin. The protein functions as a parallel dimer. A single protein consists of an N-terminal cytoplasmic domain, a TM α-helix, a coiled coil extracellular domain, and a C-terminal GPI-anchor. Glycosylation sites at positions 65 and 92 are also shown. Figure reproduced from (*49*), with permission of the publisher.

1.1.3 Negative factor (Nef)

Nef is an HIV-1 accessory protein, with a molecular weight of ~25 kDa. It has a wide range of functions that ensure efficient viral replication and pathogenicity. Nef associates with membranes, a property which can be attributed to its N-terminal myristoylation, as well as a stretch of N-terminal basic residues which may electrostatically interact with acidic phospholipids (*50*).

Nef enhances viral replication and accelerates the immune evasion of infected cells by manipulating transport as well as signalling pathways (*51*). Nef also has a strong influence on cytoskeletal dynamics, which may be linked to its role in intracellular vesicle transport, signal transduction and production of infectious progeny (*52*). As already mentioned, Nef plays a role in downregulation and degradation of CD4 molecules. Nef removes mature CD4 molecules from the cell surface by enhancing their endocytosis via a pathway involving clathrin and AP2 (*49, 53*). Internalized CD4 is then delivered to the multivesicular body pathway, followed by eventual degradation in lysosomes (*54*).

1.2 Membrane Proteins

Typical biological membranes contain many types of proteins, some inserted into the bilayer, and some associated only with the surface. They perform a wide variety of functions, like nutrient transport, cell adhesion, cell signalling and energy transduction, to name a few. Membrane proteins can be classified as follows:

Peripheral membrane proteins

Peripheral membrane proteins bind the surface of the membrane via electrostatic interactions, either with charged lipids or charged groups on other proteins. In addition to electrostatic interactions, they may interact with acyl chains via hydrophobic interactions. Typically they are weakly bound to membranes. The classic example for peripheral membrane proteins is cytochrome c, which binds anionic lipids using its cluster of lysine residues (*55*).

Lipid anchored proteins

Lipid-anchored proteins carry covalently attached lipid-moieties, thus enabling them to associate with membranes. Examples of such moieties include fatty acids, terpenes and glycosylphosphatidylinositol (GPI). The process of covalent lipid attachment is known as lipidation. Often, for lipidation with long chain fatty acids, the acyl chains may be myristoyl groups in amide linkages to glycine residues, or palmitoyl groups linked to cysteines (*56*). The HIV-1 accessory protein Nef is an example of an N-terminally myristoylated protein.
GPI-linked proteins are normally components of the plasma membrane, but they can also be found in internal membranes after endocytosis. GPIs consist of a phosphatidylinositol group linked to a short carbohydrate, which in turn is covalently attached to the carboxyl terminal residue of a protein through phosphoethanolamine.
Examples include CD317 (tetherin), CD59 (protectin), and the scrapie prion protein, to name a few.

Integral membrane proteins

Integral membrane proteins are permanently attached to the membrane, and can only be removed by disrupting the membrane. They usually have at least one transmembrane (TM) peptide segment. They are further classified depending on the nature of the TM segment. Bitopic proteins have a single TM segment, while polytopic proteins have more than one. Additionally there are monotopic proteins that insert into the membrane but do not span it. Examples include the bitopic human CD4, that has a single transmembrane α helix, while the polytopic bacteriorhodopsin has seven transmembrane α helices.

1.3 Nuclear magnetic resonance (NMR) spectroscopy for studying protein-protein interactions

In recent years, NMR spectroscopy has been widely applied in the study of protein-protein interactions (PPIs). Recent advances in instrumentation as well as the development of methods that provide long-range distance information have made NMR particularly useful in the study of weak PPIs, which may otherwise be difficult to detect.

Complementary techniques like X-ray crystallography may not be particularly useful in this regard, due to difficulties in crystallizing weakly interacting protein complexes. This may especially be the case for interactions involving unstructured proteins (several viral proteins).

In comparison to existing biophysical methods, NMR offers a much more detailed insight into PPIs. Using NMR, it is possible to identify individual interacting amino acids involved in the PPI. It also provides information on binding topology, allosteric processes as well as binding strength. In the presence of a suitable membrane mimetic, the technique can also be used for interactions involving membrane proteins. This work employs two complementary NMR methods, chemical shift perturbation (CSP) and paramagnetic relaxation enhancement (PRE) to study binding between a detergent solubilised CD4 fragment and part of the cytoplasmic domain of VpU.

Ligand binding usually affects the electron current density in the immediate vicinity of the binding site, resulting in localized chemical shift changes for nuclear spins of the binding partner. Such changes are referred to as chemical shift perturbations (*57*).

Paramagnetic relaxation enhancement is routinely used to provide long-range intra- or intermolecular distance information of up to 20 Å (*58, 59*). This involves attaching paramagnetic probes to strategic positions on one of the two interacting partners. Spatial proximity is then detected as distance-dependent line broadening and intensity loss of NMR signals, particularly for protons.

1.4 Thermophoresis

Thermophoresis is the movement of molecules along temperature gradients. Thermophoresis in liquid mixtures was first observed and reported by Carl Ludwig in 1856 (*60*). Charles Soret further understood the process by his work with solutions of NaCl and KNO_3 in differentially heated pipes (1879) (*61*). In 1938 Clusius and Dickel developed an approach to separate different components of a gas mixture, by coupling thermophoresis and convection (*62*). This is known as a thermogravitational column. Thermophoresis is alternatively known as thermal diffusion, or the Ludwig-Soret effect (*63*).

As stated above, thermophoresis is the directed movement of particles subjected to a temperature gradient. The generated temperature gradient produces a molecule drift that is either directed toward or away from the heated spot. Movement away from the heated region is termed positive thermophoresis (thermophobic), while movement toward it is termed negative thermophoresis (thermophilic) (*63-65*). Such movement is usually particle specific.

We now know that thermophoresis plays a role in several global processes. For example, thermal diffusion is involved in natural transport processes like thermohaline convection in oceans, and component segregation in the earth's mantle (*66, 67*). Recent studies suggest that thermophoretic movement in combination with laminar convection may together have played a role in molecular evolution near hydrothermal vents (*68*). Recent work has focussed on using thermophoresis for the analysis of biomolecular interactions (*65, 69-71*). Specifically, the technique termed microscale thermophoresis (MST) has been successfully applied in the study of DNA-protein and protein-protein interactions (*65, 72*). Our work is aimed at using MST in membrane protein interaction studies.

1.4.1 Thermophoresis and convection

The combination of thermophoresis and convection is known as a thermogravitational column, and is an effective approach for the separation of molecules (*73, 74*). It was originally developed by Clusius and Dickel (1938) to collect molecules in gases (*62*). It has since been effectively applied to the separation of molecules in liquid mixtures as well (*75*). The working of such a thermogravitational column is shown in figure 4(A). It consists of a vertically oriented column, with one heated vertical side. The heating results in a lateral thermal gradient across the channel. The chosen (or described) geometry in concert with the different temperatures of the two vertical walls and gravitational forces establish a convective flow. The convection results from the rising of the heated fluid and sinking of the cooler fluid. It sets up a bidirectional flow of fluid, perpendicular to the thermal gradient. Simultaneously, the thermal gradient causes molecules in the liquid to undergo thermophoresis. Molecules undergoing positive thermophoresis will migrate away from the heated surface, and concurrently occurring convection will cause them to move toward the bottom of the column. In this manner, a combination of thermophoresis and convection can be used in the effective separation of molecules in solution. A simple example is given in figure 4(B), where a thermogravitational column was used for the concentration of a small dye, 8-Hydroxypyrene-1,3,6-trisulfonic acid, trisodium salt (HPTS) (*75*). Applying a thermal gradient (ΔT) of 30 K for 24 h resulted in accumulation of the dye at the bottom of the column with a bottom to top HPTS concentration gradient of ~800 fold (*75*).

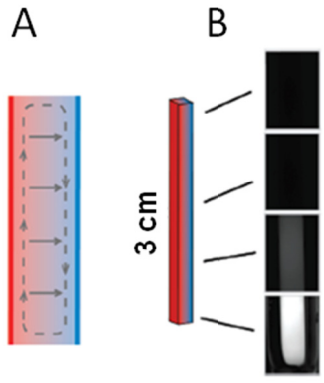

Figure 4: A) Thermogravitational column showing the coupling of convective flow (dashed arrows) and thermophoresis (solid arrows). The red coloured column wall signifies heating. B) Fluorescence microscopy images showing a strong concentration gradient of the dye HPTS, from top to bottom. Column length is 3 cm. Figure adapted from (*75*), with permission of the publisher.

In the context of biomolecules, such molecular separation was first applied to plasmid DNA (*76*). Recent studies also suggest that thermal gradients may have played a role in prebiotic evolution. Micrometer sized pores in hydrothermal vents, wherein the pore system is sandwiched between the hot vent interior and cooling oceans outside may have facilitated the accumulation and replication of biomolecules, as has been demonstrated with nucleic acids (Figure 5A) (*73, 75*). This concept may also apply to the formation of prebiotic membranes, as recent work has shown that thermal gradients can be employed to concentrate dilute fatty acid solutions to amounts at which they self-assemble into vesicles (Figure 5B). The vesicles also exhibited the ability to encapsulate DNA oligomers (*75*). These results support current protocell models which are based on self-replicating, fatty acid-encapsulated nucleic acid polymers (*77*).

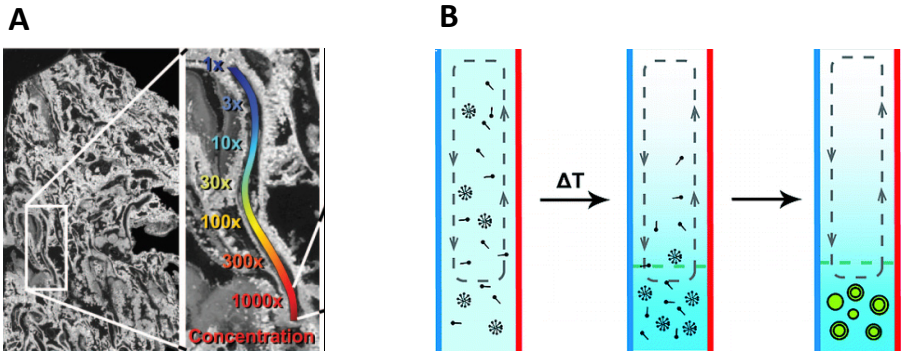

Figure 5: A) Submarine hydrothermal vent. If subjected to a horizontal thermal gradient of 30 K, a 1,200-fold accumulation of single nucleotides is expected at the bottom of a vertical pore. Figure taken from (*73*), with permission of the publisher. B) Schematic representation of thermal diffusion-induced concentration of oleic acid. The initial concentration of oleic acid is below the critical aggregate concentration (cac), thus preventing the formation of vesicles. The application of a thermal gradient results in thermophoresis and convection which concentrates the solution, until the assembly of vesicles is seen in regions where the cac is exceeded. Figure taken from (*75*), with permission of the publisher.

Such separation of molecules in thermal gradients is also influenced by other factors.

Salt concentration is an important parameter affecting thermophoresis and convection. For example, trapping of DNA molecules was abolished in the presence of high salts (500 mM NaCl or 20 mM $MgCl_2$) (*78, 79*). Chamber thickness is another influencing parameter. Thicker chambers increase the speed of convection, and thus enhance molecule trapping. Studies showed that chamber thicknesses of 10, 20 and 30 µm exhibited convection speeds of 0.055, 0.22 and 1.5 µm/s, respectively (*78*).

Chamber thickness has a greater influence on slow diffusing molecules. For example, thermophoretic depletion in combination with convective flow for a 50,000 bp DNA solution in a 50 µm thick chamber is quickly transformed to accumulation of DNA along with an eventual concentration enhancement. However, on repeating the experiment with a 50 bp DNA solution, only thermophoretic depletion was observed (*78*). Thus, using the right combination of the aforementioned parameters (chamber thickness, salt concentration, diffusion coefficient) temperature gradients offer a valuable alternative for molecule trapping.

Apart from convective flow in vertical columns, moving temperature gradients have also been used to generate and control flow patterns in thin horizontal liquid films. Studies have attributed these results to changes in the viscosity of liquid molecules, brought about by the temperature gradient (*74*).

1.4.2 Microscale thermophoresis (MST)

MST is a recently developed technology that uses the principle of thermophoresis to study biomolecular interactions. It employs infrared lasers for the creation of microscopic localized temperature fields. This application of thermophoresis to biomolecules was pioneered at the Biophysics Department of the Ludwig Maximilian University Munich (*63, 80*), and is now being commercialized by Nanotemper technologies, Munich, Germany (*65, 70*).

MST is highly sensitive, since it depends on changes in the size, charge and hydration shell of molecules (*65, 70*). For strong interactions (K_D in the nM to low µM range) it requires very low sample concentrations. It also measures interactions in free solution (no immobilization required). Additionally, it is relatively quick, with binding affinities measured in as little as 10 minutes (*65*).

It thus provides some advantages over existing methods for the characterization of biomolecular interactions.

Surface plasmon resonance (SPR) can measure dissociation constants in the nM to mM range (*81*). It however requires the covalent coupling of one of the molecules to a surface, which may adversely affect, abolish or modify binding. SPR also suffers from artefacts like rebinding and concentration depletion (*82*). In comparison, MST offers the advantage of measuring interactions in free solution.

Isothermal titration calorimetry (ITC) is probably the only true label-free method available for biomolecular analysis. It however requires high sample concentrations

(up to mg/ml), and sample volumes are considerably larger than in other methods. Also, interactions with a very small or no change in binding enthalpy cannot be studied with ITC. The acquisition of MST data representing an entire binding isotherm normally consumes less than a hundred microlitres of sample. For high affinity reactions, the technique requires only nanomolar concentrations of sample.

FCS (Fluorescence correlation spectroscopy) and FA (Fluorescence anisotropy) both measure changes in the diffusion properties of fluorescently labelled molecules. Both methods are capable of detecting high affinity binding. Additionally, their ability to measure single molecule properties gives them an advantage over other bulk methods. But to work effectively, there must be large changes in size that occur when the two proteins bind, as a modest size change will only have a negligible influence on the hydrodynamic radius (and hence diffusion). For example, to change its hydrodynamic radius by a factor of two, a globular protein must increase its mass by a factor of 8, due to the third root scaling of radius with mass (*65*). Alternately, the experiments can be carried out by labelling the smaller molecule, but this approach runs the risk of changing the binding properties. In comparison, MST is usually more sensitive, as it detects changes in size, charge and the hydration shell of molecules.

1.4.2.1 Theoretical Background

The thermodiffusive drift velocity $\vec{v}$ of a molecule in a temperature gradient **(∇T)**, scales linearly with the strength of the gradient and a proportionality constant $\mathbf{D_T}$ (*65, 80*). Thus,

$$\vec{v} = -D_T \nabla T$$

$\mathbf{D_T}$ is known as the thermal diffusion coefficient, or thermophoretic mobility.

In the steady state, thermodiffusion is counterbalanced by ordinary diffusion, i.e. the component of molecular diffusion which acts independently of the presence of a temperature gradient. Ordinary diffusion is reflected by the diffusion coefficient **D** of the molecule. The steady state is characterized by a vanishing net drift current density of molecule flow $\vec{j}$ throughout the sample. If the molecule concentration is low (low nanomolar range) the following steady state approximation applies (*80*):

$$\vec{j} = -cD_T \nabla T - D \nabla c = 0$$

Here, **c** is the position dependent concentration of the considered molecule and ∇c symbolizes the molecule concentration gradient.

Integration of the above equation with temperature independent parameters $\mathbf{D_T}$ and **D** yields the following steady state concentration distribution, which is valid for small temperature differences $\Delta\mathbf{T}$ only:

$$c_T(\vec{r}) = c_0 \exp(-S_T \Delta T(\vec{r}))$$

where $\mathbf{c_0}$ is the bulk concentration of the molecule in the sample, and $\boldsymbol{c_T}(\vec{\boldsymbol{r}})$ symbolizes its steady state concentration in a voxel characterized by a temperature that is $\Delta\mathbf{T}$ above the ambient temperature of the bulk sample. The Soret coefficient $\mathbf{S_T}$ is defined as:

$$S_T = \frac{D_T}{D}$$

Usually, thermophoresis results in a depletion of molecules in the heated spot, i.e. $\mathbf{c_T}$ is lower than the nominal concentration $\mathbf{c_0}$ of the studied molecule in the sample. This scenario is characterized by positive values of both the thermophoretic mobility $\mathbf{D_T}$ and the Soret coefficient $\mathbf{S_T}$, and is referred to as thermophobic behaviour. However, depending on the properties of individual molecules, a concentration increase may occur at the elevated temperature. This is referred to as thermophilic behaviour.

1.4.2.2 Instrumentation

Thermophoresis experiments have been conducted using instruments developed by Nanotemper Technologies, Munich, Germany.

The setup consists of an infrared (IR) laser, coupled to the path of fluorescence using an IR dichroic mirror (*65*). This setup ensures a precise observation of thermophoresis, since the IR and visible optics are well aligned. Samples are loaded into glass capillaries. Focussing the IR laser onto the sample produces a localized spatial temperature distribution in the order of a few micrometers (Figure 6). Restricting this distribution to the micrometer scale enables quantification of the samples thermophoretic properties in under 30 seconds. Switching on the laser produces a fast temperature jump (within 1 second), during which a new steady state temperature will be established in the heated spot (1 to 10 K above the temperature in the bulk of the sample; exact value will depend on the IR laser power) (*69, 83*).

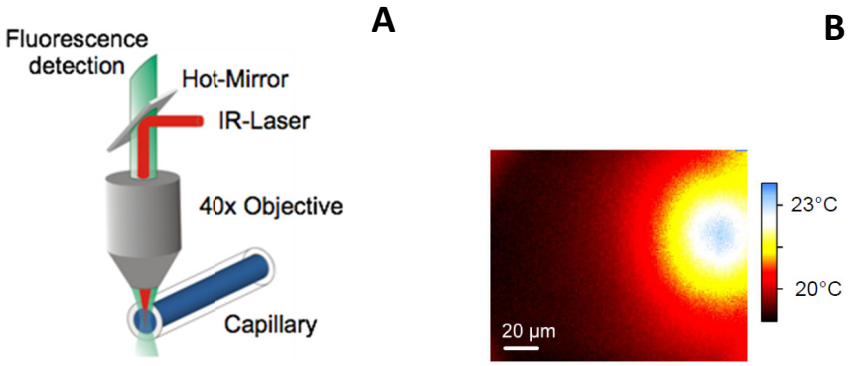

Figure 6: Setup for recording microscale thermophoresis. A) Coupling the IR laser to the fluorescence path ensures a precise observation of thermophoresis. B) Focussing the IR laser onto the sample induces a localized spatial temperature distribution. Figure adapted from (*84*), with permission of the publisher.

1.4.2.3 Thermophoretic Signals

Molecules are initially distributed evenly, and diffuse freely in solution. On switching on the laser, the molecules experience a thermophoretic force in the temperature gradient, and typically move out of the laser spot (positive thermophoresis), thus lowering the measured fluorescence signal. This molecule flow is eventually counterbalanced by ordinary mass diffusion, causing the molecules to reach a steady state. After turning off the laser, the molecules diffuse back to a homogeneous distribution. A single thermophoretic signal (also referred to as a 'time trace') displays a host of information, namely; the fluorescence signal before turning on the laser, fast temperature dependent changes in fluorescence intensity (T-Jump), thermophoresis, and lastly, back-diffusion. A typical thermophoretic signal is depicted in figure 7.

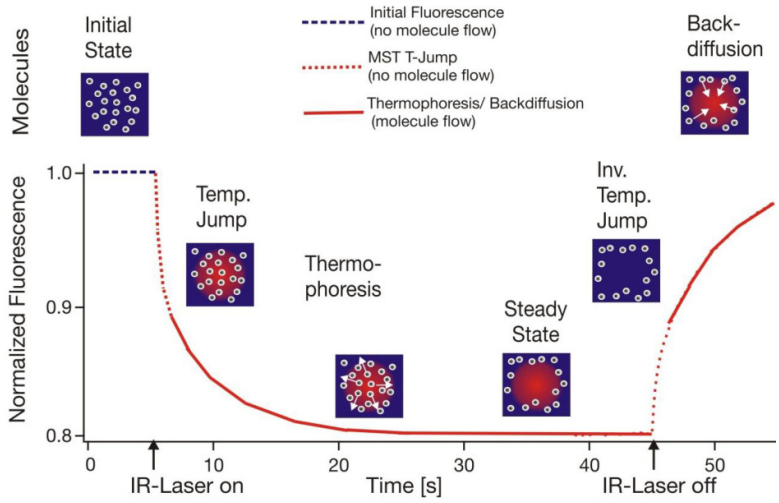

Figure 7: A typical thermophoretic signal showing positive thermophoresis. From left to right, it begins with the initial state of the molecules before the laser is switched on. This is followed by switching on the IR laser and the consequent temperature jump. The magnitude of the T jump is directly proportional to the laser power. The molecules then experience positive thermophoresis (moving away from the heated spot), which is eventually counterbalanced by mass diffusion, resulting in a steady state. Finally, switching off the IR laser abolishes the thermal gradient, thus causing the molecules to undergo an inverse temperature jump accompanied by back-diffusion, and return to their initial state. Figure taken from (*84*) with permission of the publisher.

In a typical binding experiment, the concentration of the fluorescently labelled molecule is kept constant, while that of its unlabelled binding partner is progressively increased in each subsequent capillary. The magnitude and nature of the measured signal is thus directly dependent on the concentration of both the bound complex and the remaining unbound fluorescent binding partner. Measured differences in the thermophoretic signals are thus indicative of binding, and can be used to compute the dissociation constant of the interaction, provided that the free and bound labelled molecules have distinct thermophoretic behaviour.

1.5 Nanodiscs

Difficulties in studying membrane proteins are central to biophysics, primarily due to inadequate membrane mimetics. Suitable mimetics preserve the biological structure of the protein, while not inhibiting or modifying ligand binding. Detergent micelles are the most commonly used mimetics for studying membrane proteins. Detergents are amphipathic molecules consisting of hydrophobic and hydrophilic regions. They attach to hydrophobic regions on membrane proteins, thus facilitating their solubilization. However, they are also known to adversely modify the structure and dynamic properties of proteins. Studies involving detergent micelles may thus be biologically inaccurate (*85-87*). Liposomes allow the study of membrane proteins in their natural lipid bilayer environment. Liposomes are assemblies of phospholipids arranged in uni- or multilamellar layers. Incorporation of proteins into liposomes yield structures called proteoliposomes. However, liposomes often exhibit inhomogeneity in size, and consequently protein distribution. They also tend to fuse with other membranes (*88, 89*). Additionally, soluble regions of the proteins that are oriented towards the inner aqueous compartment of liposomes are inaccessible to ligands, and thus cannot be utilized in interaction studies.

Nanodiscs are self-assembled proteolipid particles, wherein two copies of a recombinant membrane scaffold protein (MSP) clasp a lipid patch, and seal the hydrophobic edge of the bilayer from water (*85, 90*). The dimensions of the nanodisc particles are dependent on the MSP variant used (*90, 91*). So far, MSP variants derived from human and zebrafish apolipoproteins have been successfully employed in nanodisc assembly. For nanodisc assembly, we have employed an MSP variant lacking the first 43 N-terminal amino acids of human apolipoprotein A-I. The resulting nanodiscs have a diameter of ~10 nm and a lipid dependent thickness of ~5 nm (*90*). Nanodiscs offer substantial advantages over other membrane mimetics. Unlike detergents, they offer a biological environment that should maintain native protein structure, function, and dynamics. Recent studies on the receptor tyrosine kinase

EGFR (epidermal growth factor receptor), and on CYP3A4 (cytochrome P450 3A4) demonstrated that these proteins retain their activity after insertion into nanodiscs (*92, 93*). In contrast to liposomes, nanodiscs allow access to both sides of the membrane. They are not known to fuse over time. Protein loaded discs can also be separated from unloaded ones via suitable affinity tags, thus ensuring sample homogeneity. In a relatively short period, nanodiscs have been applied in biophysical studies of membrane proteins using a broad variety of techniques, ranging from structural investigations by NMR and electron microscopy, to interaction studies using surface plasmon resonance (SPR) (*85, 94-97*).

2 Materials and methods

2.1 Materials and instrumentation

2.1.1 Chemicals, biochemicals and reagents

Standard chemicals not listen in table 1 were purchased either from Fluka (Neu-Ulm), Merck (Darmstadt), Roth (Karlsruhe), or Sigma-Aldrich (Munich). All standard chemicals were of reagent grade.

Table 1: List of chemicals used

Chemical	Supplier
(1-oxyl-2,2,5,5-tetramethyl-Δ3-pyrroline-3 methyl) Methanethiosulfonate (MTSL)	Toronto Research Chemicals, Toronto, Canada
1-palmitoyl-2-oleoyl-*sn*-glycero-3-phosphocholine (POPC)	Avanti Polar Lipids, Albaster, USA
1,2-dimyristoyl-*sn*-glycero-3-phosphocholine (DMPC)	Avanti Polar Lipids, Albaster, USA
6X MassRuler DNA Loading Dye	Fermentas, Sankt Leon-Rot
Atto 488 1,2-dimyristoyl-*sn*-glycero-3-phosphoethanolamine (Atto 488 DMPE)	ATTO-TEC, Siegen
Atto 647N 1,2-dimyristoyl-*sn*-glycero-3-phosphoethanolamine (Atto 647N DMPE)	ATTO-TEC, Siegen
Acrylamide 4K solution (30%) (mix 29:1)	Applichem, Darmstadt
Agarose MP	Applichem, Darmstadt
Ampicillin	Applichem, Darmstadt
Ammonium chloride (^{15}N, 99%)	Eurisotop, Saarbrücken
L-Ascorbic acid	Sigma-Aldrich, Munich
Bio-Beads SM-2 adsorbent	Bio-Rad Laboratories, Munich
Bovine serum albumin (BSA), Assay≥99	Sigma-Aldrich, Munich
Bromophenol blue sodium salt	Merck, Darmstadt

Chloramphenicol	Roth, Karlsruhe
Complete EDTA-free protease inhibitor cocktail tablet	Roche, Freiburg
Coomassie Brilliant Blue	Merck, Darmstadt
Deuterium Oxide, D_2O (^2H, 99.9%)	Sigma-Aldrich, Munich
Dithiothreitol (DTT)	Applichem, Darmstadt
DNase I	Applichem, Darmstadt
Dodecylphosphocholine-D38 (^2H, 98%)	Chemotrade, Leipzig
Ethylenediaminetetraacetic acid (EDTA)	Applichem, Darmstadt
Ethidium bromide solution 1%	Applichem, Darmstadt
GeneRuler 1 kb DNA Ladder	Fermentas, Sankt Leon-Rot
Guanidine hydrochloride	Applichem, Darmstadt
Glutathione (reduced)	Merck, Darmstadt
Glutathione Sepharose 4B (GSH-Sepharose)	GE Healthcare, Freiburg
Imidazole	Applichem, Darmstadt
Isopropyl-beta-D-thiogalactoside (IPTG)	Roth, Karlsruhe
Kanamycin sulphate	Calbiochem, Darmstadt
β-Mercaptethanol	Sigma-Aldrich, Munich
Nickel nitrilotriacetic acid (Ni-NTA)	Qiagen, Hilden
NucleoSpin Plasmid-plasmid Miniprep kit	Macherey Nagel, Düren
Phenylmethanesulfonylfluoride (PMSF)	Applichem, Darmstadt
Sodium cholate hydrate	Sigma-Aldrich, Munich
Sodium deoxycholate	Sigma-Aldrich, Munich
Tween-20	Roth, Karlsruhe
Triton-X-100	Merck, Darmstadt
Unstained Protein Molecular Weight Marker	Fermentas, Sankt Leon-Rot

2.1.2 Enzymes and synthetic peptides

Table 2: List of enzymes and synthetic peptides

Enzyme/peptide	Supplier
GST-tagged PreScission protease	Recombinantly produced at ICS-6
His-tagged PreScission protease	Recombinantly produced at ICS-6
Lysozyme	Applichem, Darmstadt
P6 peptide (Residues 18-77) (PAVDLLEKYM QQGKRQREQR ERPYKEVTED LLHLEQGETP YREPPTEDLL HLNSLFGKDQ)	JPT Peptide Technologies, Berlin
His-tagged TEV protease S219V	Recombinantly produced at ICS-6
Thrombin protease	Roth, Karlsruhe

2.1.3 Bacterial strains

The following strains were used for DNA amplification and recombinant protein expression.

Table 3: List of bacterial strains used

Strain	Genotype	Source
E.coli Top 10	F- *mcr*A Δ(*mrr-hsd*RMS-*mcr*BC) φ80*lacZ*ΔM15 Δ*lac*X74 nupG *rec*A1 *ara*D139 Δ(ara-leu)7697 *gal*E15 galK16 rpsL(Str^R) endA1 λ$^-$	Invitrogen, USA
E.coli DH5α	F$^–$, Φ80d*lacZ*ΔM15, Δ(*lacZYA-argF*)U169, *deoR*, *recA*1, *endA*1, *hsdR*17(rK–, mK+), *pho*A, supE44, λ–, *thi*-1, *gyrA*96, *relA*1	TaKaRa Biomedicals, Japan
E.coli Mach T1 Phage-Resistant cells	F$^–$ Φ80*lacZ*ΔM15 Δ*lac*X74 *hsdR* (rK–, mK+) Δ *recA1398 endA*1 *ton*A	Invitrogen, USA

E.coli BL21 Codon-Plus (DE3) RIL	*E.coli* B, F^{-}, *dcm*, *ompT*, *hsdS*(r_B^- m_B^-), *gal*, λ(DE3) *endA, Hte,* [*arg*U *ile* Y, *leu*W *Cam*$_r$]	Stratagene Europe, Amsterdam
E.coli BL21 (DE3)	*E.coli* B, F^{-}, *dcm*, *ompT*, *hsdS*(r_B^- m_B^-), *gal*, λ(DE3)	Novagen, Darmstadt
E.*coli* C43 (DE3)	*E.coli* B, F^{-}, *dcm*, *ompT*, *hsdS*(r_B^-, m_B^-), *lon*, *gal*, λ(DE3)	BioCat, Heidelberg

2.1.4 Vectors

All the following vectors are available in the plasmid collection of the Institute of Complex Systems – Structural Biochemistry (ICS-6).

Table 4: List of vectors used for cloning and expression

Vector name	Resistance	Characteristic
pET28a_MSP1	Kanamycin	6His-MSP1
pET15b_kombi-PreScission with His-Tag	Ampicillin	6His-PreScission protease
pRK793	Ampicillin	Tobacco etch virus (TEV) protease S219V
pGEX-Prescission-Protease	Ampicillin	GST-PreScission protease
pETDuet-1ΔHisTag-Nef_MCS2	Ampicillin	Full length Nef protein of HIV-1 SF2 (MCS2)
pTKK19xb/ub_ubi-CD4mut	Kanamycin	10His-Ubiquitin CD4mut (372-433)
pTKK19xb/ub_ubi_CD4_R-3C	Kanamycin	10HisUbiquitinCD4mut, with cysteine at minus 3 position
pTKK19xb/ub_ubi_CD4_S-422C	Kanamycin	10HisUbiquitinCD4mut, with cysteine at position 422

pTKK19xb/ub_ubi_CD4_S-397C	Kanamycin	10HisUbiquitinCD4mut, with cysteine at position 397
pGEX-VpUcyt	Ampicillin	Residues 39-81, of the cytoplasmic domain of VpU, HIV-1 strain HV1S1

2.1.5 Media

2.1.5.1 Lysogeny broth (LB)

LB medium contains 10 g/l tryptone, 5 g/l yeast extract, 5 g/l NaCl pH 7.0.

2.1.5.2 Minimal medium (M9)

M9 medium supplemented with a trace element solution (TS2) was used for the expression of isotope labelled protein (*98*). The composition of the M9 medium, TS2 solution and vitamin cocktail is as follows.

Table 5a: Composition of M9 medium

Chemical	Concentration
$Na_2HPO4{\cdot}2H_2O$	9.14 g/l
KH_2PO_4	3 g/l
NaCl	0.5 g/l
$^{14}NH_4Cl$ or $^{15}NH_4Cl$	1 g/l
$CaCl_2$	0.1 mM
TS2 solution	0.2% (v/v)
Fe(III)-citrate	10 µM
Vitamin cocktail solution	0.1 (v/v)
Thiamine hydrochloride (Vitamin B1)	5 mg/ml

$MgSO_4$	2 mM
(^{13}C, 99%)-labelled or unlabelled glucose	4 g/l

Table 5b: TS2 solution

Chemical	Concentration
$MnCl_2 \cdot H_2O$	30 mg/l
$ZnSO_4 \cdot 7H_2O$	100 mg/l
H_3BO_3	300 mg/l
$CoCl_2.6H_2O$	200 mg/l
$NiCl_2 \cdot 2H_2O$	20 mg/l
$CuCl_2 \cdot 2H_2O$	10 mg/l
$Na_2MoO_4 \cdot 2H_2O$	900 mg/l
Na_2SeO_3	20 mg/l

Table 5c: Vitamin cocktail

Chemical	Concentration
d-Biotin	1 mg/l
Choline chloride	1 mg/l
Folic acid	1 mg/l
Nicotinamide	1 mg/l
Sodium-D-pantothenate	1 mg/l
Pyridoxal hydrochloride	1 mg/l
Riboflavin	0.1 mg/l

2.1.6 Lipids

POPC and DMPC were dissolved in chloroform at a concentration of 20 mg/ml. Upon arrival Atto 488 DMPE and Atto 647N DMPE were dissolved in a chloroform:methanol (4:1) mixture at a 1 mg/ml concentration. All lipid solutions were aliquoted into 2 ml brown glass vials, sealed with teflon caps and kept at -80 °C until further use.

2.1.7 Standard laboratory instrumentation and miscellaneous equipment

Table 6: List of standard laboratory and miscellaneous equipment

Equipment	Supplier
Äkta purifier	GE Healthcare, Freiburg
Branson sonifier 250	Branson Ultrasonics Corp, Danbury, USA
Centrifuge 5415D	Eppendorf, Hamburg
Centrifuge 5804R	Eppendorf, Hamburg
Centrifuge Avanti J-20 XP	Beckman Coulter, Krefeld
Freeze dryer, Alpha 1-4	Martin Christ GmbH, Osterode am Harz
GelDoc 2000	Bio-Rad, Munich
HEλIOS ε spectrophotometer	Thermo Scientific, Waltham, USA
Hoefer mighty small SE 260 vertical gel electrophoresis apparatus	Hoefer Scientific Instruments, San Francisco, USA
Horizontal DNA electrophoresis apparatus	GE Healthcare, Freiburg
Lambda 25 UV/Vis spectrophotometer	PerkinElmer, Rodgau
LC 1200 series HPLC system	Agilent Technologies, Böblingen
LiposoFast-Basic extruder	Avestin, Mannheim
LKB FPLC system	GE Healthcare, Freiburg
pH meter	Mettler Toledo, Steinbach
Semi-micro balance CP225D	Sartorius, Göttingen
Vacuum pump, D25E	Leybold, Cologne

2.1.8 Consumables

Table 7: List of consumables

Consumable	Supplier
Centricon concentrator	Millipore, Schwalbach
Centriprep concentrator, YM-10 centrifugal filter unit	Millipore, Schwalbach
Eppendorf UVette cuvettes	Sigma-Aldrich, Munich
Hamilton air-tight syringe	Hamilton, Reno, USA
Nuclepore track-etched polycarbonate membranes	GE Healthcare, Freiburg
Quantum EX cartridge	Millipore, Schwalbach
Spectra/Por dialysis membranes	SpectrumLabs, Breda, The Netherlands
Vivaspin concentrator	Sartorius Stedim, Göttingen

2.1.9 Thermophoresis equipment

MST data were recorded on the Monolith NT.115 system, manufactured by Nanotemper technologies, Munich. The instrument is equipped with filters to detect either blue or red fluorescence. Capillaries are placed in slots on a sample tray. The tray is then manually slid into its designated slot in the Monolith machine. Up to 16 capillaries can be measured during a single experiment. Capillary temperature (i.e. ambient temperature) can be varied from 20-45 °C. All experiments in this work were conducted at 25 °C. The five types of capillaries (standard, hydrophilic, hydrophobic, BSA coated, enhanced gradient) were also purchased from Nanotemper technologies. The system is run using the NTControl data acquisition software. Analysis of data was carried out using the NTAnalysis software.

2.1.10 Chromatography equipment

Glutathione Sepharose 4B and nickel nitrilotriacetic acid (Ni-NTA) agarose were purchased from GE Healthcare (Freiburg) and Qiagen (Hilden). All affinity purifications involving Glutathione Sepharose 4B and nitrilotriacetic acid (Ni-NTA) agarose were performed using gravity flow columns. Size exclusion chromatography was performed using the Äkta purifier (GE Healthcare, Freiburg) and the LKB FPLC system (GE Healthcare, Freiburg). Reverse phase chromatography was carried out using the LC 1200 series HPLC system (Agilent Technologies). Columns used in this study are listed in table 8.

Table 8: List of columns used

Column name	Supplier
HiPrep 26/10 Desalting	GE Healthcare, Freiburg
RESOURCE 15 RPC 1 ml	GE Healthcare, Freiburg
RESOURCE 15 RPC 3 ml	GE Healthcare, Freiburg
Superdex 200 10/300 GL	GE Healthcare, Freiburg
Superdex 200 XK26/70 pg	GE Healthcare, Freiburg
HiLoad 26/60 Superdex 75 pg	GE Healthcare, Freiburg

2.1.11 NMR spectrometer and equipment

Two-dimensional $^{1}H,^{15}N$-HSQC spectra were recorded at 14.1 T and 25 °C on a Varian Inova 600 spectrometer equipped with a cryogenic HCN triple-resonance probe containing a shielded field gradient along the z-axis. HSQC spectra were recorded using a standard Varian gNfhsqc pulse sequence. During experiments, NMR samples were stored in the Shigemi 5 mm symmetrical NMR microtube assembly (Sigma-Aldrich). All samples contained 10% D2O in their buffers, for field locking and shimming. NMR data were processed with nmrPipe (*99*) and analysed with CARA (*100*). For the PRE measurements, peak intensities were calculated using the 'model-based linear equation system', in CARA.

2.1.12 Software

The following software were used during the course of this work.

Table 9: List of software used

Software	Application
ExPASy-ProtParam (http://web.expasy.org)	Analysis of protein sequences (extinction coefficients, molecular weight)
ExPASy-Translate Tool (http://web.expasy.org)	Translation of a nucleotide (DNA/RNA) sequence to an amino acid sequence
PyMOL	Visualization of protein structures
NTAnalysis	Analysis of MST data
nmrDraw, nmrPipe	Analysis of NMR data
CARA (Computer Aided Resonance Assignment)	Analysis of NMR data
Quality One	Visualization and documentation of gels

2.2 Methods

2.2.1 DNA methods

2.2.1.1 Plasmid isolation

Plasmids were isolated using commercially available kits (cf. Table 1), following the manufacturers recommended protocols. *E.coli* strains DH5α, Mach 1 or Top10 (cf. Table 3) were used for amplification of plasmid DNA.

2.2.1.2 DNA gel electrophoresis

Gel electrophoresis is based on the principle of differential migration of charged molecules in an electric field. The velocity of migration is most influenced by the size of the DNA molecule, but other factors like charge, conformation of DNA, temperature, agarose concentration and strength of the applied electrical field also play a defining role.

DNA separation was carried out in a horizontal gel electrophoresis apparatus. Agarose concentration was varied from 0.2 to 8%, depending on the size of the DNA molecules. Gels were prepared by dissolving the required agarose amount in a TAE buffer (Table 10), supplemented with 1 mg/l ethidium bromide (AppliChem, Darmstadt). The agarose solution was liquefied by heating at 60 °C, followed by immediate casting of the gel. Cast gels solidified completely in 10-15 minutes, after which samples were loaded. Prior to loading, 1/5 (v/v) of a sixfold DNA loading buffer (Fermentas, Sankt Leon-Rot) was added to the sample. Electrophoresis was performed at a constant voltage of 80 V. The GeneRuler 1 kb DNA Ladder (Fermentas, Sankt Leon-Rot) was used for the estimation of size and amount of DNA. Gels were then imaged under UV light and analyzed using the GelDoc 2000 documentation system.

Table 10: Buffers used for DNA gel electrophoresis

Buffer	Composition
TAE buffer	40 mM Tris acetate pH 8.0, 1 mM EDTA
6x DNA loading buffer	10 mM Tris-HCl pH 7.6, 0.03% (w/v) bromophenol blue, 0.03% (w/v) xylene cyanol FF, 60% (v/v) glycerol, 60 mM EDTA

2.2.1.3 DNA concentration determination

Concentration of DNA was determined by measuring UV light absorption at 260 nm with an optical path cuvette of 1 cm (*101*). An absorbance of 1 corresponds to ~50 µg/ml of double-stranded DNA.

2.2.1.4 DNA sequencing

DNA sequencing was carried out at Seqlab (Sequence Laboratories Göttingen). Sequencing required 700 ng of vector DNA, along with 25 pmol of a forward primer.

2.2.2 Protein analysis techniques

2.2.2.1 SDS-PAGE

Separation of proteins was carried out using discontinuous sodium dodecyl sulphate polyacrylamide gel electrophoresis (SDS-PAGE), consisting of a stacking and separating gel (*102*). Prior to loading, 4X sample buffer was added to the sample, followed by incubating the sample at 95 °C for 5 minutes. The SDS present in the sample buffer denatures the protein molecules giving them all a similar rod like structure. SDS also coats the proteins with a negative charge. The amount of bound SDS is proportional to the protein size, so all proteins have an approximately similar

charge to mass ratio. Separation of such proteins in an electric field is thus governed only by their size.

Electrophoresis was carried out on the Hoefer mighty small SE 260 vertical gel electrophoresis apparatus at a constant current of 40 mA for 45 minutes. Gels had a 15 cm height, 10 cm width and 0.75 mm thickness. The Unstained Protein Molecular Weight Marker (Fermentas, Sankt Leon-Rot) was used in the estimation of protein sizes. After the run, gels were carefully removed and then stained for 30 minutes in a solution of Coomassie dye (25% isopropanol, 10% acetic acid, 0.5% g/l Coomassie Brilliant Blue R-250 in ddH_2O). This was followed by destaining the gel in boiling water for ~1 min. Gels were analyzed using the GelDoc 2000 documentation system. Composition of various components is given in table 11.

Table 11: Components of SDS-PAGE

Stacking gel (5%)	**Separating gel (15%)**
4.85% (w/v) acrylamide	14.55% (w/v) acrylamide
0.15% (w/v) N,N'-methylenebisacrylamide	0.45% (w/v) N,N'-methylenebisacrylamide
125 mM Tris-HCl pH 6.8	375 mM Tris-HCl pH 8.8
0.1% (w/v) SDS	0.1% (w/v) SDS
0.1% (v/v) APS	0.1% (v/v) APS
0.1% (v/v) TEMED	0.1% (v/v) TEMED

SDS running buffer	**Fourfold sample buffer**
50 mM Tris-HCl pH 8.3	200 mM Tris-HCl pH 6.8
385 mM glycine	40% (v/v) glycerol
0.1% (w/v) SDS	8% (w/v) SDS
	8% (v/v) *β*-mercaptoethanol
	0.05% (w/v) bromophenol blue

2.2.2.2 Protein concentration determination

Concentrations of proteins containing aromatic amino acids were determined by their absorbance at 280 nm (A_{280}), using a Lambda 25 UV/Vis spectrophotometer (PerkinElmer, Rodgau). Samples were measured using the Eppendorf UVette cuvettes (Sigma-Aldrich, Munich). Cuvettes are UV-Vis transparent between 220 and 1600 nm, and have an optical pathlength of 1 cm. Extinction coefficients were calculated with the Protparam tool from ExPasy (http://web.expasy.org/cgi-bin/protparam/protparam). Proteins that do not contain any aromatic amino acids were weighed as salt free lyophilized powders using a semi-micro balance. Required protein concentrations were then obtained by addition of appropriate buffer volumes.

Protein concentrations are determined using the Beer-Lambert law, which can be stated as follows

$$A = \varepsilon \cdot l \cdot c$$

Where A is the measured absorbance of the protein solution at 280 nm, ε is the molar extinction coefficient of the protein at 280 nm, l is the optical pathlength, and c is the protein concentration.

Note that the measured absorbance is due to absorption by the protein as well as light scattering. A more accurate measure of protein absorbance was obtained by manually subtracting the scattering effects from the absorption curve.

2.2.3 Protein expression and purification

2.2.3.1 Membrane scaffold protein (MSP)

The protein expression was carried out in LB medium supplemented with 50 µg/ml kanamycin. *E.coli* BL21 DE3 cells were first transformed with the pET28a_MSP1 plasmid, carrying the MSP gene.

Cells were grown at 37 °C, 150 rpm to OD_{600} = 0.6, after which protein expression was induced by the addition of 1 mM Isopropyl-beta-D-thiogalactoside (IPTG). Expression was carried out for 4 hours, after which the cells were harvested by centrifugation (5500 x g, 15 min). Cell pellets were then washed with 1X PBS and stored at -20 °C.

Purification of MSP was carried out as published (*103*). Cell pellets were first resuspended in lysis buffer (20 mM NaPi pH 7.4, Complete EDTA-free protease inhibitor cocktail tablet, lysozyme, DNase, 1% Triton X-100). Resuspended cells were then subjected to sonication (3 cycles, 30 seconds each), using a Branson 250 sonifier equipped with a microtip. Lysed cells were passed through a Ni-NTA agarose containing gravity column. MSP was eluted with an elution buffer containing imidazole (40 mM Tris-HCl pH 8.0, 300 mM NaCl, 300 mM imidazole). MSP containing fractions were pooled and dialyzed against a TEV protease cleavage buffer (50 mM Tris-HCl pH 8.0, 0.5 mM EDTA, 1 mM DTT), using a dialysis membrane with a 3500 Da molecular weight cut-off (MWCO). Cleavage was carried out at room temperature for 48-60 hours, using a mutant TEV protease (S219V) which was recombinantly produced in *E.coli* and purified in our laboratory (*104, 105*). After cleavage, the protein mixture was dialyzed against buffer containing 20 mM Tris-HCl pH 8.0, 150 mM NaCl. After dialysis sodium cholate was added to a final concentration of 50 mM. Cleaved MSP was separated from its cleaved 6X His tag and the His-tagged TEV protease via a gravity column packed with Ni-NTA agarose. Presence of pure cleaved MSP was confirmed via SDS-PAGE. Fractions containing cleaved MSP were pooled and dialyzed against a nanodisc assembly buffer (20 mM Tris-HCl pH 7.4, 100 mM NaCl, 0.5 mM EDTA). MSP solutions were then concentrated to the desired amounts (usually 2 mg/ml) using centriprep concentrators YM-10 (Millipore, Schwalbach). Aliquots of concentrated protein were then shock frozen in liquid nitrogen, lyophilized and stored at -20 °C. Figure 8 highlights the major steps in MSP purification.

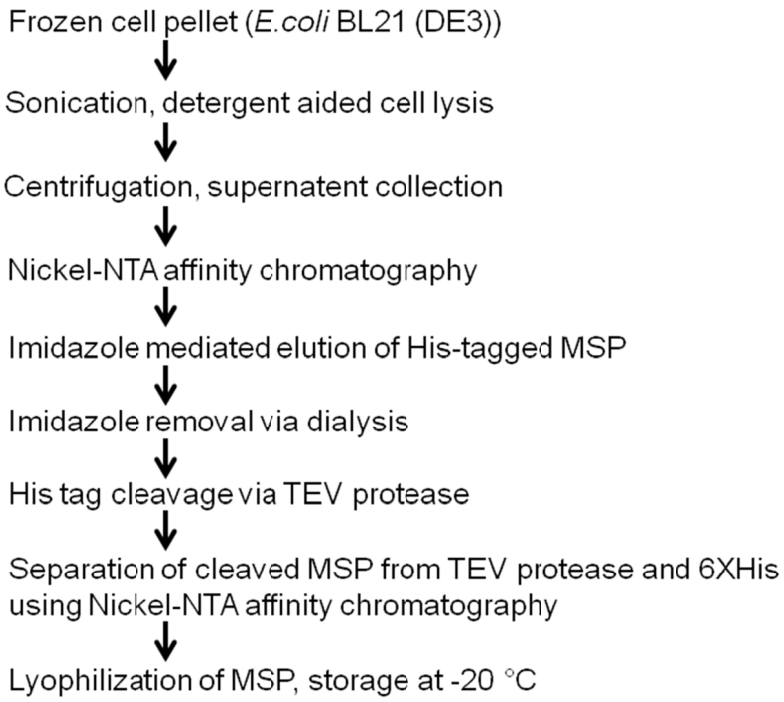

Figure 8: Individual steps in MSP purification

2.2.3.2 CD4mut and HisUbiquitinCD4mut

Expression and purification of the CD4mut and HisUbiquitinCD4mut was carried out as previously published (*106, 107*).

The protein is expressed as a fusion protein comprising an N-terminal decahistidine tag, the 76 residue fusion partner yeast ubiquitin, a 14 residue linker containing PreScission and Thrombin cleavage sites, and a 62 residue CD4 fragment comprising the transmembrane and cytoplasmic domains of the CD4 receptor. CD4mut is obtained after cleavage of the fusion protein with His-tagged PreScission protease. CD4mut contains four serines and a histidine in place of five naturally occurring cysteines (C394S, C397S, C420S, C422S, and C430H).

Expression was carried out in *E. coli* C43(DE3) competent cells transformed with the pTKK19xb/ub_ubi-CD4mut plasmid. Cells were grown at 37 °C, 150 rpm to an OD_{600} of 0.6, after which protein expression was induced by the addition of 1 mM IPTG. Expression was carried out for 4-6 hours, after which the cells were harvested by

centrifugation (5500 x g, 15 min). Cell pellets were then washed with 1X PBS and stored at -20 °C.

Cell pellets were first resuspended in lysis buffer (50 mM Tris-HCl pH 8.0, 1% (v/v) Triton X-100, 1% (w/v) cholic acid, 600 mM NaCl, 0.1% sodium azide). Resuspended cells were then subjected to sonication (3 cycles, 30 seconds each), using a Branson 250 sonifier equipped with a microtip. Lysed cells were passed through a Ni-NTA agarose containing gravity column. HisUbiquitinCD4mut was eluted with an elution buffer containing imidazole (50 mM Tris-HCl pH 8.0, 12.5% (w/v) sucrose, 0.5% (w/v) cholic acid, 0.1% NaN_3, 300 mM NaCl, 0.5% Triton X-100, 8 mM $MgCl_2$, cOmplete EDTA-free protease inhibitor tablet, 300 mM imidazole). Imidazole was removed via buffer exchange using a HiPrep 26/10 Desalting column (GE Healthcare, Freiburg). The column was operated using an Äkta purifier. The imidazole-free protein was then cleaved using His-tagged PreScission protease. Cleavage was carried out overnight, at 4 °C, with gentle shaking. Cleaved CD4mut was separated from His-Ubiquitin and His-PreScission protease using Ni-NTA agarose. The CD4mut protein was obtained in the flowthrough. Triton X-100 was separated from CD4mut using trichloroacetic acid (TCA) based precipitation (10% TCA) at 4 °C. Precipitated protein pellets were washed twice with 100% acetone. The CD4mut pellet was resuspended in a solution of 40% acetonitrile, 60% H_2O, 0.09% TFA. The CD4mut solution was applied to a RESOURCE 15 RPC 3 ml reverse phase column (GE Healthcare, Freiburg), and eluted using a discontinuous gradient of 0 to 100%, of 80% acetonitrile in 0.08% TFA. The column was operated using the LC 1200 series HPLC system (Agilent Technologies). Presence of pure CD4mut in specific elution fractions was confirmed by SDS-PAGE. CD4mut containing fractions were shock frozen in liquid nitrogen, lyophilized and stored at -20 °C.

The purification protocols for CD4mut and the uncleaved HisUbiquitinCD4mut are the same, except that the steps involving the PreScission mediated cleavage were skipped for HisUbiquitinCD4mut. Figure 9 highlights the major steps in purification of both proteins. The steps involving PreScission cleavage have been coloured red.

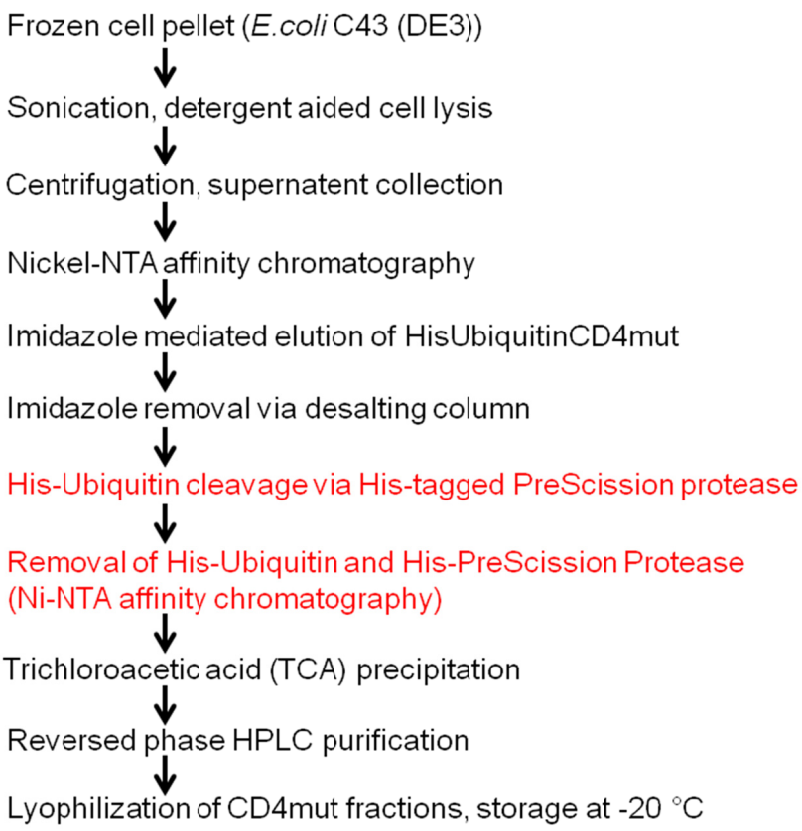

Figure 9: Steps involved in the purification of CD4mut and HisUbiquitinCD4mut. Steps coloured red are skipped during HisUbiquitinCD4mut purification.

2.2.3.3 CD4mut single cysteine mutants

The CD4mut single cysteine mutants (CD4S397C, CD4S422C and CD4R(-3)C) were purified in the same manner as CD4mut (cf. 2.2.3.2), except that all buffers were carefully degassed and supplemented with 10 mM β-mercaptoethanol, in order to prevent oxidation of the cysteines.

2.2.3.4 Nef

The protein expression was carried out in LB medium supplemented with ampicillin (100 µg/ml) and chloramphenicol (34 µg/ml). *E.coli* BL21-CodonPlus(DE3)-RIL cells (Stratagene) were transformed with the pETDuet-1ΔHis-Tag_Nef_MCS2 vector

plasmid, carrying the Nef gene (cf. 2.1.4). The cultures were grown to an OD_{600} of 0.6, after which their temperatures were reduced from 37 °C to 28 °C. Gene expression was induced at an OD_{600} of 0.6, by addition of 0.5 mM IPTG. Expression was carried out for 4 hours, with gentle shaking (150 rpm). Cultures were then spun down (5500 x g, 4 °C, 20 min), and the resultant pellets were washed with 1X PBS and stored at -20 °C.

For purification, cell pellets obtained from 1 l culture volumes were suspended in 25 ml lysis buffer (20 mM Tris-HCl pH 8.0, 500 mM NaCl, 20 mM imidazole, 15 mM β-mercaptoethanol) supplemented with lysozyme (200 µg/ml) and a cOmplete EDTA-free protease inhibitor cocktail tablet (Roche). Resuspended cells were then subjected to sonication (3 cycles, 30 seconds each) using a Branson 250 sonifier equipped with a microtip. The lysed cell solution was spun down (50000 x g, 4 °C, 30 min), and the supernatant was collected and used for subsequent purification steps. Purification was carried out in the cold room, at 6 °C. The supernatant was applied to a gravity flow column containing Ni-NTA agarose (Qiagen, Hilden), pre-equilibrated by washing with 5 column volumes (CV) of lysis buffer. Unbound or weakly unspecifically bound substances were removed by first washing the column with 10 CV of lysis buffer supplemented with 30 mM imidazole. Specifically bound His-tagged Nef was eluted by increasing the imidazole concentration up to 200 mM. Nef containing fractions were then pooled and dialyzed against a solution of 20 mM Tris-HCl pH 8.0, 500 mM NaCl, 15 mM β-mercaptoethanol). The His tag was simultaneously cleaved by addition of glutathione-S-transferase (GST) tagged PreScission protease to the dialysis solution (1 mg protease per 5 mg of Nef).

Following dialysis, the solution was passed through two gravity flow columns, one containing Ni-NTA, and the other containing GSH-Sepharose. The His tag binds Ni-NTA, the PreScission protease binds GSH-Sepharose, and cleaved Nef is collected in the flowthrough. The flowthrough fractions are pooled and applied to a HiLoad 26/60 Superdex 75 prep grade column (GE Healthcare, Freiburg), pre-equilibrated with 20 mM Tris-HCl pH 8.0, 150 mM NaCl, 15 mM β-mercaptoethanol. The column is operated using an FPLC system (GE Healthcare) at 6 °C, and a flow rate of 1.5 ml per minute. Presence of pure Nef in the elution fractions was confirmed by SDS-PAGE. Nef fractions were pooled and concentrated using centriprep devices with a MWCO of 3500 Da (Millipore, Schwalbach). Concentrated Nef solutions were shock frozen in liquid nitrogen and stored at -80 °C, until further use. The important steps in Nef purification are summarized in figure 10.

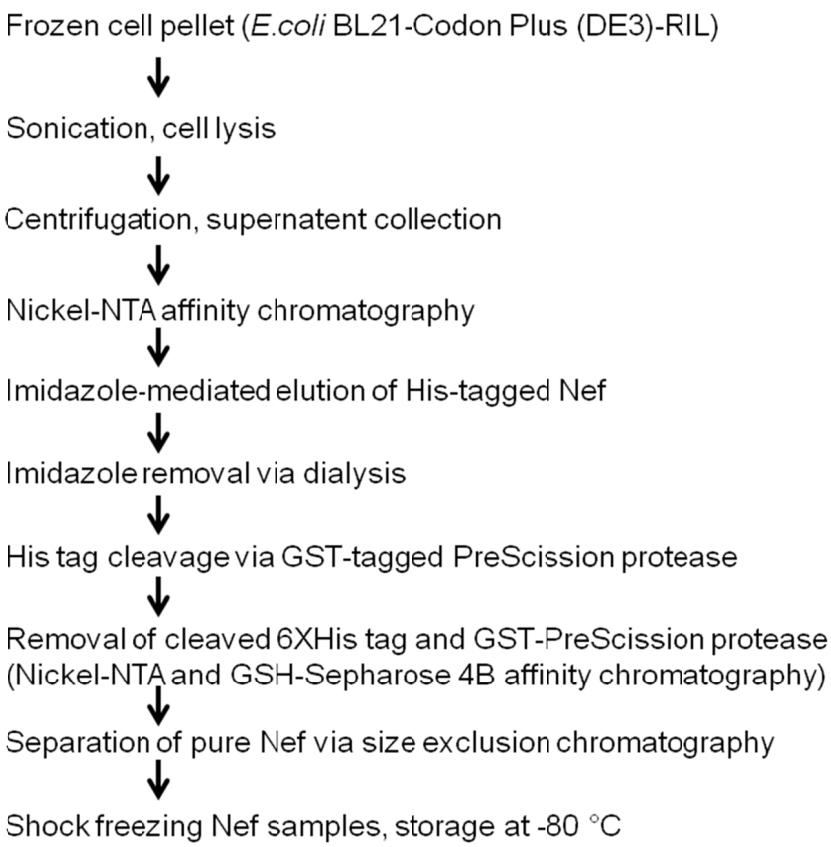

Figure 10: Individual steps involved in Nef purification.

2.2.3.5 VpUcyt

Expression and purification of VpUcyt was carried out as previously published by Wittlich et.al (*108*). Sequentially, VpUcyt contains amino acids 39 to 81, which make up majority of the cytoplasmic domain of VpU (*108*). Expression was carried out in the *E.coli* BL21(DE3) cell strain, in M9 minimal medium supplemented with ^{15}N ammonium chloride (Eurisotop, Saarbrücken). Cells were grown at 37 °C, 150 rpm to an OD_{600} of 0.6, after which protein expression was induced by the addition of 1 mM IPTG. Expression was carried out for 4 hours, after which the cells were harvested by centrifugation (5500 x g, 15 min). Cell pellets were then washed with 1X PBS and stored at -20 °C. Cell pellets were first resuspended in lysis buffer (1X PBS, 100 µg/ml lysozyme, 20 µg/ml DNAse I, 8 mM $MgCl_2$), and incubated at 11 °C, for 1 hour, with gentle shaking. This was followed by sonication (3 cycles, 30 seconds each), using a Branson 250 sonifier equipped with a microtip. Lysed cells were passed through a GSH-Sepharose containing gravity column, equilibrated with 1X PBS. The

column containing bound GST-VpUcyt was then incubated on a shaker for 1 hour. Following cleavage with the enzyme Thrombin, cleaved VpUcyt was obtained in the flowthrough. Thrombin was inactivated by the addition of 1 mM phenylmethylsulfonyl fluoride (PMSF) to the flowthrough solution.

The VpUcyt containing solution was applied to a RESOURCE 15 RPC 3 ml reverse phase column, and eluted using a discontinuous gradient from 0 to 100%, of 60% acetonitrile in 50 mM ammonium acetate. The column was operated using the LC 1200 series HPLC system (Agilent Technologies). Presence of pure VpUcyt in specific elution fractions was confirmed by SDS-PAGE. VpUcyt containing fractions were shock frozen in liquid nitrogen, lyophilized and stored at -20 °C. Figure 11 highlights the major steps in VpUcyt purification.

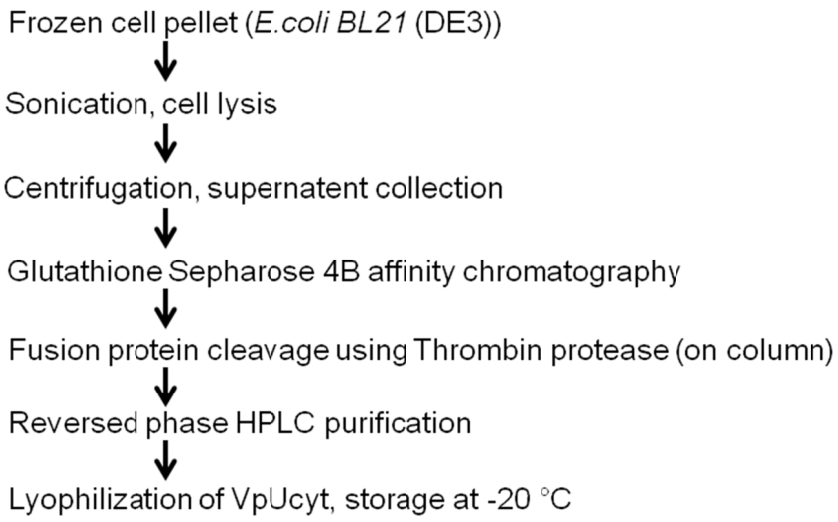

Figure 11: Individual steps involved in VpUcyt purification

2.2.4 Preparation of nanodiscs

2.2.4.1 Preparation of lipids

The principal lipid used was either 1-palmitoyl-2-oleoyl-*sn*-glycero-3-phosphocholine (POPC), or 1,2-dimyristoyl-*sn*-glycero-3-phosphocholine (DMPC). Additionally a small amount of fluorescently labelled lipid, either Atto 647N 1,2-dimyristoyl-*sn*-glycero-3-phosphoethanolamine (Atto 647N DMPE), or Atto 488 1,2-dimyristoyl-*sn*-

glycero-3-phosphoethanolamine (Atto 488 DMPE), was added to the lipid component. The ratio of the principal lipid and fluorescently labelled lipid was 60 to 1 for POPC nanodiscs, and 70 to 1 for DMPC nanodiscs. The required amount of lipid mixture (in chloroform) was pipetted into a glass test tube using an air tight Hamilton syringe, after which it was dried under a gentle stream of nitrogen gas. The dried lipid film was dissolved in 0.5-1 ml of cyclohexane, frozen in liquid nitrogen and freeze dried overnight using the D25E vacumn pump (Leybold, Cologne), equipped with a solvent trap immersed in liquid nitrogen. For dissolving DMPC, a small volume of ethanol (5%) was added to the cyclohexane solution. Lyophilized lipid was dissolved in lipid buffer containing the detergent sodium cholate (20 mM Tris-HCl pH 7.4, 100 mM sodium cholate) to a final concentration of 50 mM lipid. The lyophilyzed lipid powder was dissolved by first gently aspirating the solution by means of a pipette, followed by incubating the solution at 37 °C for 15-20 minutes.

2.2.4.2 Preparation of unloaded (empty) nanodiscs

Lyophilized, cleaved MSP was dissolved in water, resulting in the original protein stock solution in a buffer containing 20 mM Tris-HCl pH 7.4, 100 mM NaCl, 0.5 mM EDTA. Required volumes of MSP were mixed with the lipid/detergent stock solutions. The ratio of MSP:lipid:sodium cholate was 1:60:120 for POPC nanodiscs, and 1:70:120 for DMPC nanodiscs.

The assembly mixture was cycled between temperatures above and below the lipid phase transition, in order to break apart any large lipid aggregates that may have formed.

The sodium cholate was then removed using Bio-Beads SM2. Prior to use, the beads were washed with three volumes methanol, three volumes water and three volumes of an assembly buffer containing 20 mM Tris-HCl pH 7.4, 100 mM NaCl, 0.5 mM EDTA. About 0.5-0.6 g of wet Bio-Beads were used per millilitre of assembly mixture. The assembly mixture was incubated with Bio-Beads for 4 hours on an orbital shaker at room temperature. Removal of the sodium cholate causes the nanodiscs to spontaneously assemble. The resultant detergent free mixture was filtered through a 0.45 µm PVDF syringe filter. The nanodiscs in the filtered solution were then separated from unincorporated lipids, MSP and possibly remaining detergent molecules using size exclusion chromatography on a Superdex 200 10/300 GL column. The column was run in SEC buffer (10 mM sodium phosphate pH 7.4, 150 mM NaCl), on an Äkta purifier, at room temperature, at a flow rate of 0.5 ml/min. Based on the calibration with globular proteins, the elution volume of the nanodisc peak corresponds to a molecular weight of ~150 kDa.

2.2.4.3 Preparation of loaded nanodiscs

For assembly of HisUbiquitinCD4mut- or CD4mut-loaded nanodiscs, the appropriate amount of the lyophilized protein was first dissolved in 20 mM Tris-HCl pH 7.4, 100 mM NaCl, 100 mM dodecylphosphocholine. This solution was then added to the MSP-POPC-sodium cholate mixture (MSP:CD4 ratio was 1:0.5). The subsequent procedure was the same as the assembly of empty nanodiscs (cf. 2.2.4.2). The presence of the membrane protein in nanodiscs was confirmed by SDS-PAGE.

For assembly of Vpr loaded nanodiscs, the appropriate amount of lyophilized Vpr was added to a solution of preformed DMPC nanodiscs (MSP:Vpr ratio was 1:1). The mixture was incubated at room temperature for 3 to 4 hours on a roller shaker. The Vpr spontaneously incorporates into the nanodiscs. The nanodisc concentration was determined based on the absorption of the aromatic amino acids in MSP, at 280 nm (A_{280}), using a Lambda 25 UV/Vis spectrophotometer (PerkinElmer, Rodgau).

2.2.4.4 Separation of loaded from unloaded nanodiscs

HisUbiquitinCD4mut containing nanodiscs can be separated from unloaded nanodiscs using Ni-NTA affinity chromatography. After the SEC run, all the nanodisc-containing fractions are pooled and added to the Ni-NTA agarose-containing gravity flow column. Prior to this, the column is equilibrated by washing the column material (Ni-NTA agarose) with 5 CV of a buffer containing 10 mM sodium phosphate pH 7.4, 150 mM NaCl. Unloaded nanodiscs are washed away and can be collected in the flowthrough. Loaded discs bind to the Ni-NTA via the His tag on the HisUbiquitinCD4. The loaded discs are then eluted with 3-5 CV of SEC buffer, supplemented with 300 mM imidazole. The presence of loaded discs is verified using SDS-PAGE. Nanodisc solutions are then dialyzed against 10 mM sodium phosphate pH 7.4, 150 mM NaCl, 0.5 mM EDTA, at 6 °C, using a 10000 MWCO dialysis membrane.

2.2.5 Microscale thermophoresis

Experiments were carried out using the Monolith NT.115 instrument. Thermophoresis is measured by monitoring the fluorescence of the fluorescently labelled interaction partner in an applied temperature gradient. Fluorescence is excited by a LED beam.

Fluorescence emission originating in a small cylindrical section of the sample volume that is perpendicular to the capillary axis which holds the liquid sample is selected by the optics system and reaches the detector (cf. Figure 6). An IR laser beam is passed through the same optics system and is used to temporarily heat the same cylindrical section of the sample. The time dependent fluorescence intensity measured prior to, during and after operation of the IR laser is referred to as a thermophoretic time trace.

2.2.5.1 Sample preparation

All samples were prepared in a buffer containing 10 mM sodium phosphate pH 7.4, 150 mM NaCl. All samples were stored in low binding tubes (Biozym Scientific, Hessisch Oldendorf). Prior to an experiment, samples were spun down at 13000 x g for 5 min at room temperature. Storing protein samples in low binding tubes prevents their sticking to the tube walls. The sticking of proteins to the walls of storage vessels alters their concentrations in solution, and is thus a source of extensive error in experiments that aim to measure binding constants of protein-protein interactions. Spinning down of samples helps sediment aggregates or other large impurities, which otherwise cause sample inhomogeneity and consequently lead to bumpy raw data.

2.2.5.2 Capillary selection

Samples can be loaded into five types of commercially available capillaries, namely; standard, hydrophilic, hydrophobic, BSA-coated and enhanced gradient. The surfaces of hydrophilic, hydrophobic and BSA-coated capillaries have been chemically modified to suit certain sample types. The aim of capillary selection is to identify the capillary wherein there is no adsorption of the sample to the capillary walls. Feasibility and ease of sample loading should be checked for each capillary type. Standard, hydrophilic and hydrophobic capillaries were suitable for the nanodisc experiments.

2.2.5.3 Capillary scan

Capillary scanning allows one to estimate the amount of fluorescence dye in each capillary, and also serves as an indicator of whether samples adsorb to the capillary walls. Sample adsorption is indicated by U shaped curves. In the event of protein or ligand adsorption to the capillary walls, the experiment must be abandoned. If sample adsorption to the capillary walls occurs, it can often be prevented by either supplementing the sample with certain additives, or sample filtration.

2.2.5.4 Supplementation with additives

Addition of small amounts of certain additives to the buffer may passivate the capillary surface and prevent sample sticking (*65*). Types and amounts of additives used are listed in table 12

Table 12: List of additives used in MST experiments

Molecule	Concentration (vol%)	Concentration (μM)	Charge	CMC (mM)	Aggregation number
Sodium dodecyl sulphate (SDS)	0.005 to 0.1	173-3460	Anionic	8	62
Cetyl trimethylammonium bromide (CTAB)	0.005 to 0.1	137-2740	Cationic	1	170
Tween-20	0.005	40	Non ionic	0.06	-
Dodecylphosphocholine (DPC)	0.005	142	Zwitterionic	0.91	50-60
Bovine serum albumin (BSA)	0.005	0.75	-	-	-

2.2.5.5 Filtration

Filtration is carried out when supplementation with additives like detergents needs to be avoided. Nanodisc samples were first spun down at 13000 x g for 5 min at room temperature. The nanodisc solution was then gently passed through a nuclepore track-etched polycarbonate membrane (pore size 50 nm, GE Healthcare, Freiburg),

using a LiposoFast-Basic extruder (Avestin Europe, Mannheim). Nanodisc solutions were loaded into the capillaries immediately after filtration.

2.2.5.6 Laser power and laser intervals

Laser power denotes heating power, and thus determines the strength of thermophoresis. Its value can be varied from 10% to 100% (output power is in the milliwatt regime). Experiments with POPC-Atto 647N nanodiscs were carried out at 100% laser power. Experiments with DMPC-Atto 488 nanodiscs were carried out at 20, 40 and 80% laser powers. The laser on time was set to 30 seconds, while the final laser off time was set to 5 seconds. Laser on time denotes the time interval when the laser is turned on, and is thus the period when the temperature gradient exists. Final laser off time succeeds the laser on time, and is the period when the system measures the back-diffusion of the molecules to their initial state, due to cessation of the temperature gradient (cf. Figure 7).

2.2.5.7 Data analysis

Data analysis was carried out using the NTAnalysis software (Nanotemper technologies). The initial part of a thermophoretic time trace reflects a homogeneous fluorescence distribution before the laser is switched on (referred to as initial state in Figure 7). The measured and normalized fluorescence intensity in this state is termed F_{cold}. For MST data analysis, the measured fluorescence intensity is generally normalized to the average intensity measured in the initial state, resulting in $F_{cold} = 1$. After the laser has been switched on, the fluorescence is redistributed via two effects proceeding on different time scales. First, the “temperature jump” (T-Jump) reflects the temperature dependence of the fluorescence intensity of the dye and occurs on a typical time scale of ~50 ms. Second, thermophoresis causes motion of the dye carrying molecule on a diffusion time scale of ~10 seconds. Fluorescence intensity recorded with the laser power “on” (F_{hot}) will be dominated by the T-jump if measured shortly after switching on the laser (F_{hot}(early)), but reflects both T-jump and thermophoresis if measured after 10 s or later (F_{hot}(late)). Changes of fluorescence intensity observed 1 s or later after switching on the laser are dominated by thermophoresis. Both the T-jump and thermophoresis can be used to quantify the amount of free and bound fluorescently labeled binding partner in the sample, provided the respective property is significantly different for the free versus the bound

state of the labeled molecule. The software determines numeric values for $\overline{F_{cold}}$, $\overline{F_{hot}(early)}$ and $\overline{F_{hot}(late)}$ which are essentially averages of the normalized fluorescence intensity measured in user defined time windows placed in the initial state (F_{cold}), immediately after the T-jump ($F_{hot}(early)$) or at a time where the system is close to a steady state ($F_{hot}(late)$), respectively. For all time traces recorded for the multiple capillaries in an MST-based titration, the same time windows are utilized for averaging. In principle, either one of the quantities $\overline{F_{hot}(late)}$ / $\overline{F_{hot}(early)}$ (reflecting thermophoresis only), $\overline{F_{hot}(early)}$ / $\overline{F_{cold}}$ (reflecting T-jump only) and $\overline{F_{hot}(late)}$ / $\overline{F_{cold}}$ (reflecting T-jump and thermophoresis) carries information on the bound fraction of the fluorescently labeled molecule and could be used to derive a binding isotherm. However, in practice the characteristic thermophoretic properties of the studied system determine which of the three signal types are sensitive enough to complex formation and provide a binding isotherm with satisfactory signal-to-noise ratio.

All three types of signal were inspected after each measurement using the NTAnalysis software. Binding isotherms were fitted based on a 1:1 complex model.

2.2.6 NMR spectroscopy

NMR is a technique that takes advantage of the magnetic properties of nuclei, to obtain structural and dynamic information about the molecule under study. NMR uses the intrinsic property of nuclear spin, characterized by the nuclear spin quantum number, I. The rules governing the nuclear spin quantum number are as follows (i) Nuclei with odd mass numbers have half-integral spin quantum numbers, (ii) Nuclei with an even mass number and an even atomic number have spin quantum numbers equal to zero, and (iii) Nuclei with an even mass number and an odd atomic number have integral spin quantum numbers. Nuclei that belong to (ii) are termed NMR inactive, while those possessing non-zero spins (i, iii) are NMR active (e.g. ^{15}N, ^{13}C, ^{2}H). Such nuclei behave like positive charges spinning on axes. The spinning charge, like an electric current creates a tiny magnetic field (*109*).

2.2.6.1 Chemical Shift

Chemical shift reflects the resonance frequency of the nucleus. Each nucleus has a characteristic resonance frequency at a given field strength. The resonance frequency is proportional to the external magnetic field in the first approximation, and can be described as follows.

$$\boldsymbol{\nu = \frac{\gamma B_o}{2\pi}}$$

Where ν is resonance frequency of the nucleus, γ is the gyromagnetic ratio of the isotope, and B_o is the strength of the external magnetic field.

However, the exact magnetic field experienced by the nucleus may be slightly different from the external magnetic field (B_o). The cloud of electrons surrounding the nucleus create their own magnetic fields, which either subtract or add to the external magnetic field. The nucleus thus experiences a slightly different field (B_{eff}), depending on its chemical environment (*109*). The exact resonance frequency is thus given by,

$$\boldsymbol{\nu = \frac{\gamma B_{eff}}{2\pi}}$$

An NMR spectrum is a graph of intensity versus frequency for a narrow range of frequencies corresponding to the nucleus of interest. Each peak in such a spectrum is thus indicative of the environment experienced by the corresponding nucleus within the molecule. Using a quantity known as the chemical shift (δ), it is possible to differentiate nuclei based on differences in their resonance frequencies. The chemical shift is defined as the resonance frequency of the nucleus relative to a standard. It is usually expressed in parts per million (ppm), and is described as follows:

$$\boldsymbol{\delta = \frac{\nu - \nu_o}{observing\ frequency} 10^6}$$

Where ν is the resonance frequency of the nucleus, $\boldsymbol{\nu_o}$ is the frequency of a reference compound, and the observing frequency refers to the operating frequency of the spectrometer. Commonly used reference compounds include tetramethylsilane (TMS) and DSS (4,4-dimethyl-4-silapentane-1-sulfonic acid).

2.2.6.2 Different implementations of NMR spectroscopy

NMR measurements can be carried out using the continuous wave (CW), or Fourier transform (FT) methods. In continuous wave CW NMR, experiments are carried out by varying the frequency of irradiation at a constant magnetic field (frequency sweep), and measuring the absorption of energy by different nuclei. Alternatively, the magnetic field strength can also be varied at a constant irradiation frequency (field sweep). CW NMR was used before the advent FT NMR.

In FT NMR, all frequencies in a selected spectral range are irradiated simultaneously with a monochromatic radio frequency pulse. This causes the magnetization vector to precess about the external magnetic field vector. The oscillating magnetization induces a current in a nearby pickup coil, creating an electric signal known as the free induction decay (FID). An FID is the overlay of oscillations characterized by the resonance frequencies of all nuclei that contribute to the measured signal. The FID is a time domain signal, which is then Fourier transformed to obtain the frequency domain NMR spectrum.

2.2.6.3 Heteronuclear single quantum coherence (HSQC)

The two dimensional HSQC experiment permits one to obtain a 2D heteronuclear chemical shift correlation map between a directly bonded ^{1}H and a heteronuclei (usually ^{13}C or ^{15}N). In an HSQC experiment, the INEPT (Insensitive nuclei enhanced by polarization transfer) sequence is used to transfer ^{1}H spin polarization into antiphase heteronuclear single quantum coherence (*110*). The antiphase heteronuclear coherence evolves during the subsequent t_1 evolution period. A second INEPT sequence is used to transfer the frequency labelled heteronuclear coherence back to the proton magnetization for detection. The $^{1}H,^{15}N$ HSQC is commonly used in protein NMR. Each residue of a protein (except proline) has an amide proton attached to a nitrogen in the peptide bond. Such an experiment is a good indicator of the physical state of the protein. If the protein is well folded, the peaks are usually well dispersed. Also, most of the individual residue peaks can be distinguished from one another. In contrast, an unstructured or aggregated protein will show considerable peak overlap, especially in the middle of the HSQC spectrum.

2.2.6.4 Chemical shift perturbation (CSP)

Ligand binding usually affects the electron current density in the immediate vicinity of the binding site, resulting in localized chemical shift changes for nuclear spins of the binding partner (*111*). Such changes are referred to as chemical shift perturbations (CSPs). In a CSP analysis, the $^{1}H,^{15}N$ HSQC spectrum of one protein is monitored while the unlabeled interaction partner is titrated in (*57, 112*). Chemical shift perturbation measurements can, in general, yield the location of the binding interfaces on the individual binding partners. Along with mapping the binding site, CSPs can also be indicators of allosteric processes, when residues far away from the binding site show CSP's (*112*). Additionally, if the free and bound states of the interaction partners are in rapid chemical exchange, a series of titration steps can provide an accurate estimate of the dissociation constant (K_d).

2.2.6.5 Paramagnetic relaxation enhancement (PRE)

Paramagnetic relaxation enhancement (PRE) is a method to provide long distance structural information. PRE labels can provide distance information of up to 20 Å (*58*). Additionally, they can also be used to map interactions between proteins (*113*). Paramagnetic molecules cause distance dependent line broadening and loss of intensity in NMR signals. The effect is caused by a transient dipolar interaction between the unpaired electron spin of the paramagnetic label and the NMR active nuclei in its vicinity (up to 20 Å).

2.2.7 NMR sample preparation

2.2.7.1 CSP experiments

An initial stock solution of uniformly ^{15}N-labeled VpUcyt was obtained by dissolving lyophilized ^{15}N-VpUcyt at a concentration of 450 µM in NMR buffer (20 mM sodium phosphate pH 6.2, 100 mM NaCl, 0.02% (w/v) NaN_3, 10% (v/v) $^{2}H_2O$, 100 mM DPC-d38). Weighed, lyophilized CD4mut was dissolved in ^{15}N-VpUcyt stock to give a final CD4mut concentration of 1 mM. A CD4mut dilution series was obtained by adding appropriate amounts of ^{15}N-VpUcyt stock to CD4mut aliquots, resulting in 13 titration steps with uniform ^{15}N-VpUcyt and varying CD4mut concentrations. A $^{1}H,^{15}N$-HSQC spectrum was recorded at each titration step.

The composite chemical shift perturbation, Δδ, takes both the ^{1}H and ^{15}N chemical shift changes into consideration, and was calculated as follows:

$$\Delta\delta = \sqrt{[(\Delta\delta\ ^{1}HN)^{2} + (\Delta\delta\ ^{15}N/5)^{2}]}$$

Here Δδ ^{1}HN and Δδ ^{15}N are the ^{1}H and ^{15}N chemical shift changes for a given CD4 titration step with respect to the chemical shifts of free VpUcyt.

2.2.7.2 PRE experiments

The paramagnetic probe (1-oxyl – 2,2,5,5 – tetramethyl - Δ3 – pyrroline – 3 methyl)-methanethiosulfonate (MTSL) (Toronto Research Chemicals, Canada) was attached to single cysteine variants of CD4mut via disulfide bond formation with the sulfhydryl group of the cysteine. Three plasmids encode for three different single cysteine mutants of the primary CD4mut construct. The corresponding CD4 peptide variants are designated as CD4mutS422C, CD4mutS397C and CD4mutR(-3)C, based on the position and type of amino acid substituted. These positions are marked on the CD4mut sequence in Figure 12. For labelling with MTSL, purified single cysteine CD4mut peptide was dissolved in a mixture of acetonitrile (60 vol%) and H_2O, along with a 7-10 fold molar excess of MTSL. The solution was incubated overnight at room temperature, with gentle shaking. Unbound MTSL was removed by reversed phase chromatography using a Resource RPC column (GE HealthCare, Freiburg). The efficiency of the labelling reaction was checked by electrospray ionization (ESI) mass spectrometry.

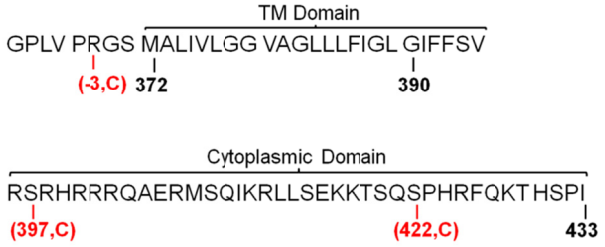

Figure 12: Positions of the spin labels in the CD4mut amino acid sequence

Lyophilised MTSL-linked CD4mut variants were dissolved in aliquots of the ^{15}N-VpUcyt stock (450 µM in NMR buffer) to a final concentration of 600 µM CD4mut. Following acquisition of a ^{1}H,^{15}N-HSQC spectrum in presence of the paramagnetic label, ascorbic acid was added to the sample at tenfold excess over MTSL. After one hour of incubation the spin label was completely reduced (diamagnetic), and a second HSQC spectrum was recorded. The exact procedure was repeated for all three CD4mut variants (CD4S422C, CD4S397C, CD4R(-3)C). The pH at each step was kept constant at 6.2.

3 Results

3.1 Protein production and modification

3.1.1 CD4mut, HisUbiquitinCD4mut and CD4 single cysteine mutants

Expression and purification of all CD4mut related proteins was carried out as detailed earlier (cf. 2.2.3.2). Expression was carried out in the C43(DE3) *E.coli* cell strain. Protein cleavage steps were skipped for purification of HisUbiquitinCD4mut. Purification of the single cysteine mutants was carried out in the same manner as CD4mut, but under reducing conditions (cf. 2.2.3.2). Protein yield for CD4mut and the three CD4 single cysteine mutants was ~1 mg of pure protein per litre of expression culture. For HisUbiquitinCD4mut, the yield was slightly higher, at ~1.5 mg per litre. Protein separation, cleavage and purification were confirmed by SDS-PAGE, as shown in figure 13. The chromatographic steps are shown in figure 14.

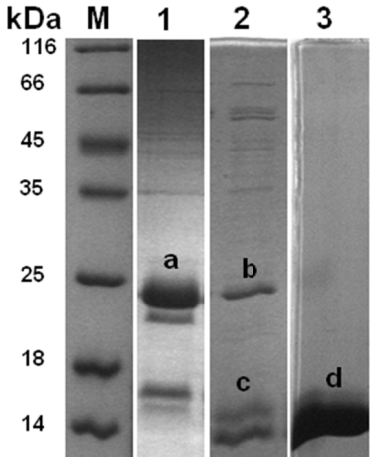

Figure 13: SDS page to track CD4mut purification. Letters **a-d** correspond to the protein bands above which they are placed. HisUbiquitinCD4mut (**a**) after first Ni-NTA affinity chromatography (lane 1). His-tagged PreScission protease (**b**) and His-Ubiquitin (**c**) after cleavage (lane 2). Pure CD4mut (**d**), after removal of **b** and **c** via Ni-NTA affinity chromatography, followed by reverse phase chromatography (lane 3). The lane M corresponds to the unstained protein molecular weight marker (Fermentas).

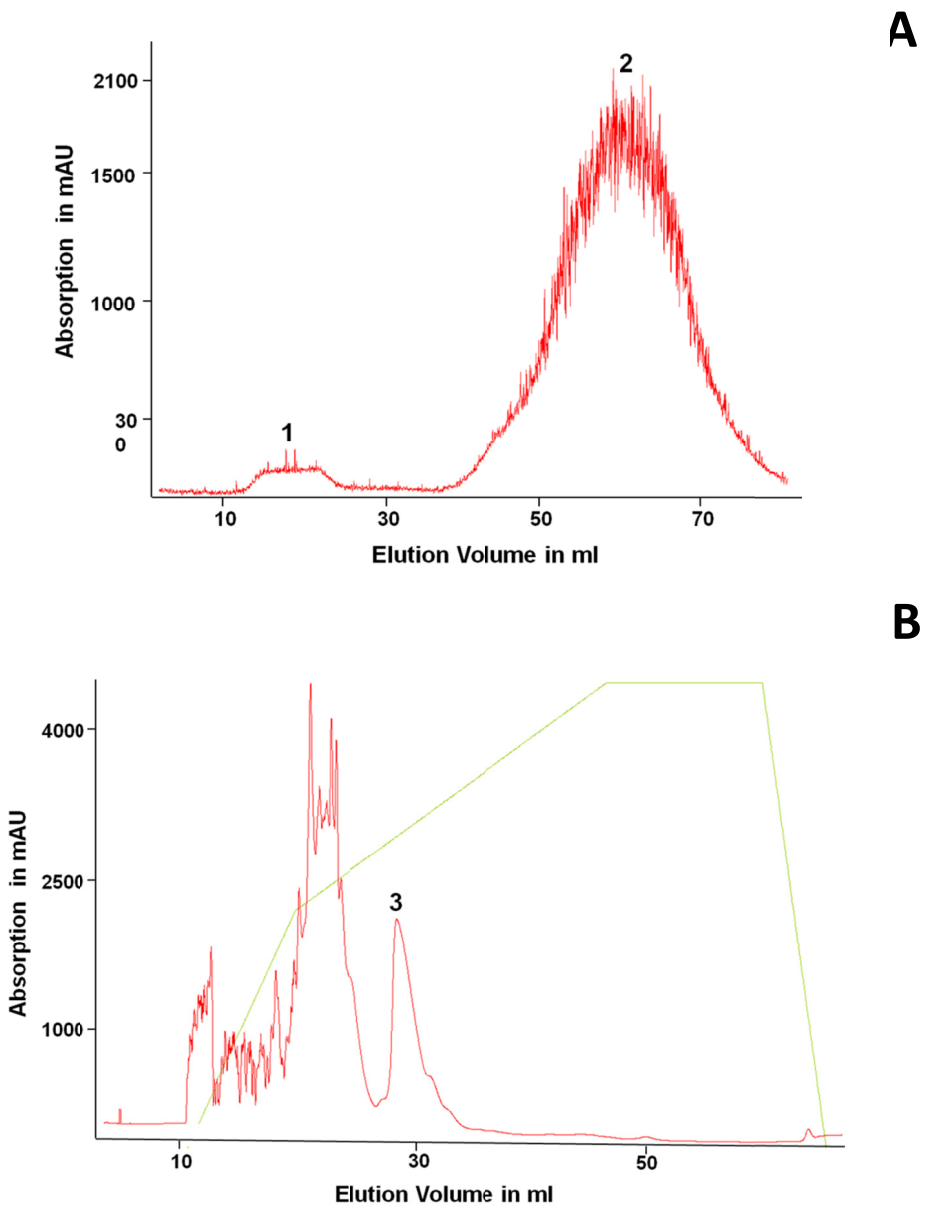

Figure 14: Chromatographic steps involved in CD4mut purification**. A)** Desalting run to separate HisUbiquitinCD4mut **(1)** and imidazole **(2)** using a HiPrep 26/10 Desalting column. **B)** Reverse phase chromatography to obtain pure CD4mut **(3)**, using a Resource 15 RPC, 3 ml column run with a discontinuous gradient from 0 to 100% of 80% acetonitrile, in 0.08% TFA, as the organic solvent. CD4mut elutes at 72% of the gradient **(green line)**. Absorption measured at 214 nm for A and B.

3.1.2 Labelling of CD4 single cysteine mutants with MTSL

The three single cysteine mutants (CD4S422C, CD4S397C, CD4R(-3)C) were labelled with the paramagnetic MTSL as described previously (cf. 2.2.7.2). The efficiency of the labelling reaction was checked by electrospray ionization (ESI) mass spectrometry (Performed by Dr. Beatrix Santiago-Schübel, of the ZCH at the Research Centre Jülich). These results are depicted in figure 15. The mass spectrometry data showed a single protein component with the expected mass of MTSL-labelled CD4S22C. There was no indication of the unlabelled CD4S422C, suggesting that all of the protein was MTSL-labelled. The labelling of the other two cysteine mutants was successfully carried out and verified in the same manner.

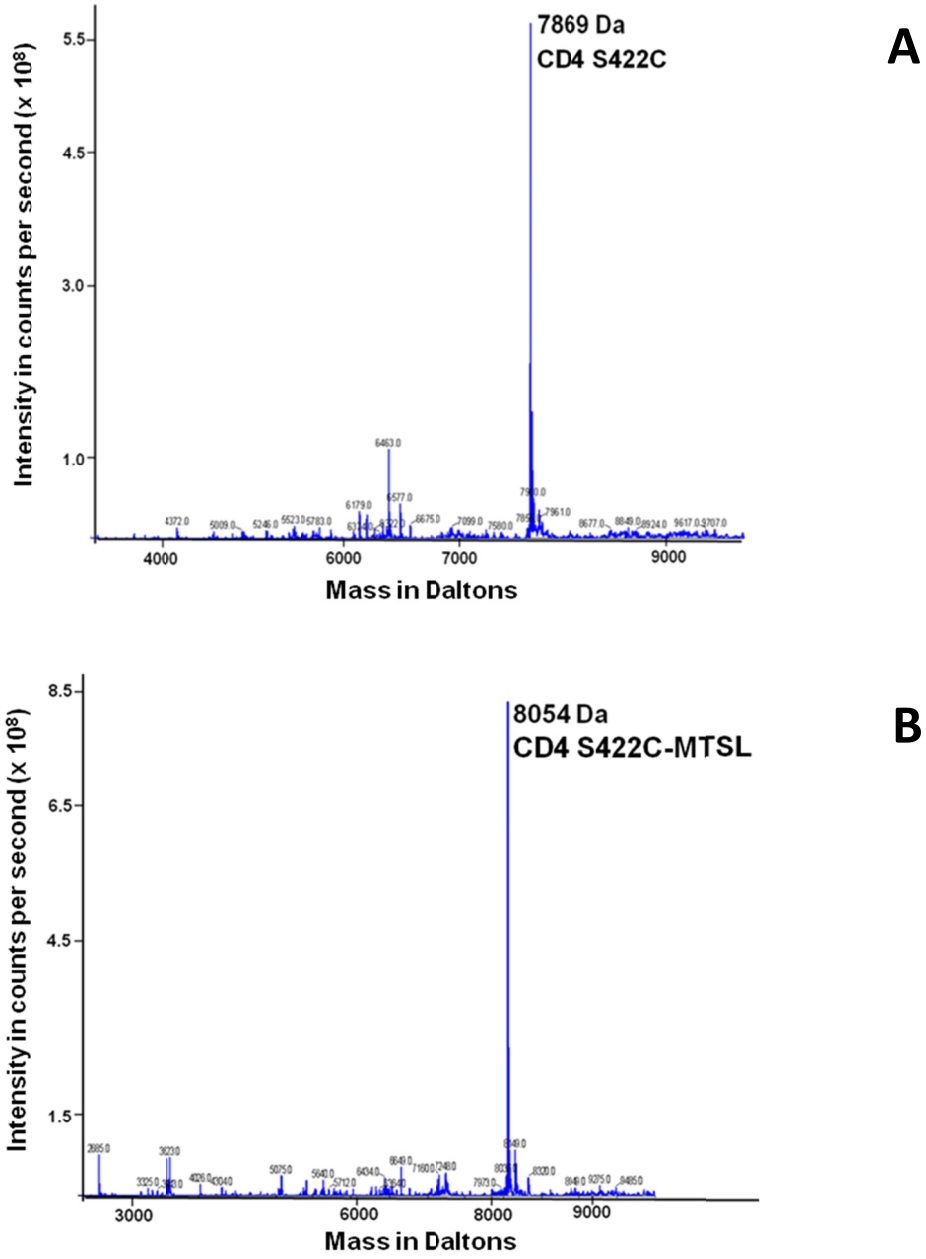

Figure 15: Processed mass spectra confirming MTSL labelling of the CD4 single cysteine mutants using ESI mass spectrometry. **A)** The mass spectrum for unlabelled CD4 shows a single mass peak at 7869 Da. **B)** The label MTSL adds 186 Daltons to the mass of the CD4 molecule. The measured mass of MTSL-labelled CD4 is within the error limits. Data pertains to CD4S422C.

3.1.3 Nef

Expression and purification of Nef was carried out as previously described (cf. 2.2.3.4) Expression was carried out in the BL21-CodonPlus(DE3)-RIL *E.coli* cell strain. Approximately 6 mg of pure Nef was obtained per litre of expression culture. As shown in figure 16, purification was confirmed with SDS-PAGE.

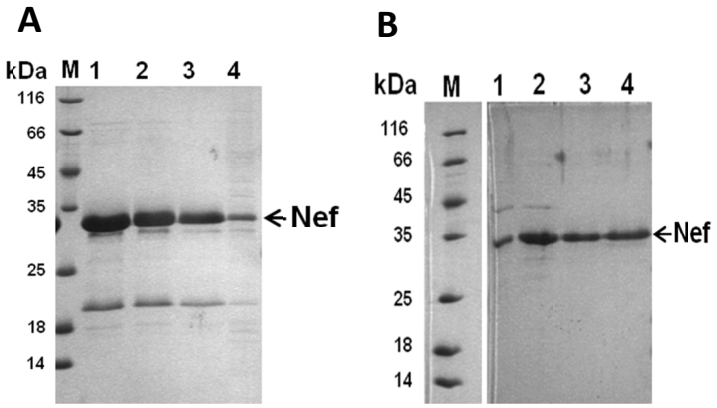

Figure 16: SDS-PAGE to track Nef purification. Samples were applied to a 15% SDS polyacrylamide gel, followed by Coomassie staining**. A)** Nef elution fractions after Ni-NTA affinity chromatography, and imidazole mediated elution (lanes 1-3 with 300 mM imidazole, lane 4 with 500 mM imidazole). **B)** Pure Nef fractions after size exclusion chromatography (lanes 1-4 correspond to four consecutive elution fractions). The lane M corresponds to the unstained protein molecular weight marker (Fermentas). Individual marker band weights are given under kDa (Kilodalton).

3.1.4 VpUcyt

Expression and purification of ^{15}N labelled VpUcyt was carried out as detailed in section (cf. 2.2.3.5). Expression was carried out in the BL21 (DE3) *E.coli* cell strain. Approximately 10 mg of pure VpUcyt was obtained per litre of expression culture. As shown in figure 17, purification was confirmed with SDS-PAGE. The reversed phase chromatographic purification step is shown in figure 18.

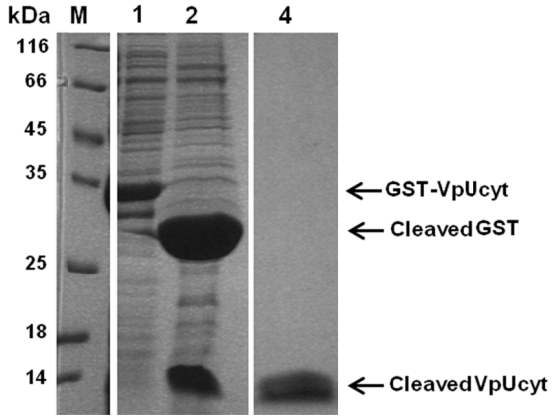

Figure 17: SDS-PAGE to track VpUcyt purification. The uncleaved GST-VpUcyt protein (lane 1) is first purified via affinity chromatography. Cleavage with thrombin results in cleaved GST (lane 2) and VpUcyt (lane 2). Pure VpUcyt (lane 4) is obtained after reverse phase chromatography. The lane M corresponds to the unstained protein molecular weight marker (Fermentas).

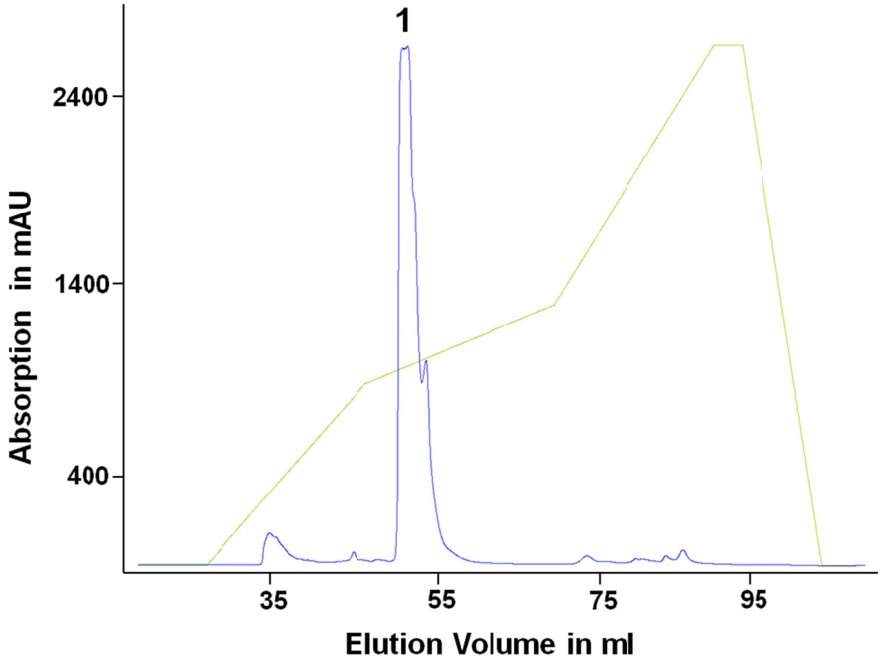

Figure 18: Reverse phase chromatography to obtain pure VpUcyt **(1)**. Reversed phase run was carried out using a Resource 15 RPC, 3 ml column, using a discontinuous gradient from 0 to 100%, of 60% acetonitrile in 50 mM ammonium acetate pH 7.2, as the mobile phase. VpUcyt elutes at 38% of the gradient **(green line)**. Absorption was measured at 214 nm.

3.1.5 MSP

Expression and purification of MSP was carried out as detailed in section 2.2.3.1. Expression was carried out in the BL21 (DE3) *E.coli* cell strain. Approximately 12 mg of pure MSP was obtained per litre of expression culture. As shown in figure 19, purification was confirmed with SDS-PAGE.

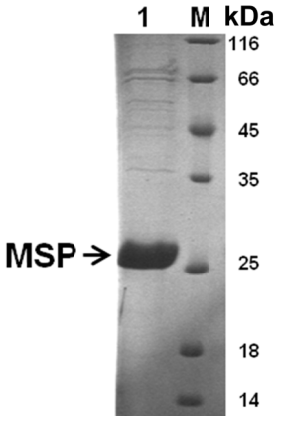

Figure 19: SDS-PAGE to track MSP purification. Purified MSP is marked in lane 1. The lane M corresponds to the unstained protein molecular weight marker (Fermentas). Individual marker band weights are given under kDa.

3.2 Characterizing the CD4-VpU interaction using NMR

3.2.1 $^{1}H,^{15}N$ HSQC of VpUcyt

Firstly, a plain $^{1}H,^{15}N$ HSQC of ^{15}N VpUcyt was recorded in the presence of membrane mimicking DPC micelles. VpUcyt contains residues 39 to 81, which comprise majority of the cytoplasmic domain of the 81 residue VpU protein. The cross-peak positions match those of previous studies that employed the same conditions (*108*). Spectra were recorded at 25 °C at a pH of 6.2 (cf. 2.2.7.1). Figure 20 shows a $^{1}H,^{15}N$ HSQC of VpUcyt in the presence of DPC micelles.

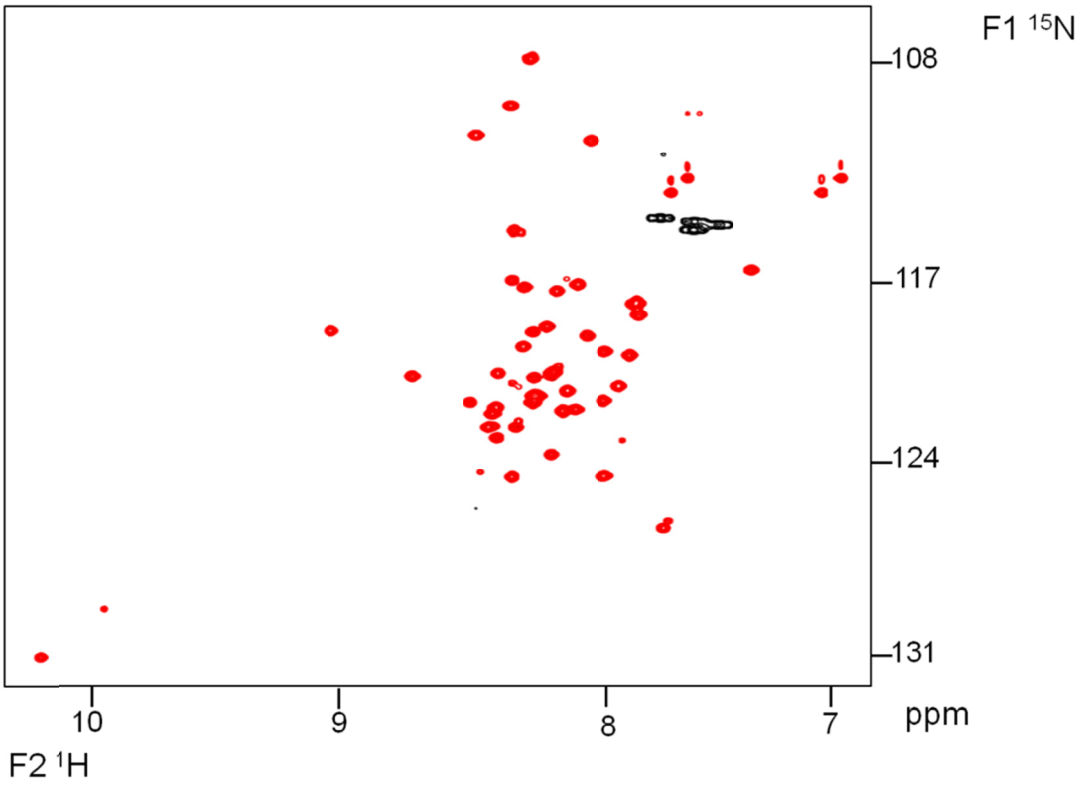

Figure 20: $^{1}H,^{15}N$ HSQC spectrum of ^{15}N VpUcyt, recorded in the presence of membrane mimicking DPC micelles. VpUcyt concentration was 450 µM. NMR buffer composition is 20 mM sodium phosphate pH 6.2, 100 mM NaCl, 0.02% (w/v) NaN_3, 10% (v/v) $^{2}H_2O$, 100 mM DPC-d38. Real backbone or side chain amide peaks are shown in red, while folded in peaks that have their resonance frequencies outside the recorded spectral width are coloured black.

3.2.2. Measurement of chemical shift perturbations (CSPs)

Cross-peak positions observed in $^{1}H,^{15}N$ HSQC spectra of ^{15}N-labelled VpUcyt in a detergent micelle solution (100 mM DPC) are only very weakly dependent on the presence of CD4mut variants in the sample. Therefore, transfer of the previously determined resonance assignment of VpUcyt in 100 mM DPC (*21*) to the observed HSQC cross-peaks was straightforward. Precise determination of cross-peak position and intensity is hampered by peak overlap resulting in partial lack of experimental data for VpUcyt residues 41, 44, 45, 63, 64, 70, 73, and 80, in addition to proline at position 75 (indicated by stars in Figure 21).

A series of thirteen $^{1}H,^{15}N$ HSQC spectra of ^{15}N-labelled VpUcyt (450 µM in presence of 100 mM DPC) were recorded with increasing concentrations of unlabelled CD4mut (0 to 1 mM). The largest chemical shift changes of VpUcyt backbone amide cross-peaks were observed at 1 mM CD4mut and correspond to A66 ($\Delta\delta^{1}$HN = 0.032 ppm) and to E69 ($\Delta\delta^{15}$N = 0.223 ppm) in the ^{1}H and ^{15}N dimension, respectively. The maximum composite CSP amounts to 0.051 ppm, and was also observed for E69. Composite CSPs were calculated as previously stated (cf. 2.2.7.1). The results are shown below in figure 21.

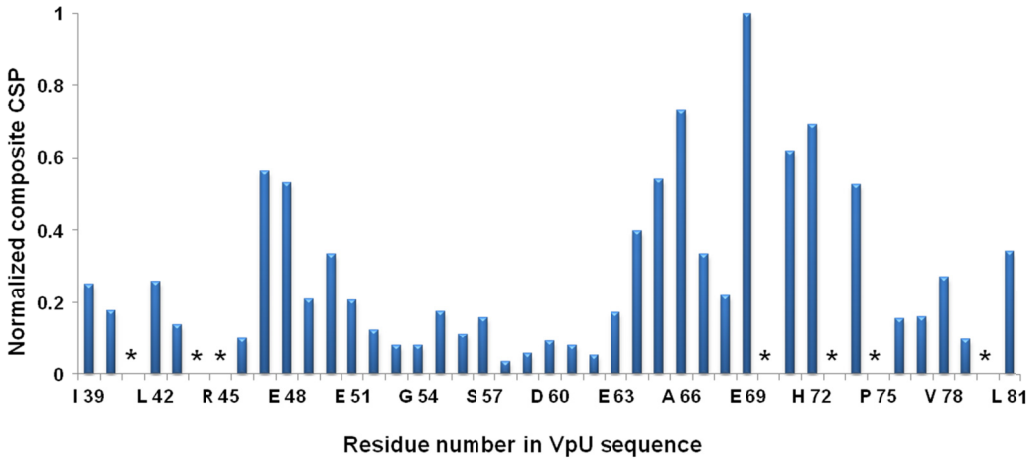

Figure 21: Chemical shift perturbations (CSPs) of VpUcyt residues at maximum CD4mut concentration (1 mM). Based on the ^{1}HN and ^{15}N CSP values, the composite chemical shift perturbations for each peak resonance were calculated. The resulting CSPs were then normalized by scaling the highest shift observed (E69) to a value of 1.0. These values were then plotted as a function of the VpUcyt sequence. (* Data unidentified due to peak overlap, or lack of amide proton, as for proline).

3.2.3 Binding affinity of the CD4mut-VpUcyt interaction

An experimental binding isotherm is obtained directly if the chemical shift of a suitable VpUcyt spin is measured for a series of CD4mut concentrations (*111*). This approach holds good only for rapid exchange between free and CD4-bound VpUcyt. In this case, the observed chemical shift is a time weighted average of the corresponding chemical shift values in the free and bound state. The CSP data thus encodes information on the fraction of CD4-bound VpUcyt molecules in the sample.

Figure 22 depicts the binding isotherm obtained for E69, the residue which shows the maximum CSP. As observed, the shape of the isotherm does indeed indicate complex formation between CD4 and VpUcyt. However, there is no indication of a bound-state plateau at the highest CD4mut concentration studied (1 mM), suggesting that the data may reflect only the rising part of the sigmodial binding isotherm.

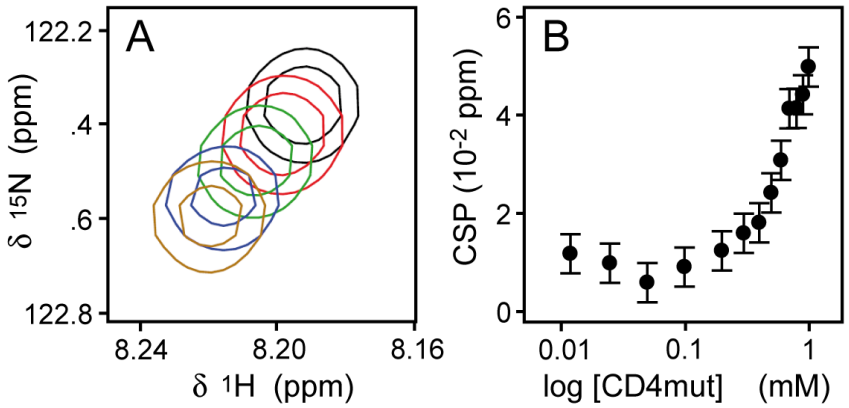

Figure 22: Shift of the E69 cross-peak of VpUcyt in $^{1}H,^{15}N$ HSQC spectra. **A)** Overlay of E69 signal contours from 5 out of 13 titration steps. A linear shift pattern is observed on increasing the CD4mut concentration from 0 (orange) to 1 mM (black). **B)** Composite CSP values relative to the CD4mut-free sample are plotted against the CD4mut concentration for all titration steps.

3.2.4 Quantification of paramagnetic relaxation enhancement (PRE)

A strong PRE effect can be observed by simply overlaying HSQC spectra in the presence and absence of the active MTSL probe. Figure 23 shows the loss of intensities in the VpUcyt HSQC spectrum, due to spacial proximity of the PRE-labelled CD4S422C. Also, the loss of intensity is residue specific, with VpUcyt residues in close proximity to the PRE label (and hence CD4S422C) showing maximum intensity reduction.

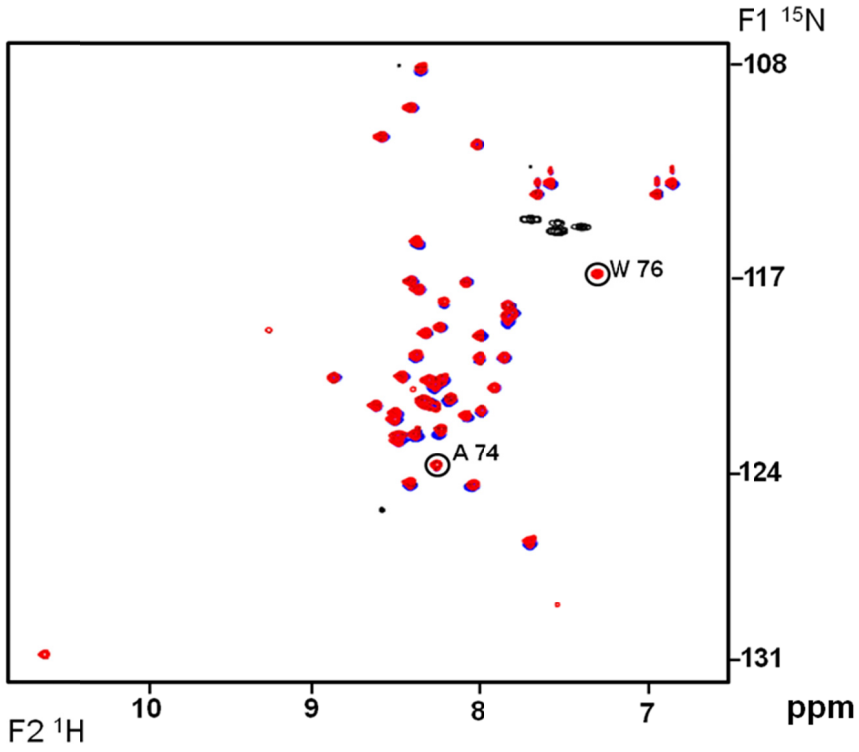

Figure 23: $^{1}H,^{15}N$ HSQC spectrum of ^{15}N-VpUcyt (Red, in the presence of reduced PRE probe) overlaid with a $^{1}H,^{15}N$ HSQC ^{15}N-VpUcyt spectrum showing loss of signal intensities (Blue, in the presence of oxidized PRE probe), due to the spatial proximity of the PRE-labelled CD4S422C. The effect is especially pronounced for certain peaks. A74 and W76 (black circles) experience a near total loss of peak intensities in the presence of the oxidized PRE label. Real backbone or side chain amide peaks are shown in red, while folded in peaks that have their resonance frequencies outside the recorded spectral width are coloured black.

For a quantitative analysis, signal intensities of all the backbone amide cross-peaks in $^{1}H,^{15}N$ HSQC experiments of ^{15}N-labelled VpUcyt were compared in the presence of MTSL-labelled CD4mut variants in the oxidized vs. reduced state of the spin label. The ratio of VpUcyt signal intensities recorded under oxidizing and reducing conditions is referred to as signal retention in presence of the paramagnetic label. Signal retention was calculated separately for the three MTSL-labelled CD4 constructs. A comparison of signal intensities in the presence of oxidized and reduced MTSL label is shown in figure 24. The red bars indicate signal retention for individual VpUcyt residues.

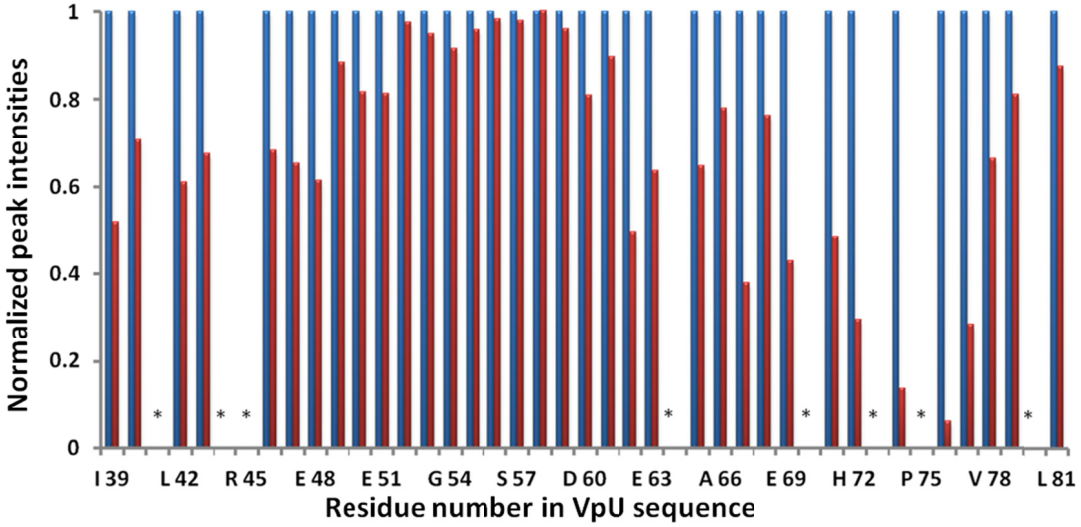
Normalized peak intensities
1
0.8
0.6
0.4
0.2
0
I 39 L 42 R 45 E 48 E 51 G 54 S 57 D 60 E 63 A 66 E 69 H 72 P 75 V 78 L 81
Residue number in VpU sequence

A

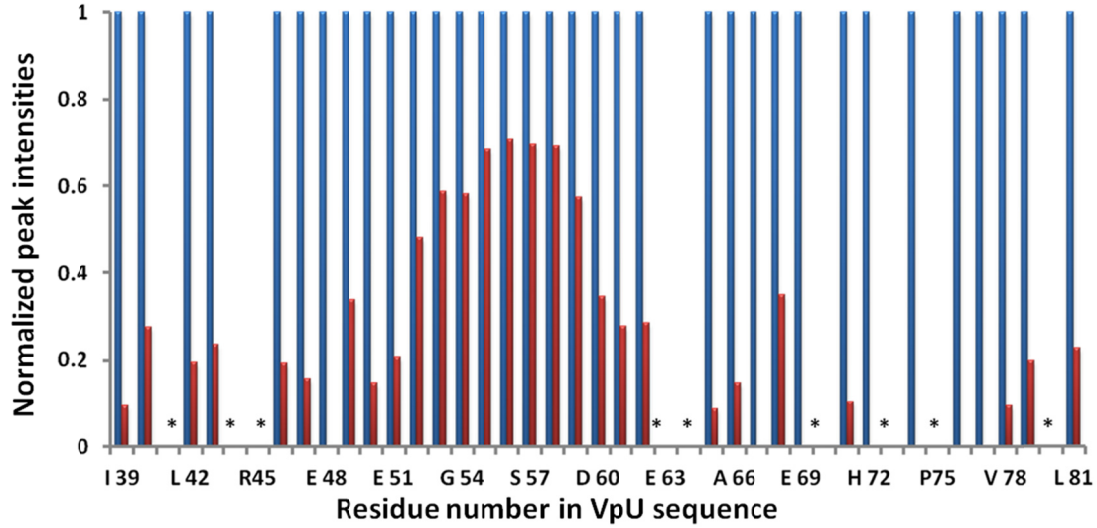
Normalized peak intensities
1
0.8
0.6
0.4
0.2
0
I 39 L 42 R45 E 48 E 51 G 54 S 57 D 60 E 63 A 66 E 69 H 72 P75 V 78 L 81
Residue number in VpU sequence

B

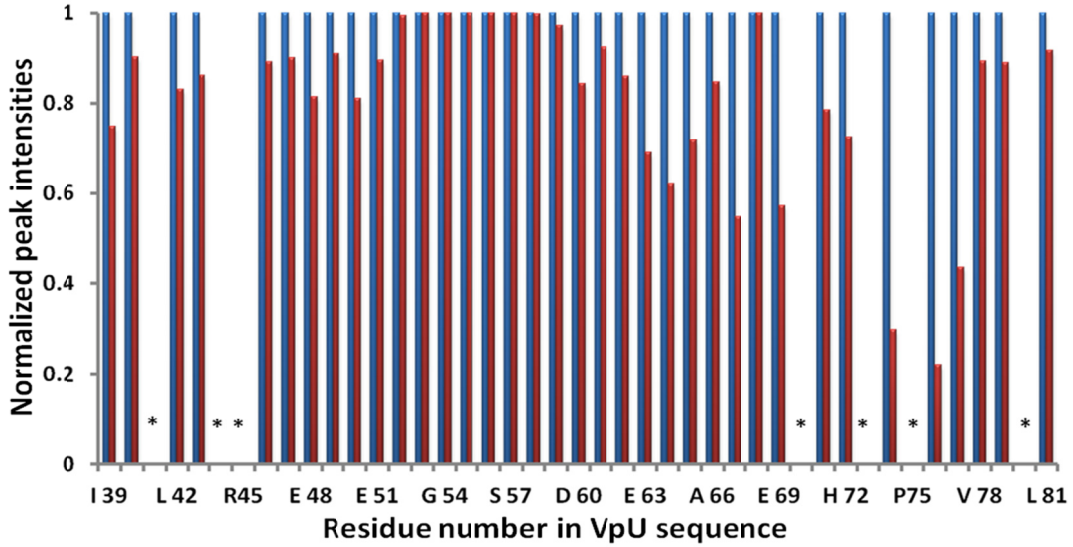
Normalized peak intensities
1
0.8
0.6
0.4
0.2
0
I 39 L 42 R45 E 48 E 51 G 54 S 57 D 60 E 63 A 66 E 69 H 72 P75 V 78 L 81
Residue number in VpU sequence

C

Figure 24: Comparison of intensities for VpUcyt cross-peaks in the presence of reduced (Blue) and oxidized (Red) PRE-labelled CD4mut, as a function of VpUcyt residue number. The reduced PRE label is no longer a strong source of relaxation for neighbouring nuclei. This causes a reversal of the effects (peak broadening, loss of peak intensities) seen with the oxidized label. Each peak intensity was normalized to the reduced state intensity, i.e., the measured intensity of a peak is divided by the intensity of the same cross-peak observed in the reduced state. The intensity comparison was then plotted as a function of the VpUcyt sequence. Intensity comparisons are shown for the CD4S422C **(A)**, CD4S397C **(B),** and CD4R(-3)C **(C)** constructs. Red bars indicate signal retention. All samples contained 450 µM VpUcyt and 600 µM CD4mut. (* Data unidentified due to peak overlap, or lack of amide proton, as for proline).

3.3 Nanodisc assembly

The preparation of nanodiscs used in this work is largely based on a protocol developed by Sligar and colleagues (*90, 91*).

The MST experiments described here require the usage of fluorescently labelled nanodiscs. Accordingly, fluorescently labelled lipids were added to the nanodisc assembly mixture (cf. 2.2.4.1).

Nanodiscs were prepared with a principal lipid, along with a small amount of fluorescently labelled lipid (cf. 2.2.4.1). Nanodiscs assembled with POPC as the principal, and Atto 647N DMPE as the fluorescently labelled lipid, were designated as POPC-Atto 647N nanodiscs. Similarly, nanodiscs assembled with DMPC as the principal, and Atto 488 DMPE as the fluorescent lipid, were designated as DMPC-Atto 488 nanodiscs. The fluorescently labelled lipids could be tracked using their specific absorption wavelengths (645 nm for Atto 647N or 501 nm for Atto 488).

Figure 25 shows the final step in assembly of CD4mut-loaded POPC-Atto 647N nanodiscs, wherein size exclusion chromatography is used to separate assembled nanodiscs from free MSP, free lipids and possibly detergent molecules. Both loaded and empty nanodiscs are obtained in this manner. As seen, nearly all the fluorescent lipids elute with the standard nanodisc peaks, thus confirming the assembly of fluorescently labelled nanodiscs. The presence of CD4mut in the nanodiscs was

confirmed by SDS-PAGE. Assembly could be successfully repeated for DMPC-Atto 488 nanodiscs.

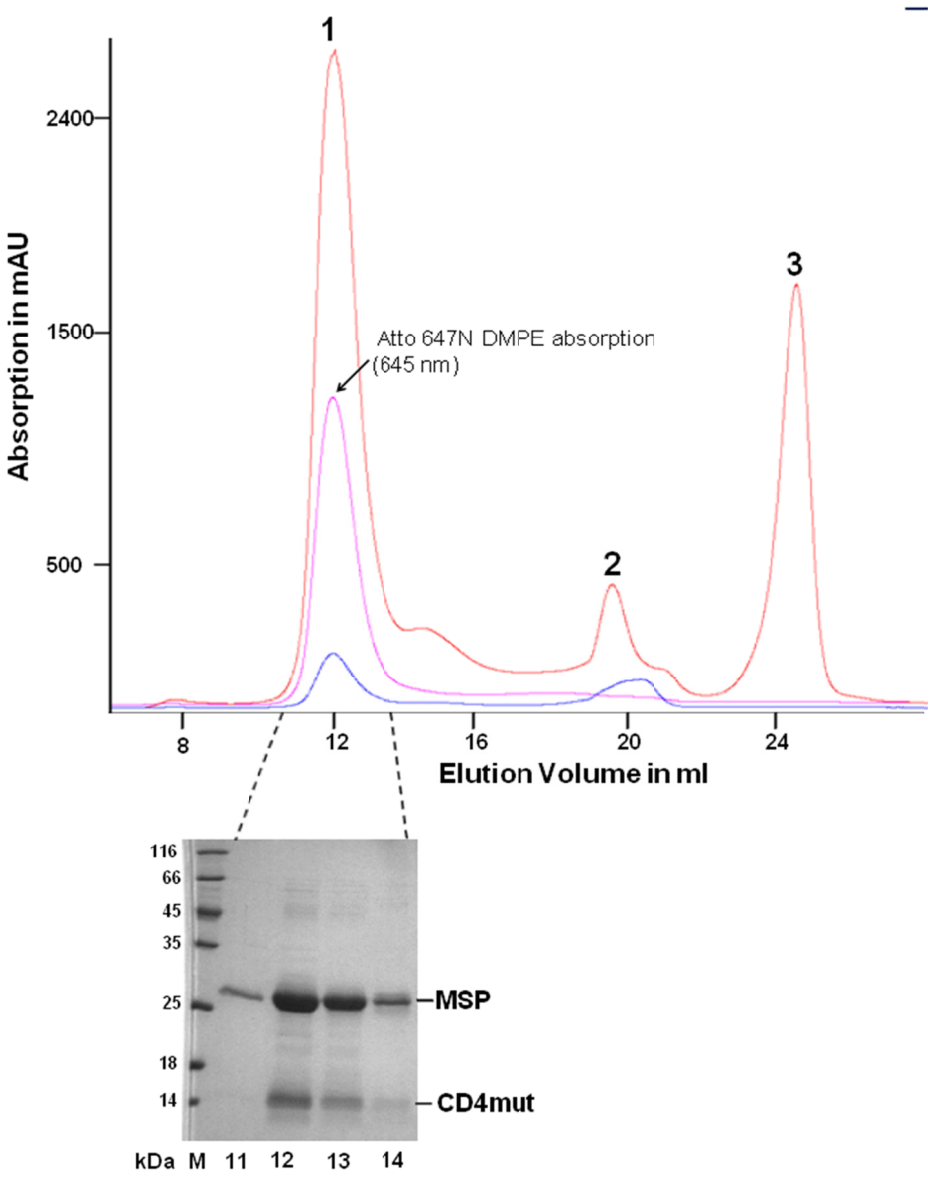

Figure 25: Size exclusion chromatography for the separation of CD4mut-loaded POPC-Atto 647N nanodiscs. Absorption at 214, 645 and 280 nm is depicted by red, pink and blue lines respectively. Based on a calibration with globular proteins, the nanodisc peak **(1)** corresponds to a molecular weight of ~150 kDa. The absorption at 645 nm corresponds to that of the dye, Atto 647N. SDS-PAGE analysis of elution volumes 11 through 14 ml confirms the presence of MSP and cleaved CD4mut. The absorption profile for Atto 647N confirms that nearly all labelled lipids are incorporated into the nanodiscs. The presence of free MSP **(2)** was also confirmed by SDS-PAGE. A late peak showing a relatively high absorption at 214 nm **(3)** may

correspond to a mixture of lipids and detergent molecules. The lane M denotes the unstained protein molecular weight marker (Fermentas), while kDa corresponds to the individual marker band weights.

Optimization of nanodisc assembly was obtained by first varying the MSP:lipid ratio. For POPC-Atto 647N nanodiscs, ratios of 1:70, 1:60 and 1:50 were first tested, with 1:60 being identified as the ideal ratio. For CD4mut-loaded nanodiscs, this ratio was reduced to 1:55, to account for the lipids displaced by the insertion of CD4mut.

For DMPC-Atto 488 nanodiscs ratios of 1:90, 1:80, 1:70 and 1:60 were first tested, with 1:70 being identified as the ideal ratio. For Vpr-loaded nanodiscs, assembly was carried out by adding a weighed, lyophilized powder to preformed unloaded nanodiscs (1:70). Any displacement of lipids in this case was probably spontaneous.

Based on the above experiments, the types of nanodiscs produced and their relevant properties are listed in table 13.

Regarding the actual compositions of the assembled nanodiscs, the stated concentrations of the individual components are merely approximations based on the ratios of these components in the initial assembly mixture.

Table 13: Types of nanodiscs produced, and their relevant properties

Nanodisc	Principle lipid	Fluorescent lipid	Fluorescent dye absorption (nm)	Ratio of fluorescent lipid: Principle lipid:	Ratio of MSP:Principle lipid	Membrane proteins incorporated
POPC Atto 647N	POPC	Atto 647N-DMPE	645	1:60	1:60	CD4mut, HisUbiquitinCD4mut
DMPC-Atto 488	DMPC	Atto 488-DMPE	501	1:70	1:70	Vpr

3.3.1 Nanodisc stability and storage

Nanodisc stability was checked using size exclusion chromatography. Pure nanodisc solutions elute at a specific volume, and as a single peak (peak 1 in figure 25, cf. 3.3). Aggregation of nanodiscs is detected by the presence of peaks in the void volume of the size exclusion run. Both POPC-Atto 647N and DMPC-Atto 488 nanodiscs could be stored at 4 °C for up to 6 weeks, without aggregating or precipitating. For longer storage periods, nanodisc solutions were shock frozen in liquid nitrogen and stored at 80 °C. All nanodisc solutions containing fluorescent lipids were stored in containers covered with aluminium foil. For MST experiments, nanodisc solutions were stored in low binding tubes (Biozym Scientific). Nanodisc aggregation can be prevented by the addition of small amounts of detergents, or by filtering them through nucleopore membranes (cf. 2.2.5).

3.4 Microscale thermophoresis (MST)

3.4.1 Establishing a protocol to employ nanodiscs in MST studies

The initial work concentrated on establishing a protocol to study binding between a nanodisc-inserted membrane protein and its soluble protein ligand. An important aspect when using membrane mimetics like nanodiscs, is establishing conditions wherein they maintain their structural and functional integrity. The following aspects were crucial while developing the protocol.

3.4.1.1 Nanodiscs adsorb to capillary walls

MST experiments are conducted by loading samples into thin glass capillaries. In addition to the standard capillaries, there are capillaries with chemically modified surfaces to suit certain sample types (cf. 2.2.5).

A recurring issue when using nanodiscs, is their adsorption to the walls of capillaries used in MST experiments. Adsorption to the capillary walls is seen with all five capillary types (standard, hydrophilic, hydrophobic, enhanced gradient, BSA-coated). Figure 26 depicts the adsorption of POPC-Atto 647N nanodiscs. Adsorption to the capillary walls can be detected by U-shaped profiles that are seen in the initial capillary scans. The capillary scan measures the fluorescence levels in each capillary. Also, experiments run with these samples show extreme bumpiness in their raw data. Bumpy raw data is synonymous with sample aggregation. Experiments were run at 25 °C, in a buffer containing 10 mM sodium phosphate pH 7.4, 150 mM NaCl. Similar behaviour was observed with DMPE-Atto 488 nanodiscs.

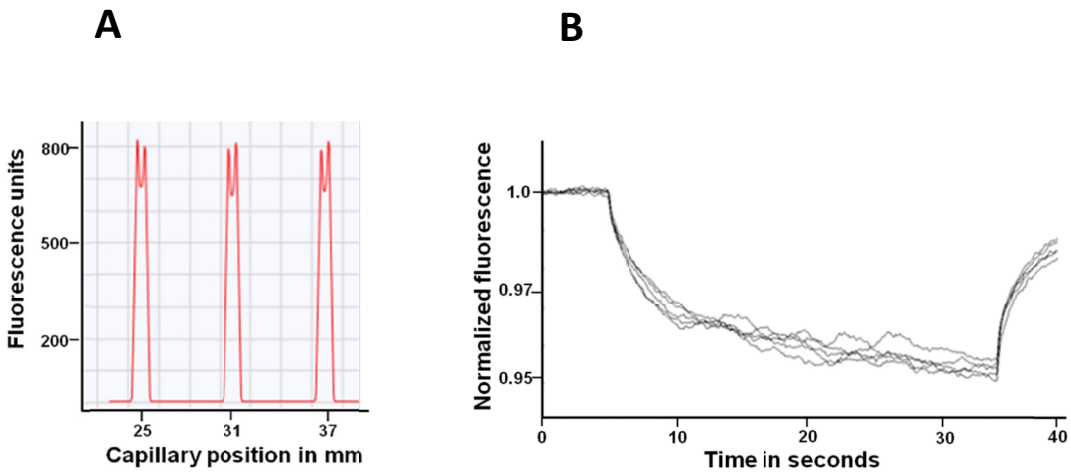

Figure 26: Adsorption of POPC-Atto 647N nanodiscs to standard capillaries. **A)** The U-shaped curves seen in the capillary scan are an indicator of sample adsorption to the capillary walls. **(B)** The time traces (Raw data) obtained from these samples are extremely bumpy, suggestive of sample aggregation. Experiments were run at 25 °C, in a buffer containing 10 mM sodium phosphate pH 7.4, 150 mM NaCl.

3.4.1.2 Strategies to prevent nanodisc adsorption

Introducing the following steps helped prevent the adsorption of nanodiscs to the capillary walls.

3.4.1.2.1 Supplementation with additives

The supplementation of the buffers with certain additives has been shown to prevent adsorption of the molecules of interest to the capillary walls (*65*). A table of these additives and their relevant properties has been listed (cf. 2.2.5.4).

For POPC-Atto 647N nanodiscs, addition of detergents like DPC (0.005%) and traditional blocking agents like BSA (0.005%) did not prevent nanodisc adsorption to the capillary walls. This was observed with all five capillary types. The addition of CTAB (0.005%) did prevent adsorption for solutions containing only nanodiscs. However, while studying the Nef-CD4 interaction, the addition of CTAB caused precipitation of Nef, and subsequent adsorption of nanodiscs to the capillary walls.

The CTAB-mediated Nef precipitation was also seen in the absence of nanodiscs. When using standard or hydrophobic capillaries, both Tween 20 (0.005%) and SDS (0.005%) prevented nanodisc adsorption to the capillary walls. However, these effects were longer lasting for nanodiscs supplemented with SDS. Nanodiscs in SDS-containing buffer show no signs of adsorption to the capillary walls, even after three weeks storage. In contrast nanodiscs in Tween 20-containing buffer may begin to adsorb after 3 to 4 days. The above results are applicable to unloaded, as well as HisUbiquitinCD4mut- and CD4mut-loaded POPC-Atto 647N nanodiscs. Figure 27 depicts the capillary scan and raw data for unloaded POPC-Atto 647N nanodiscs in the presence of SDS (0.005%). Experiments were run at 25 °C, in a buffer containing 10 mM sodium phosphate pH 7.4, 150 mM NaCl, 0.005% SDS. As can be seen, the adsorption is completely prevented, and the resultant raw data does not exhibit any bumpiness.

For DMPC-Atto 488 nanodiscs, addition of BSA (0.005%) prevented capillary adsorption in hydrophilic capillaries. These results could not be reproduced in other capillary types. Also, nanodiscs begin to adsorb to the capillary walls after 4-5 days. The results are applicable to unloaded and Vpr-loaded DMPC-Atto 488 nanodiscs.

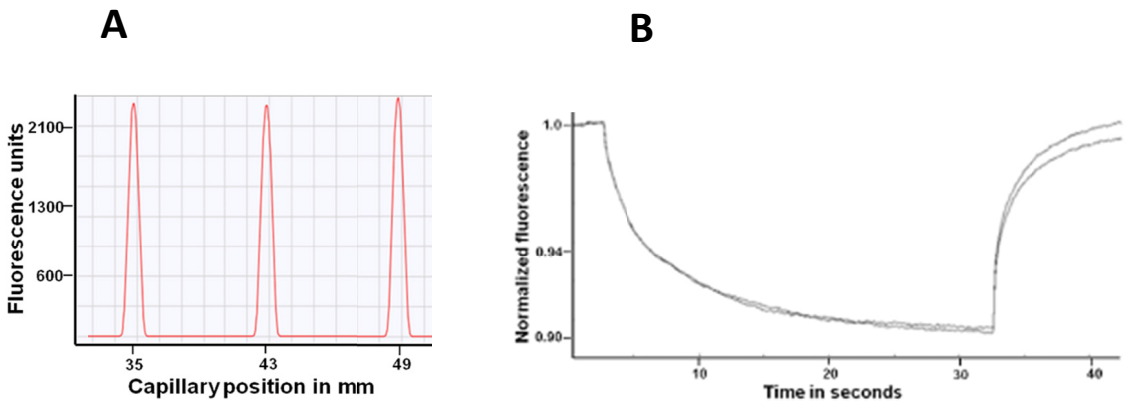

Figure 27: Effect of SDS on the nanodisc adsorption to standard capillary walls. **(A)** Capillary scans for unloaded POPC-Atto 647N nanodiscs show an inverted V shape, indicating the absence of sample sticking. **(B)** Also, the raw data is smooth, with no traces of the bumpiness as seen in the absence of SDS. Experiments were run at 25 °C, in a buffer containing 10 mM sodium phosphate pH 7.4, 150 mM NaCl, 0.005% SDS.

3.4.1.2.2 Filtration of nanodiscs

The methodology for the filtration of nanodiscs has been previously described (cf. 2.2.5.5).

POPC-Atto 647N nanodisc samples were spun down at 13000 x g for 5 min at room temperature. The nanodisc solution was then gently passed through a 50 nm nuclepore track-etched polycarbonate membrane. The solution was analyzed within 1 hour after filtration. Filtered nanodsics showed no signs of adsorption to the capillary walls for standard and hydrophobic capillaries. However, they begin to adsorb to the walls after 4-5 hours. The above results are applicable to unloaded, as well as HisUbiquitinCD4mut- and CD4mut-loaded POPC-Atto 647N nanodiscs. Figure 28 depicts the capillary scan and raw data for filtered unloaded POPC-Atto 647N nanodiscs. Experiments were run at 25 °C, in a buffer containing 10 mM sodium phosphate pH 7.4, 150 mM NaCl.

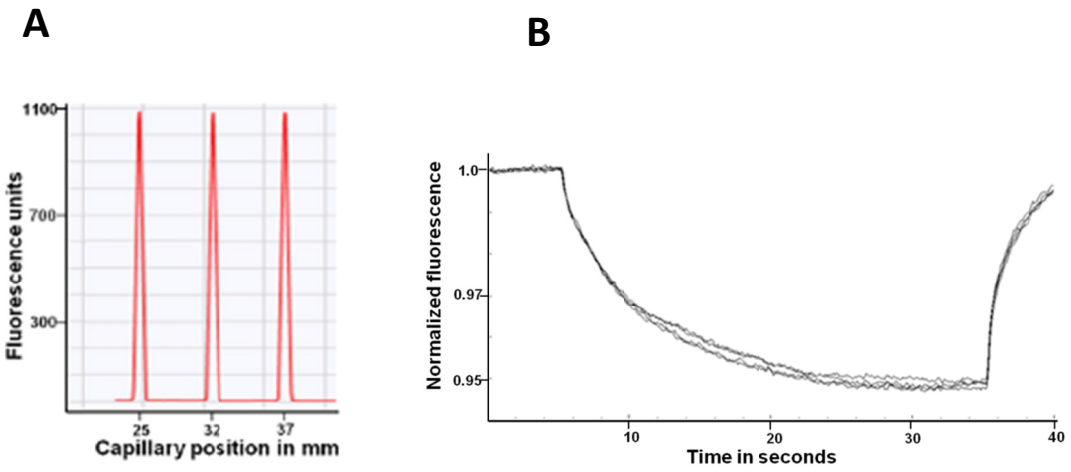

Figure 28: Effect of filtration on the nanodisc adsorption to standard capillary walls. **(A)** Capillary scans for unloaded POPC-Atto 647N nanodiscs show an inverted V shape, indicating the absence of sample sticking. **(B)** Also, the raw data is smooth, with no traces of bumpiness. Experiments were run at 25 °C, in a buffer containing 10 mM sodium phosphate pH 7.4, 150 mM NaCl.

3.4.1.3 Laser Power

Laser power denotes heating power, and has a strong influence on thermophoresis. Its value can be varied from 10% to 100% (Corresponding voltage setting: 0.5 V to 2 V). Figure 29 shows the raw data for POPC-Atto 647N nanodiscs, measured at 20% and 100% laser power. As seen, the raw data for 20% laser power is noisy, irreproducible, with negligible sample depletion. This behaviour was seen with standard and hydrophobic capillaries. In contrast, the data at 100% laser power is smoother, reproducible, and similar to a typical thermophoretic curve (Figure 7, cf. 1.4.2.3). Experiments were run at 25 °C, using standard' capillaries, in a buffer containing 10 mM sodium phosphate pH 7.4, 150 mM NaCl, 0.005% SDS.

For DMPC-Atto 488 nanodiscs, smooth reproducible raw data could be obtained at different laser powers (20%, 40% and 80%). Experiments were run at 25 °C, using hydrophilic capillaries, in a buffer containing 10 mM sodium phosphate pH 7.4, 150 mM NaCl, 0.005% BSA.

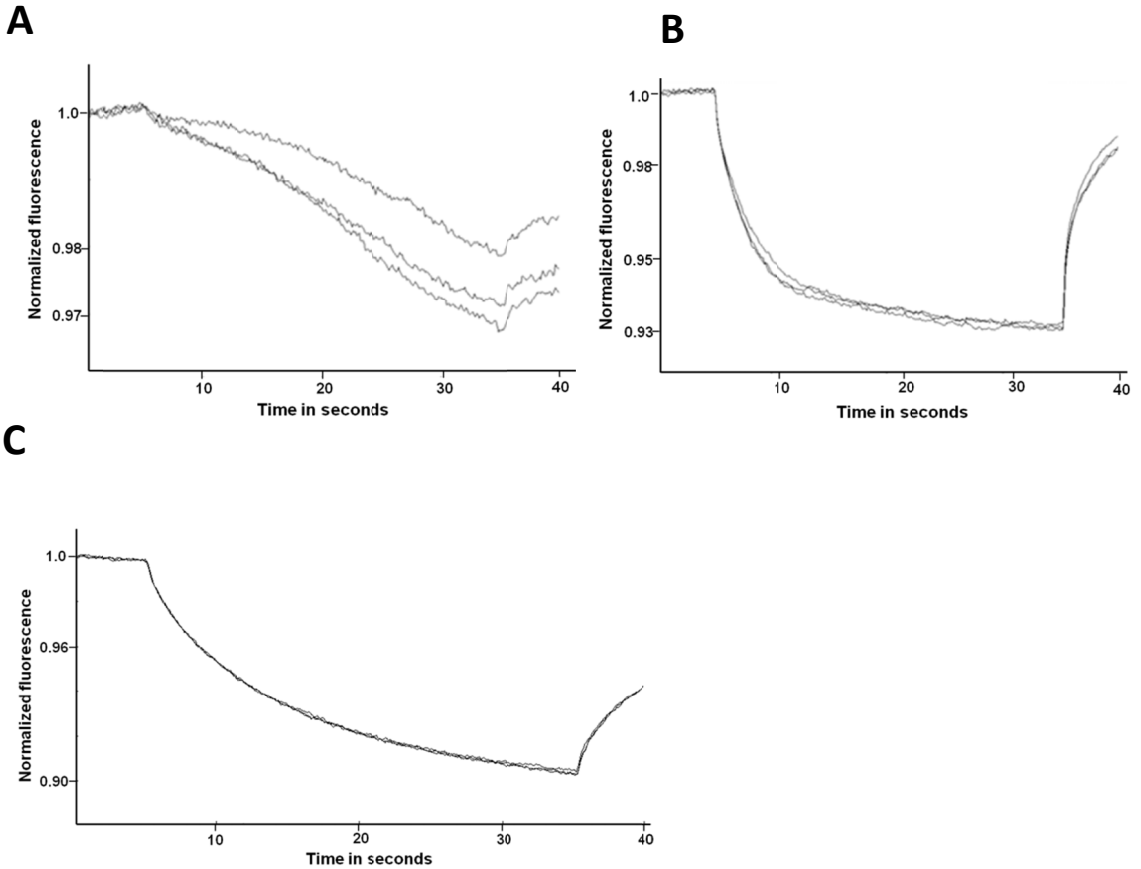

Figure 29: Effect of laser power on data quality. **(A)** Raw data for POPC-Atto 647N nanodiscs obtained at 20% laser power is noisy, irreproducible, and with negligible sample depletion. **(B)** In contrast, raw data at 100% laser power is smoother, reproducible, and similar to a typical thermophoretic curve. **(C)** DMPC-Atto488 nanodiscs show satisfactory raw data even at 20% laser power. This could be repeated at 40%, and 80% laser power.

3.4.1.4 Establishing parameters to study nanodiscs

Based on the initial standardization experiments, the important parameters for studying POPC-Atto 647N and DMPC-Atto 488 nanodiscs were established. They are listed in table 14.

No	Parameter	POPC-Atto 647N nanodiscs	DMPC-Atto 488 nanodiscs
1.	Capillaries	Standard	Hydrophilic
2.	Additives	0.005% SDS	0.005% BSA
3.	Filtration	1x through a 50 nm nucleopore membrane	Not tested
4.	Laser power	100%	20%, 40%, 80%

Table 14: List of optimized parameters established for studying POPC-Atto 647N and DMPC-Atto 488 nanodiscs.

3.4.1.5 Nanodisc storage

Prior to capillary loading, all nanodiscs samples were stored in low binding tubes (Biozym Scientific), designed to reduce sample adsorption to the tube walls. Nanodisc solutions showed minimal binding (< 10%) to the walls of the low binding tubes. Storage in normal, generic tubes increases sample adsorption, leading to large errors in the assumed sample concentration, and consequently the results of the experiment.

3.4.2 Interaction studies involving nanodiscs and MST

3.4.2.1 Interaction between Nef and HisUbiquitinCD4mut-loaded POPC nanodiscs

MST was used to detect binding between HisUbiquitinCD4mut-loaded POPC-Atto 647N nanodiscs, and the soluble Nef protein. The binding between Nef and unloaded POPC-Atto 647N nanodiscs was measured as a negative control. Experiments were run at 25 °C using standard capillaries, in a buffer containing 10 mM sodium phosphate pH 7.4, 150 mM NaCl. Nanodisc samples were filtered prior to running the experiment (cf. 2.2.5.5). All samples were stored in low binding tubes (Biozym scientific), and spun down (13,000 x g for 5 min) before capillary loading.

Nanodisc concentration was kept constant at 50 nM in each capillary. Nef concentration was varied from 11.5 µM to 0.3 nM. Using higher Nef concentrations proved difficult, due to its propensity to precipitate at higher concentrations. Data was acquired at 100% laser power, and fit using the NTAnalysis software (Nanotemper Technologies, Munich), assuming a 1:1 binding model. The calculated dissociation constant (K_d) for the interaction between Nef and HisUbiquitinCD4mut-loaded nanodiscs was 0.21±0.03 µM. However, binding of Nef to unloaded nanodiscs also yielded a similar K_d (0.33±0.03 µM). Results are shown in figure 30.

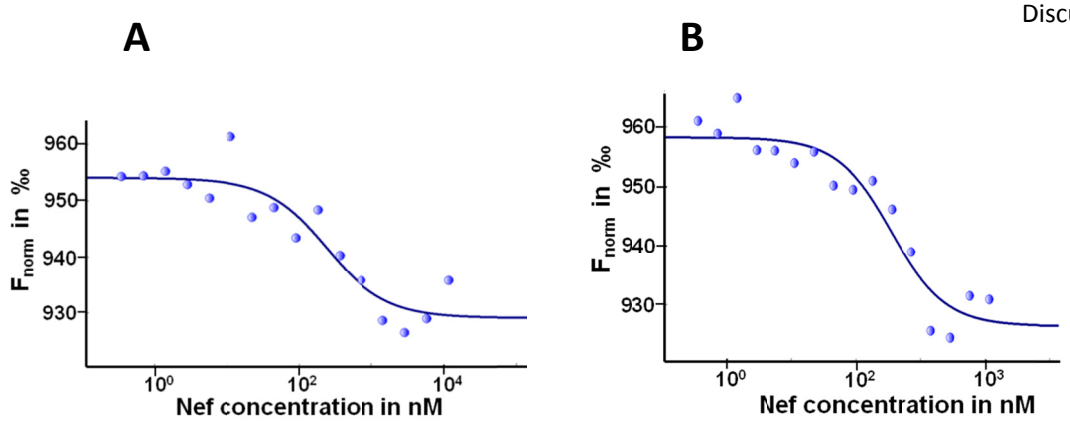

Figure 30: Interaction of Nef with HisUbiquitinCD4mut-loaded, and unloaded POPC-Atto 647N nanodiscs. **(A)** Nef binding to HisUbiquitinCD4mut-loaded nanodiscs yields a K_d of 0.21±0.03 µM. **(B)** However, the binding of Nef to unloaded nanodiscs yields a similar K_d of 0.33±0.03 µM. This experiment was meant to serve as a negative control.

3.4.2.2 Interaction between a p6 peptide and Vpr-loaded DMPC-Atto 488 nanodiscs

MST was used to study binding between Vpr-loaded DMPC-Atto 488 nanodiscs and the p6 peptide (cf. 2.1.2). Nanodisc assembly was carried out as previously described (cf. 2.2.4). The p6 peptide was produced by chemical synthesis (JPT Peptide Technologies, Berlin).

Experiments were run at 25 °C and 40% laser power, using hydrophilic capillaries in a buffer containing 10 mM sodium phosphate pH 7.4, 150 mM NaCl, 0.005% BSA. Nanodisc concentration was kept constant at 5 nM in each capillary. P6 peptide concentration was varied from 190 µM to 5 nM. Data was fit using the NTAnalysis software (Nanotemper Technologies, Munich), assuming a 1:1 binding model. The calculated dissociation constant (K_d) was 32.9±3.9 µM. The binding of p6 to empty nanodiscs was tested as a negative control, under the same experimental conditions. No significant interaction was seen between p6 and unloaded nanodiscs. All experiments were then repeated at 32 °C, using 20% laser power. All other experimental conditions were kept the same. This experiment yielded a dissociation constant of 37.1±2.7 µM. For both experiments, a clear distinction can be observed between p6 binding to Vpr-loaded and empty nanodiscs. Results are shown in figure 31.

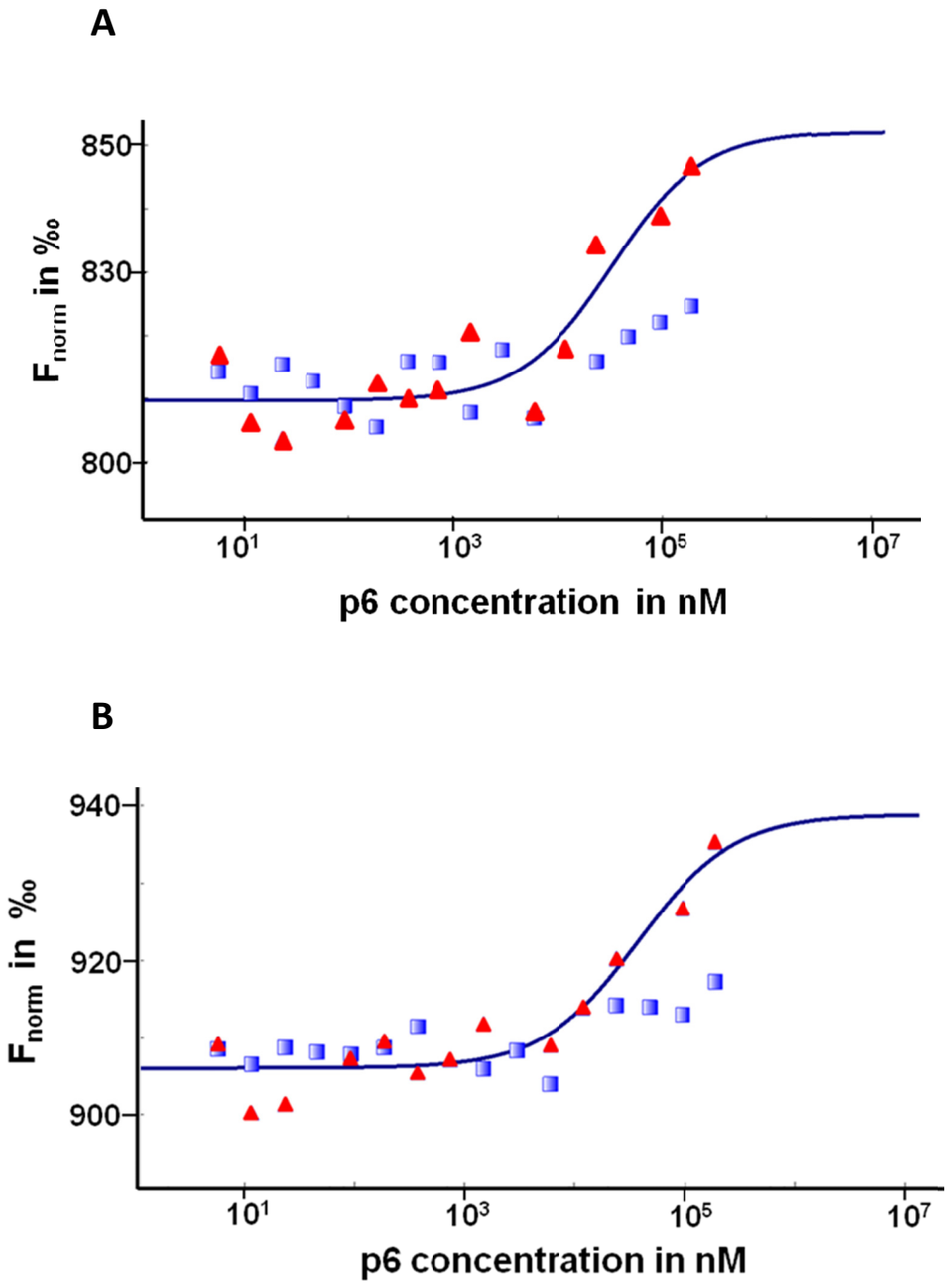

Figure 31: Interaction of Vpr-loaded DMPC-Atto 488 nanodiscs and the soluble p6 peptide. Binding between p6 and Vpr-loaded nanodiscs (▲) can be distinguished from p6 binding to empty nanodiscs (■). **A)** Experiments performed at 25 °C using 40% laser power yielded a K_d of 32.9±3.9 µM. **B)** Experiments repeated at 32 °C, using 20% laser power yielded a K_d of 37.1±2.7 µM.

4 Discussion

4.1 CD4-VpUcyt interaction

4.1.1 Rationale for employing NMR

The downregulation and ultimate degradation of CD4 is a crucial step in the life cycle of HIV-1. VpU-mediated downregulation of CD4 employs a complex degradation pathway, initiated by the physical binding of VpU to CD4s.

While the mechanism of VpU-dependent CD4 downregulation has become clearer during the last few years, there is still only limited knowledge regarding the exact region of VpU that binds CD4. Current estimates are predominantly based on results from mutational studies and other techniques central to cell and molecular biology. These studies suggest that the cytoplasmic domain of VpU is essential for binding CD4, while the CD4 cytosolic residues 414-419, as well as a putative α-helical structure in the membrane proximal region of the cytoplasmic domain of CD4 are critical for binding VpU. However, a sensitive biophysical technique like liquid NMR can provide a more accurate map of binding regions for protein-protein interactions (*57*).

Using an appropriate approach, NMR can map interaction sites with atomic resolution. By employing a suitable membrane mimetic, the technique can be extended to studies on membrane proteins. NMR is also sensitive to weak protein-protein interactions, which may go undetected when using other biophysical techniques (*114*).

Additionally, the three dimensional structure of VpUcyt in the presence of membrane mimicking DPC micelles, but in the absence of CD4 has been previously solved using liquid NMR. Certain data from this study, like the backbone assignment of VpUcyt residues could be transferred for use in the current study. Combining this data with results obtained from techniques like CSP and PRE allows one, in principle, to pinpoint the exact VpUcyt residues involved in binding CD4.

4.1.2 Chemical shift perturbation analysis (CSP)

Ligand binding usually affects the electron current density in the immediate vicinity of the binding site, resulting in localized chemical shift changes for nuclear spins of the binding partner. Such changes are referred to as chemical shift perturbations (CSP) (*115*). In order to gain insights into the CD4 binding site on VpUcyt, a series of thirteen $^{1}H,^{15}N$ HSQC spectra of ^{15}N-labelled VpUcyt (450 µM in presence of 100 mM DPC) with increasing concentrations of unlabelled CD4mut (0 to 1 mM) were recorded. Many of the VpUcyt cross-peak positions remained virtually unchanged during the titration. However, a significant number of peaks showed small and continuous shifts with increasing CD4mut concentration. This behaviour is typical for rapid exchange of the monitored species between free and bound states on the chemical shift time scale. Such fast exchange is often seen for weak interactions (*57*). It is characterized by only a single set of resonances, whose chemical shifts are the fractionally weighted average of the free and bound state chemical shifts. The resonances move in a continuous fashion during titration. In addition to the magnitude of CSPs, information can also be obtained from the rate of chemical shift changes of the individual trajectories, and the uniformity of the direction they take with successive titration steps. A single binding event is indicated if all trajectories occur at the same rate and are linear. However, if trajectories occur at a different rate and/or are curved, there probably exists more than one binding site (*57*).

Chemical shift changes $\Delta\delta$ were referenced to the peak position in the HSQC spectrum of ligand-free (no CD4mut) VpUcyt. The largest chemical shift changes of VpUcyt backbone amide cross-peaks were observed at 1 mM CD4mut and apply to A66 ($\Delta\delta^{1}$HN = 0.032 ppm) and E69 ($\Delta\delta^{15}$N = 0.223 ppm), in the ^{1}H and ^{15}N dimension, respectively. The maximum composite CSP amounts to 0.051 ppm and was also observed for E69. Composite CSP values for all non-overlapping cross-peaks of VpUcyt in presence of 1 mM CD4mut were normalized with respect to the CSP of E69 and are displayed as a function of VpUcyt sequence position in Figure 21 (cf. 3.2.2).

The pattern of CSPs can now be analyzed with respect to the secondary structure of VpUcyt, as published by Wittlich et al. (*21*). The panels in figure 32 indicate the position of the three secondary structure elements of VpUcyt, observed earlier in the presence of CD4-free DPC micelles (*21*): an N-terminal amphipathic helix (residues 39 to 48, named helix 2) and a flexible helix (residues 64 to 70, named helix 3) are indicated by grey stripes, and a hydrophobic tight loop close to the C-terminus

(residues 73 to 78) is marked by an open rectangle. These structural elements can be used as references to discuss and interpret the results.

Residues located in, or just C-terminal of helix 3 of VpUcyt in CD4-free DPC micelles show the strongest shift changes (residues 64 to 74); a smaller cluster of less pronounced shifts is found at the C-terminus of helix 2 (T47, E48, A50). In contrast, most residues in the interhelical linker, in helix 2 and in the C-terminal tight loop show only marginal CSP effects. Most likely, VpUcyt residues in the region of helix 3 are part of the CD4 binding site. Perhaps, this region might undergo a structural rearrangement in the course of CD4 binding, e.g., an extension, stabilization or destabilization of helix 3. The CSPs relative to the secondary structure elements observed in VpUcyt in the absence of CD4mut are shown in figure 32.

However, one cannot exclude the possibility, that the observed CSPs present an allosteric effect. The same arguments hold true for the C-terminus of helix 2. The significant CSPs observed may reflect a CD4 binding site, structural rearrangements in this region upon CD4 binding or an allosteric effect.

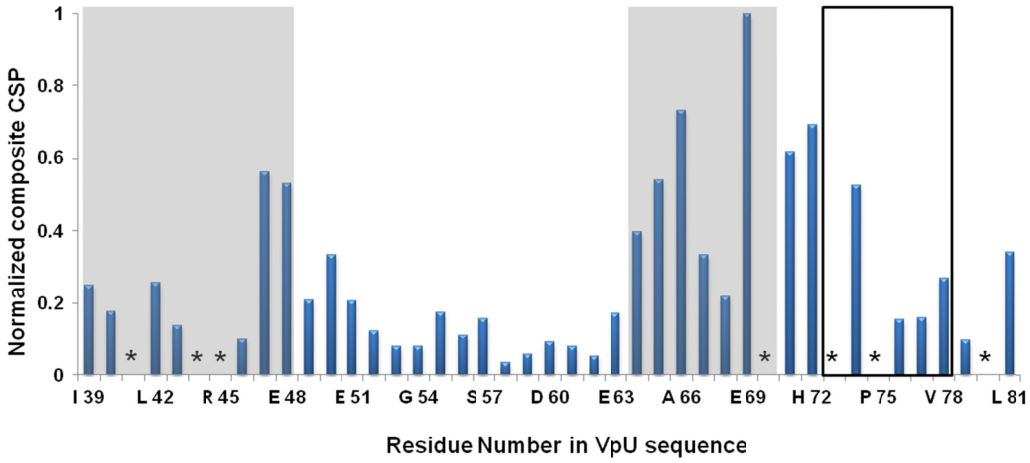

Figure 32: Plot of chemical shift perturbation with respect to the secondary structure of VpUcyt. The positions of two helices and a C-terminal tight loop reported for VpUcyt in presence of DPC but without CD4 (*21*) are indicated by grey stripes and an open rectangle, respectively. Stars indicate unavailable experimental data due to peak overlap or proline. The sample contained 450 µM ^{15}N VpUcyt and 100 mM DPC. Data were normalized to the maximum CSP, which was observed for E69.

It is also possible to map the CSP effects on the three dimensional structure of VpUcyt. VpUcyt residues showing the strongest CSP effects (above a threshold of 0.3) in presence of 1 mM CD4mut are highlighted in red in the ribbon diagram of CD4-free VpUcyt (Figure 33), determined in presence of 100 mM DPC (*21*).

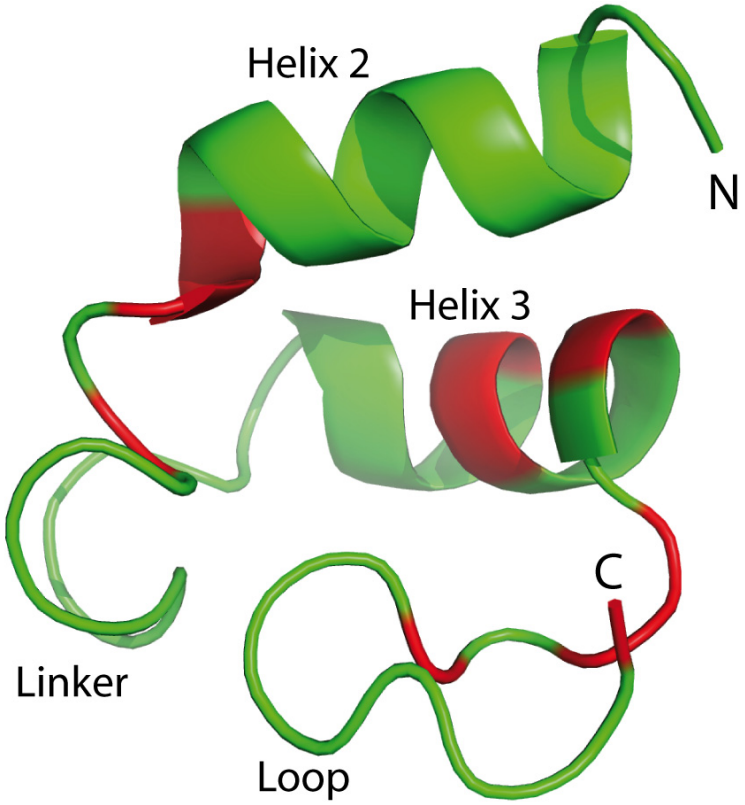

Figure 33: Solution NMR structure of VpUcyt in presence of membrane mimicking DPC micelles (PDB code: 2K7Y). Previously determined structure elements have been labelled (*21*). VpUcyt residues showing maximum chemical shift changes upon addition of CD4mut (1mM) to the sample are highlighted in red (criterion: normalized CSP is larger than 0.3).

4.1.3 Affinity of binding

Nuclear spins of VpUcyt that have significantly different chemical shifts in the CD4mut-bound and in the ligand-free state encode information on the fraction x_b of CD4mut-bound VpUcyt in the sample. In case of rapid exchange, one single peak is observed for every directly bonded ^{1}H-^{15}N spin pair of VpUcyt in an HSQC spectrum, and it is the chemical shifts of qualifying peaks that contain the desired information on x_b. Therefore, an experimental binding isotherm is obtained directly if the chemical shift of a suitable VpUcyt spin is measured for a series of CD4mut concentrations (*111*). Provided that x_b varies from close to 0 (free VpUcyt) to almost 1 (all VpUcyt molecules are bound) during the titration, one can fit the data to a proper binding model of the interaction and obtain the dissociation constant K_d of the complex. Assuming a 1:1 complex of VpUcyt and CD4mut, a sigmoidal shape of the binding isotherm is expected. Thirteen titration steps were carried out, increasing the CD4mut concentration from 0 to 1 mM, while the VpUcyt concentration was kept constant (450 µM). Figure 22 (cf. 3.2.3) shows the composite CSP values measured for E69 of VpUcyt as a function of CD4mut concentration on a logarithmic scale. The available data may reflect the rising part of a sigmoidal binding isotherm. However, there is no indication of a bound state plateau at the highest CD4mut concentration studied (1 mM). This suggests a rather weak affinity of the CD4mut-VpUcyt complex, with a K_d above 1 mM. Several factors might contribute to this unexpectedly low *in vitro* affinity. VpU residues 1 to 38, which are missing in our VpUcyt protein, may be important for binding (*29, 116, 117*). Anchoring both the CD4 and VpU cytoplasmic domains in the same membrane would reduce the dimensionality of protein diffusion, which in turn might enhance their affinity. Protein-lipid interactions may play a role. Additionally, it is possible that the interaction requires a yet unknown cellular cofactor.

4.1.4 Paramagnetic relaxation enhancement (PRE) analysis

The CSP experiments provided initial insights into the CD4-VpUcyt interaction, and helped identify the VpUcyt residues most affected by CD4 binding. Subsequently, the aim was to study the VpU-CD4 binding using a complementary method. Paramagnetic probes are routinely used in NMR to provide long range intra- or intermolecular distance information of up to 20 Å (*59, 118*). They cause distance-dependent line broadening and intensity loss of NMR signals, particularly in protons. The spin label MTSL was attached to strategic positions on the CD4 molecule via disulfide bond formation with single cysteines in three CD4mut variants. Two of these

positions lie in regions that have been implicated in VpU binding (*27, 119-122*). The third label (CD4R-3C) is meant to serve as a negative control. These paramagnetically active CD4mut variants are then added to solutions of ^{15}N-labelled VpUcyt. The VpUcyt residues in proximity (up to 20 Å) to the MTSL label, and thus the CD4 molecule, will experience line broadening or losses in signal intensity. The experimental strategy for the PRE measurements is depicted in figure 34.

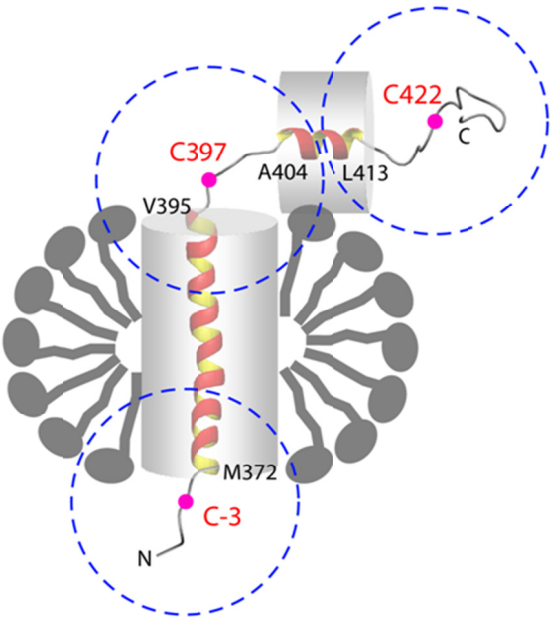

Figure 34: Strategy for monitoring the interaction between CD4mut and VpUcyt in DPC micelles by PRE experiments. Oxidized paramagnetic probes were covalently linked to single cysteine residues in three CD4mut variants. The PRE effect decreases with the distance from the active probe (magenta dots) and has a range of ~20 Å (blue circles). Line broadening and loss of peak intensity are expected for the VpUcyt nuclear spins that at least transiently occupy the corresponding spheres.^{15}N-labelled VpUcyt and CD4mut were combined in a DPC micelle solution. Subsequently, VpUcyt NMR spectra were screened for indications of signal loss or broadening.

MTSL is paramagnetic in the oxidized state, but becomes diamagnetic in the presence of excess amounts of the reducing agent ascorbic acid. The unpaired electron of the oxidized nitroxide radical in MTSL has a much greater magnetic moment than the surrounding protons, and is thus a source of dramatic relaxation enhancement for neighbouring spins. We compared signal intensities of backbone amide cross-peaks in $^{1}H,^{15}N$ HSQC experiments of ^{15}N-labelled VpUcyt in presence of MTSL-labelled CD4mut variants in the oxidized vs. reduced state of the spin label. The ratio of VpUcyt signal intensities recorded under oxidizing and reducing conditions is referred to as signal retention in presence of the paramagnetic label. The comparison of signal intensities in the presence of oxidized and reduced MTSL was plotted as a function of VpUcyt sequence position for three different MTSL-labelled CD4mut variants (Fig 24).

Like with the CSP data, the pattern of peak intensity reduction can now be analyzed with respect to the secondary structure of VpUcyt in the presence of DPC micelles, as published by Wittlich et.al (*21*).

The overall pattern of VpUcyt signal retention is similar for all three MTSL attachment sites studied, i.e., amino acids C422 (Fig 35, A), C397 (Fig 35, B), and C-3 (Fig 35, C) in the three CD4mut variants. Signal retention is highest in the region connecting the two helices, is intermediate in the region of the two helices and at the extreme C-terminus, and is lowest in the region of the tight loop. The magnitude of PRE-based intensity reduction is quite different in the three panels of Figure 35, and depends on the MTSL position. Relaxation enhancement of VpUcyt spins by CD4mut-attached paramagnetic MTSL is least efficient for CD4mut(R-3-MTSL), slightly more efficient for CD4mut(C422-MTSL), and most effective for CD4mut(C397-MTSL). In the latter case, some VpUcyt cross-peaks (E48, L67, E69, A74, W76, D77) are completely absent in presence of the active paramagnetic probe.

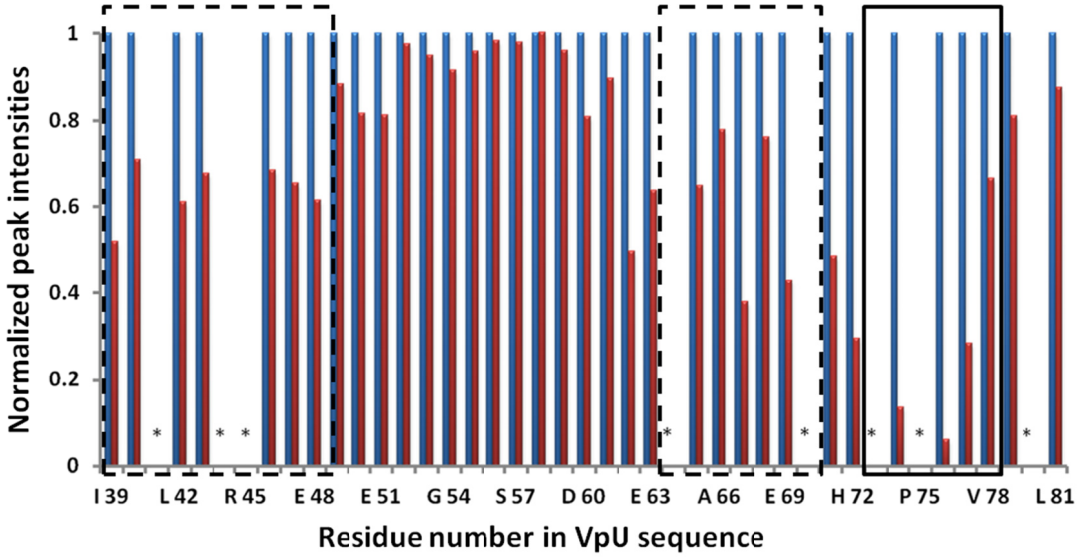
A
Normalized peak intensities
1
0.8
0.6
0.4
0.2
0
I 39 L 42 R 45 E 48 E 51 G 54 S 57 D 60 E 63 A 66 E 69 H 72 P 75 V 78 L 81
Residue number in VpU sequence

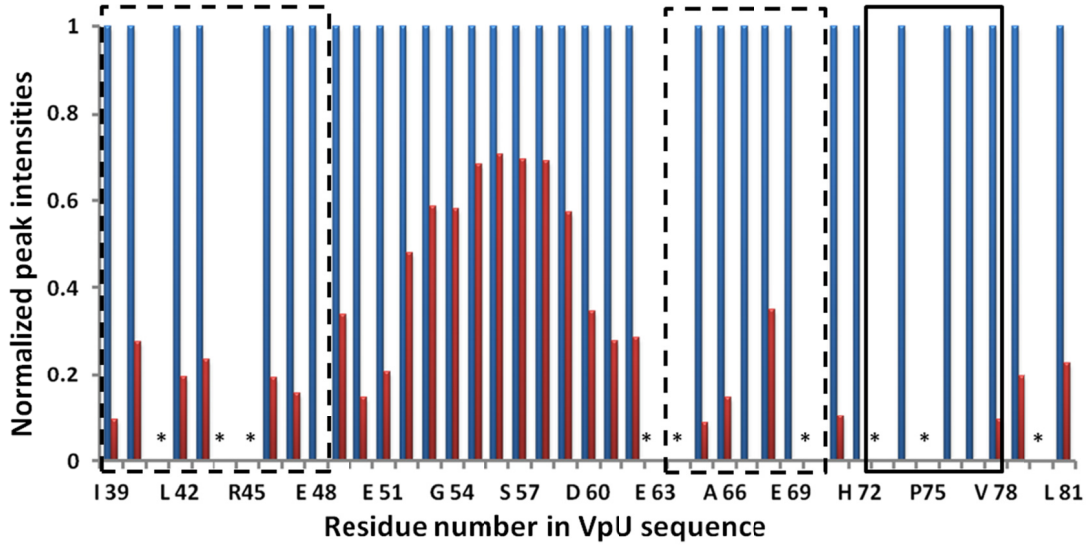
B
Normalized peak intensities
1
0.8
0.6
0.4
0.2
0
I 39 L 42 R45 E 48 E 51 G 54 S 57 D 60 E 63 A 66 E 69 H 72 P75 V 78 L 81
Residue number in VpU sequence

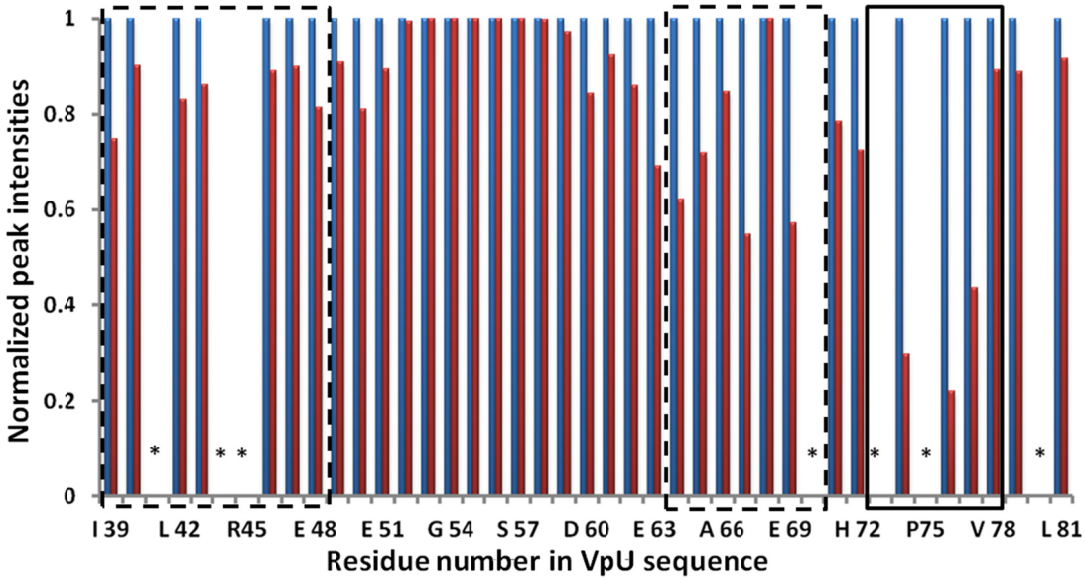
C
Normalized peak intensities
1
0.8
0.6
0.4
0.2
0
I 39 L 42 R45 E 48 E 51 G 54 S 57 D 60 E 63 A 66 E 69 H 72 P75 V 78 L 81
Residue number in VpU sequence

Figure 35: Comparison of normalized intensities for VpUcyt cross-peaks in the presence of reduced (Blue) and oxidized (Red) PRE labelled CD4mut, as a function of residue number (Fig 24, cf. 3.2.4). The positions of two helices and a C-terminal tight loop reported for VpUcyt in presence of DPC but without CD4 (*21*) are indicated by dotted lines and a solid line, respectively. The active PRE probe was covalently linked to C422 **(A)**, C397 **(B)**, and C-3 **(C)** in single cysteine variants of CD4mut. Stars denote peak intensities that could not be quantified. All samples contained 450 µM VpUcyt, 600 µM CD4mut, and 100 mM DPC. Intensity reduction shows a similar pattern in all three data sets: Amino acids in the interhelical region are least affected, the two helical regions show intermediate signal reduction and the effect is strongest for the C-terminal tight loop. But the extent of signal reduction strongly depends on the position of the PRE probe in the CD4 sequence.

4.1.5 Dynamic equilibrium of VpUcyt conformations and binding to CD4mut

VpUcyt is unstructured in plain aqueous buffer but adopts a more defined 3D structure upon addition of DPC micelles (*21*). The well-defined helix 2 (residues 39 to 48) is rather rigid and is present in ~80% of the VpUcyt conformers in DPC solution (*21*). Helix 3 (residues 64 to 70) is simultaneously found in ~40% of conformers only. The amino acids between the N-terminus of helix 3 and the C-terminus of the tight loop (residues 64-78) show substantial dynamics and have higher mobility than helix 2. The interhelical linker (residues 49 to 63) and the very C-terminus of VpUcyt are very flexible and do not show any indication of secondary structure in DPC micelle solution (*21*). Observation of a single set of VpUcyt NMR signals in presence of DPC micelles indicates fast interconversion of the individual conformations found in the ensemble. The data on helix 2 suggest that at least 80% of the VpUcyt molecules in the sample are associated with the DPC micelle at any instant of time. The fraction of unbound VpUcyt, if any, must be lower than 20%.

Incorporation of CD4mut into the DPC micelle gives rise to three rapidly exchanging states of VpUcyt: (i) unbound VpUcyt in buffer; (ii) VpUcyt associated primarily with the DPC component of the micelle; and (iii) VpUcyt bound to CD4mut. It is reasonable to assume that the equilibrium between groups (i) and (ii) is only marginally affected by the introduction of CD4mut. However, the overall number of VpUcyt molecules in states (i) and (ii) will be diminished by the CD4mut-bound VpUcyt. The chemical shift changes of VpUcyt observed upon incorporation of

CD4mut into the micelle (Fig 21, cf. 3.2.2) reflect the redistribution of VpUcyt from states (i) and (ii) on one hand side to state (iii). The inflection point of a sigmoidal protein-ligand binding isotherm denotes the ligand concentration at which exactly 50% of proteins are ligand-bound. The absence of an inflection point in the measured part of the binding isotherm in Figure 22 (cf. 3.2.3) indicates that even at the highest CD4mut concentration studied (1 mM) less than 50% of the VpUcyt molecules are bound to CD4mut. Consequently, at least 40% of all VpUcyt molecules in the sample belong to group (ii). This reasoning is important for interpretation of the PRE data.

The overall pattern of VpUcyt intensity retention observed in samples with MTSL-labelled CD4mut variants (Figure 24, cf. 3.2.4) is very similar to the pattern obtained earlier for VpUcyt in presence of DPC micelles doped with 16-doxylstearic acid, where the paramagnetic probe is confined to the hydrophobic interior of the micelle but may get close to the polar headgroups of DPC (*21*). CD4mut residues S397 and R-3, which are replaced by MTSL-linked cysteine in the PRE experiments, are only 2 or 3 residues away from the C- or N-terminal ends, respectively, of the micelle embedded transmembrane helix of CD4mut (Figure 34) (*123*). The common proximity of the three paramagnetic probes CD4S397C-MTSL, CD4R-3C-MTSL and 16-doxylstearic acid to the headgroup region of the micelle will cause a similar intensity retention pattern for the large VpUcyt fraction (at least 40%) that is DPC-associated. Transient specific binding of VpUcyt to MTSL-labelled CD4mut will further decrease the observed VpUcyt signal intensity.

The situation is somewhat different in case of CD4S422C-MTSL, where the paramagnetic label is attached to the dynamic C-terminal tail of CD4 which is not necessarily located in the DPC headgroup region, but may explore a larger space on and above the surface (*123*). Perhaps a larger fraction of VpUcyt signal reduction is attributable to specific binding of VpUcyt to CD4mut in case of CD4S422C-MTSL, when compared with the other two MTSL positions.

The reduced VpUcyt signal intensity retention observed for CD4S397C-MTSL and CD4S422C-MTSL in comparison with CD4R-3C-MTSL in Figure 35 proves specific binding of VpUcyt to CD4mut on top of unspecific VpUcyt association with the DPC micelle.

Intensity retention is lower in case of CD4S397C-MTSL than for CD4S422C-MTSL. This suggests that CD4 residue 397 is in closer proximity to bound VpUcyt than residue 422.

One may be tempted to derive CD4 binding amino acid residues of VpUcyt from the signal retention profiles in Figure 35. Such an approach is justified for stable protein-

protein or protein-ligand complexes (*124, 125*), but not for the highly dynamic complex of VpUcyt and CD4mut studied here, in particular if a significant fraction of the unbound interaction partner is kept in close proximity to the PRE source by unspecific interactions with the micelle. The strongest relaxation enhancement for all three MTSL label positions is observed for residues in the tight loop (Figure 35). However, almost no CSP effect is observed for this region (Figure 32), which discounts the tight loop as a potential CD4 binding site. Instead, the strong susceptibility of this loop region to paramagnetic relaxation enhancement might be the result of rapid positional exchange of the loop region. Notably, similarly strong PRE effects on this region of VpUcyt were observed earlier, both in presence of micelle-embedded 16-doxylstearic acid as well as after adding paramagnetic Mn^{2+} ions to the aqueous buffer (*21*).

4.1.6 Biological context

Earlier studies implicated the cytoplasmic domains of both CD4 and VpU in degradation of CD4 in the ER, as well as physical binding between VpU and CD4 (*25, 26, 28, 126, 127*). Coimmunoprecipitation of VpU with CD4 variants carrying cytoplasmic domains with different levels of C-terminal truncations revealed the presence of a VpU binding site within the amino acid sequence 402 to 420 of CD4 (*127*). The same CD4 region is critical for VpU-induced degradation of CD4 in the ER (*126*). The CD4 amino acid sequence 414 to 419 appears to be the minimal element required for efficient VpU-dependent degradation of CD4 (*26*). In addition, formation of a membrane proximal helix in the CD4 cytoplasmic region seems to be critical for VpU binding (*28*).

Our PRE data confirm binding of VpUcyt to the cytosolic part of CD4mut in DPC micelles. The VpU binding site is within ~20 Å of both residues 397 and 422 of CD4. The stronger VpU signal reduction upon binding to CD4S397C-MTSL compared to CD4S422C-MTSL indicates that binding to VpU does not just involve the region 414-419 (LSEKKT), but a larger membrane proximal part of the CD4 cytosolic domain. It may also be related to a role of the cytoplasmic helix of CD4 in VpU binding. This helix encompasses CD4mut residues 404-413 in VpU-free DPC micelles which is slightly closer to residue 397 than to 422 in the CD4 sequence. The position of residue 397 is also close to the transmembrane domain of CD4 (residues 372-395). Our results are certainly compatible with additional binding determinants in the transmembrane domain of CD4.

Both the membrane proximal helix in the cytoplasmic domain and the C-terminus of VpU (residues 76-81) are required for CD4 binding and degradation (*128*). Mutational analysis further suggested the importance of preserving an amphipathic helix in the membrane proximal region of VpU (helix 2 in our nomenclature) rather than the specific amino acid sequence of VpU for binding to CD4 (*116*).

Our CSP data (Figure 32) confirm involvement of VpU helix 2 in CD4 binding. However, only small chemical shift changes occur at the VpU C-terminus. Interestingly, several residues in and around helix 3 of VpUcyt experience the strongest chemical shift changes upon CD4 binding, implicating a prominent role of this helix. Both cytosolic helices of VpUcyt are affected by CD4 binding; whether they form direct contacts with CD4 or rather undergo structural rearrangements upon CD4 binding remains an open question.

The interhelical region region of VpUcyt contains the S53 and S57 residues, both of which are phosphorylated by caesin kinase II (*129-131*). They also form part of the $DS_PG\ \Phi\ XS_P$ motif (S_P-phosphorylated serine, Φ and X correspond to hydrophobic and variable amino acid residues, respectively). Phosphorylated VpU interacts with βTrCP1 and βTrCP2 via this motif, which is a critical step in the CD4 degradation pathway (*49, 132, 133*). The CSP results suggest that CD4 does not interact with this motif, as there are no significant chemical shift changes in this region. This would permit the formation of a CD4-VpU-βTrCP ternary complex, as has already been suggested (*134*). Figure 36 depicts such a model for VpU-mediated CD4 degradation.

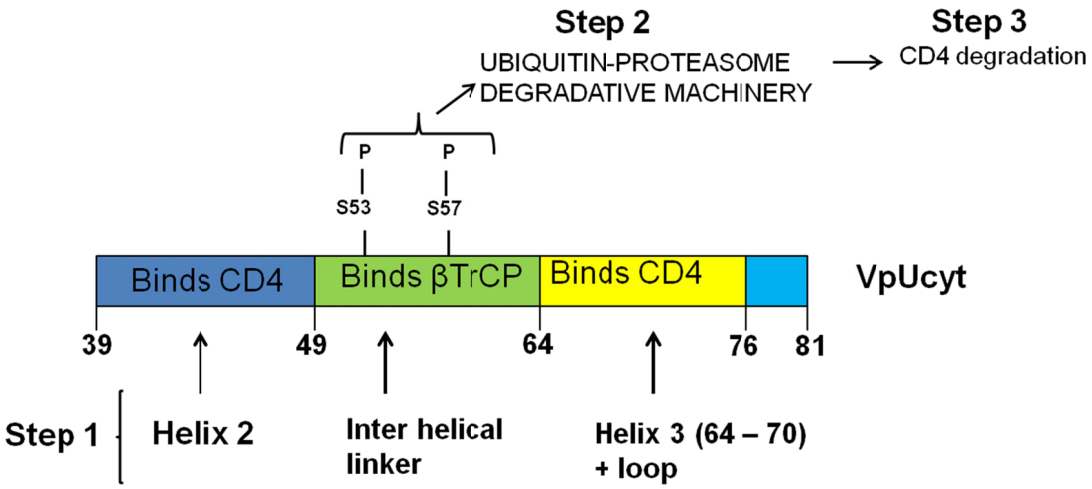

Figure 36: Possible model for VpU-mediated CD4 degradation. The CSP and PRE data are consistent with a model, whereby an initial CD4-VpU-βTrCP ternary complex may assemble **(Step 1)**. This could be followed by recruitment of the degradative machinery **(Step 2)**, and finally, CD4 degradation **(Step 3)**.

NMR-based CSP analysis allows verification and topological characterization of protein interactions and does, in general, not require mutations or truncations of the target proteins. A combination PRE and CSP analysis shows that helices 2 and 3 of VpU, and very likely also the cytosolic helix of CD4 play a role in the formation of a bound complex of CD4 and VpU. The flexible interhelical linker region of VpU (R49-E63), comprising the βTrCP binding motif including the two phosphorylation sites, remains largely unaffected by CD4 binding to VpU.

4.2 Microscale Thermophoresis (MST)

4.2.1 Rationale for employing nanodiscs in microscale thermophoresis (MST)

Membrane proteins account for ~30% of proteins encoded by the human genome (*135-137*). They perform a wide variety of functions, like nutrient transport, cell adhesion, cell signalling and energy transduction, to name a few. They also play important roles in the initiation and progression of diseases. For example, human CD4 acts as the primary receptor for HIV-1 entry into host cells. The development of methods for the correct characterization of membrane proteins and their interactions, is thus a central theme in biophysics. Model membrane systems and mimetics like detergents, bicelles and liposomes are extensively used in membrane protein studies. As mentioned earlier, the relatively new nanodisc technology seems to provide a stable and near native alternative for membrane protein solubilization.

Microscale thermophoresis (MST) can characterize interactions using very small sample amounts, in a relatively short time period. The successful combination of nanodiscs and MST could potentially pave the way for rapid analysis of multiple membrane protein interactions, in a biologically relevant environment.

4.2.2 Protocol

Interaction studies using the NT.115 instrument (NanoTemper Technologies) require fluorescent labelling of one of the interacting partners. Accordingly, nanodiscs were assembled with small amounts of dye-labelled lipids (cf. 2.2.4). Nanodiscs with POPC and DMPC as the principal lipids, were supplemented with Atto 647N DMPE and Atto 488 DMPE, respectively. The resulting nanodiscs were termed POPC-Atto 647N and DMPC-Atto 488. The molar ratio of the labelled and unlabelled lipids in the assembly mixture was such that each nanodisc was calculated to carry two fluorescent lipids.

The MST analysis proceeds by first loading samples into specific capillaries. Depending on the chemical modification of the glass surface, capillaries are classified as standard, hydrophilic, hydrophobic, enhanced gradient and BSA-coated. Capillaries are supplied by NanoTemper Technologies, Munich. Analyzing a binding interaction requires a titration series, with the concentration of the fluorescently

labelled compound kept constant at each titration step, while that of the unlabelled binding partner is systematically increased. A standard titration series consists of up to 16 capillaries, which are measured in a single thermophoresis run.

Capillary scans were run before measuring thermophoresis. The capillary scan is an indicator of the amount of fluorescence in each capillary. Fluorescence levels should be constant within error limits for all capillaries in a series. Large deviations in the fluorescent intensities indicate adverse effects between the sample and sample containers (sample tube, capillary walls, etc). The strength of the detected fluorescence can be varied by changing the LED power (10 – 100%).

Additionally, the shape of the fluorescence peak is indicative of whether the fluorescently labelled sample adsorbs to the capillary walls. Samples that adsorb to the capillary walls show a U-shaped pattern in the capillary scan, while those that do not show the inverted V-shape (cf. 3.4.1). A molecule that adsorbs to the capillary walls will most likely not participate in the interaction with its binding partner. Furthermore, sample adsorption reduces the concentration of soluble molecules in an unpredictable manner, thus rendering any measured affinity parameters erroneous.

As previously shown, nanodiscs adsorb to the walls of the capillaries (cf. 3.4.1). Nanodisc adsorption is seen for all types of capillaries, although to a varying degree.

Adsorption may be a result of the fact that nanodiscs are large complex ensembles of lipids and amphipathic proteins. They thus contain different surface patches (hydrophilic, hydrophobic regions), which may enhance adsorption to the capillary walls. Another factor contributing to adsorption, is that nanodiscs may tend to aggregate in the capillary enviromment. Nanodisc samples which adsorb to capillary walls also tend to show extreme bumpiness in their raw data (cf. 3.4.1.1). Such extreme bumpiness is usually an indicator of particle size inhomogeneity (aggregation), suggesting that nanodiscs may aggregate even at the low nanomolar concentrations used in MST experiments.

4.2.2.1 Strategies to prevent nanodisc adsorption

Addition of low concentrations of detergent molecules has been shown to prevent adsorption of soluble globular proteins to the capillary walls (*65*). Additionally, traditional blocking agents like BSA have been shown to have similar effects (*65*). Nanodisc samples were tested in the presence of low concentrations of a variety of these additives (Table 12, cf. 2.2.5.4).

The addition of 0.005% SDS to POPC-Atto 647N nanodiscs prevents sample adsorption to the capillary walls. Also, the effect of SDS seems to be very long lasting. In fact adsorption to the capillary walls was not detected even after a sample was stored in the instrument for three weeks. Nanodisc samples with SDS also show smooth, reproducible raw data (cf. 3.4.1.2.1). Other detergents like Tween 20 and CTAB also prevented sample adsorption, although the effect was not as long lasting as seen with SDS. This may be attributed to the negative charge carried by SDS. SDS molecules could perhaps insert into individual nanodiscs, causing nanodisc repulsion, and consequently preventing their fusion and aggregation.

A similar effect was seen for DMPC-Atto 488 nanodiscs in the presence of 0.005% BSA. In this instance, samples did not show capillary adsorption for at least 2 days.

While detergents do improve sample quality, they may adversely affect the experiment, as their effect on nanodisc structure and stability is unknown. Even at 0.005%, the detergent concentration is well over the standard nanodisc concentration used, and may well modify the nanodisc structure. For instance, 0.005% of SDS corresponds to a molar concentration of 173 µM, while the nanodisc concentration typically used in the mentioned experiments is between 5 and 100 nM. Additionally, detergents could bind one of the interaction components, thus interfering with the desired interaction.

To eliminate the use of detergents and prevent sample sticking, we employed a procedure akin to liposome preparation via extrusion. It involves spinning down the nanodisc solution (13000 x g, 5 min, room temperature) and then passing it once through a 50 nm Nuclepore membrane. Initially, filtered nanodiscs do not adsorb to the capillary walls. However, adsorption is seen after 3 to 4 hours. Thus, for best results, nanodiscs must be used immediately after filtration.

4.2.2.2 Laser power

Laser power denotes heating power, and thus has an immediate influence on the strength of thermophoresis. Its value can be varied between 10% to 100% (i.e. voltages from 0.5 V to 2 V). It is recommended to check different laser powers (20%, 40%, 80%) while studying new interactions, and most systems can be measured at lower laser powers (20%, 40%).

Is must be noted that using a laser power of 100% can cause a rapid temperature increment (in <1 second) of up to 10 °C at the laser focus; an increase that may even adversely affect the sample. On the other hand, lower laser powers cause less sample heating, thus helping preserve the sample for a longer time period. This is especially important while studying proteins, as a rapid temperature jump (as seen with 100% laser power) could easily accelerate effects like protein precipitation or aggregation. However, when POPC-Atto 647N nanodiscs were measured at 20% laser power, the resultant raw data was irreproducible and noisy (cf. 3.4.1.3). Additionally, the thermophoretic depletion of the sample was negligible; after the laser was switched on, the normalized fluorescence only reduced from 1.0 to 0.97. However, on increasing the laser power to 100%, the raw data was smoother, reproducible, and with a higher thermophoretic depletion (cf. 3.4.1.3). Experiments involving POPC-Atto 647N nanodiscs were thus always recorded at 100% laser power.

In contrast, DMPC-Atto 488 nanodiscs produced satisfactory curves at lower and higher laser powers (20%, 40%, 80%) (cf. 3.4.1.3). Raw data were smooth, reproducible and showed higher thermophoretic depletion. For instance, even at 20% laser power, the normalized fluorescence reduced from 1.0 to 0.90, thus showing much higher thermophoretic depletion as compared to POPC-Atto 647N nanodiscs at the same laser power.

The difference in behaviour of the two nanodisc types is either due to the principle lipid (POPC, DMPC), or the type of dye used (Atto 647N, Atto 488).

Majority of the optimization experiments presented here were conducted on POPC-Atto 647N nanodiscs. The advantage of using POPC is that its main phase transition temperature of 5 °C is far away from the temperature utilized in the experiments (25 °C). Additionally POPC is biologically more relevant, as it is found in eukaryotic cell membranes (*138, 139*). On the other hand, nanodiscs made from DMPC (saturated chain lipid) seem to be much more suited for MST experiments. Additionally, recent reports have suggested that the Atto 647N dye used in POPC-Atto 647N nanodiscs may not be ideal for MST experiments, since it exhibits inconsistent thermophoretic behaviour (internal communication, Dr. Jerabek-Willemsen, Nanotemper Technologies, Munich). Future interaction studied should thus be conducted using DMPC-Atto 488 nanodiscs.

4.2.3 Interaction studies

4.2.3.1 Nef binding to CD4mut

The HIV-1 accessory protein Nef interacts with CD4 molecules at the cell surface, thus facilitating their endocytosis and eventual degradation in lysosomes (*49*). The interaction involves the cytoplasmic domain of CD4 (*53*). For these studies, purified HisUbiquitinCD4mut was incorporated into POPC-Atto 647N nanodiscs (cf. 3.1.1, cf. 3.3). The binding between the HisUbiquitinCD4mut-loaded nanodiscs and Nef was then studied using MST. The interaction between Nef and unloaded nanodiscs served as the negative control (cf. 3.4.2.1). A K_d of ~0.3 µM was obtained for Nef binding to the loaded nanodiscs, assuming that one Nef molecule binds one loaded nanodisc. However, analysis of MST data for Nef binding to empty nanodiscs gave the same K_d. This implies that Nef interacts strongly with POPC lipids, and that the result obtained with CD4-loaded nanodiscs most probably reflects Nef-POPC, and not Nef-CD4 binding.

The ability of Nef to interact with liposomes has been recently reported (*140*). However, these studies state that the interaction requires the presence of negatively charged lipids, with strongest binding reported for Nef binding to liposomes with 30% negatively charged lipids. Contrarily, a previous study reported the ability of Nef to disrupt POPC liposomes, which did not carry any negative charge (*141*). The latter study may support our results regarding Nef-POPC binding.

Perhaps the MST data represent two processes. Firstly, the binding of Nef to POPC lipids, that takes place at a K_d of ~0.3 µM. Secondly, the binding of Nef to CD4mut, that perhaps takes place at a much lower K_d. Previous studies on Nef-CD4 binding mostly employed shorter, soluble CD4 peptides, which included only the proposed Nef binding sites (*142*). Here, we have studied binding of the full length Nef protein, with the transmembrane and cytoplasmic domains of CD4, in a membrane environment that closely mimics its natural one. This may lead to much stronger Nef-CD4 binding. Perhaps, MST is not sensitive enough to clearly detect such high affinity binding. This possible scenario has been further explained in figure 37.

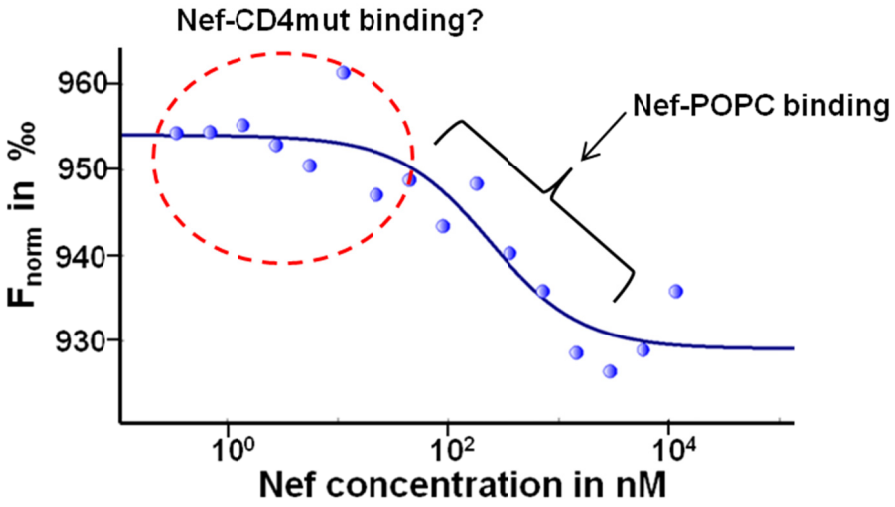

Figure 37: MST-based binding isotherm recorded with 50 nM POPC-Atto 647N nanodiscs loaded with HisUbiquitinCD4mut and varying amounts of Nef. MST data may represent two binding processes. The measured K_d of ~0.3 µM probably represents Nef-POPC binding, as indicated by the right brace. The binding of Nef to CD4 may occur at a lower K_d, in the region indicated by the red dashed oval, but is not visible in the recorded data. The instrument is perhaps not sensitive enough to detect the latter process.

4.2.3.2 Binding of the p6 peptide to Vpr

In HIV-1, Vpr is a 14 kDa protein that plays an important role in regulating nuclear import of the HIV-1 pre-integration complex. It is also essential for the infection of terminally differentiated macrophages by HIV-1 (*143*).

Unlike other accessory proteins, Vpr is packaged into virions in quantities similar to the viral Gag proteins. P6 is a small 52 amino acid protein that encompasses the C-terminal region of the group specific antigen (Gag). It is essentially obtained after the proteolytic processing of the Gag polyprotein (*144*). The interaction of Vpr and p6 is essential, as it facilitates incorporation of Vpr into assembling virions. While this interaction has been well characterized in HIV-1, its presence in HIV-2 is yet to be confirmed.

In this work, the binding between the HIV-2 Vpr in DMPC-Atto 488 nanodiscs, and a section of the soluble p6 protein, (comprising amino acids 18-77), was studied using MST. The binding of p6 to unloaded nanodiscs served as the negative control (cf. 3.4.2.2). The binding of p6 to Vpr-loaded nanodiscs yields a K_d of 32 µM.

Furthermore, the interaction can be clearly distinguished from p6 binding to unloaded nanodiscs. This rules out the possibility that the result represents p6 binding to lipids (cf. 3.4.2.2). The K_d of 32 µM is in agreement with values published for the Vpr binding to p6 in HIV-1 (*145*).

These results represent the first evidence that MST can be used to study binding between a nanodisc-inserted membrane protein and its soluble protein ligand.

5 Summary

The accessory proteins from HIV-1 are now known to play vital roles in the replication efficiency and infectivity of the virus. Of these proteins, the virus protein U (VpU) and negative factor (Nef) are responsible for downregulation of human CD4. VpU is expressed late during the virus life cycle, and acts on newly synthesized CD4 molecules in the ER. Physical binding of VpU to CD4 triggers a pathway that leads to the degradation of CD4 via the ubiquitin-proteasomal system. Previous studies implicated certain regions in the cytoplasmic parts of both proteins in binding. In the present work nuclear magnetic resonance (NMR) spectroscopy was used to study the CD4-VpU interaction in detail. Sections of VpU and CD4 containing regions crucial for CD4-VpU binding were recombinantly produced in Escherichia coli in milligram amounts and purified to homogeneity. The interaction was probed using two complementary NMR techniques, namely chemical shift perturbation (CSP), and paramagnetic relaxation enhancement (PRE) analyses. For the PRE experiments three different single cysteine CD4 variants were produced and specifically labelled with a paramagnetic probe, MTSL. The CSP data confirm involvement of helices 2 and 3 of VpU in CD4 binding. The PRE data indicate that binding to VpU doesn't just involve the region 414-419 (LSEKKT) of CD4 as previously reported, but a larger membrane proximal part of the CD4 cytosolic domain as well. All in all, the CSP and PRE results corroborated each other. The dissociation constant (K_d) for the interaction of the studied VpU and CD4 fragments is found to be in the millimolar range.

The second part of this work concerns the development and application of a protocol for characterization of membrane protein interactions using nanodiscs and microscale thermophoresis (MST). Nanodiscs are a superior model membrane, with reported applications in various areas of biophysics. Microscale thermophoresis is a relatively new method that characterizes intermolecular interactions based on the differential movement of proteins and their complexes in a thermal gradient. MST requires very little protein, is highly sensitive, and studies interactions in solution. Protocols for MST studies were developed for two different types of nanodiscs, containing either POPC or DMPC as the principal lipid. The persistent problem of adsorption of nanodiscs to the capillary walls used in MST was circumvented by either supplementing the nanodisc solutions with certain additives (detergents, BSA) or by filtering them through nuclepore membranes. The protocol was applied to the study of interactions between Nef and CD4 and between the HIV proteins Vpr and p6 with one interaction partner anchored in a nanodisc.

Zusammenfassung

Die akzessorischen Proteine von HIV-1 spielen eine wichtige Rolle für die Replikationseffizienz und Infektiosität des Virus. Zwei dieser Proteine, das Virusprotein U (VpU) und das Protein „negative factor“ (Nef), bewirken die Herunterregulierung des humanen CD4. VpU wird in der späten Phase des viralen Lebenszyklus gebildet und wirkt auf neu synthetisierte CD4-Moleküle im endoplasmatischen Retikulum. Die physische Bindung des VpU an CD4 stellt den ersten Schritt einer Ereigniskette dar, welche zum Abbau des CD4 über das Ubiquitin-Proteasom-System führt. Bisherige Studien haben gezeigt, dass bestimmte Bereiche in den zytoplasmatischen Regionen beider Proteine an der Bindung beteiligt sind. In der vorliegenden Arbeit wurde die kernmagnetische Resonanzspektroskopie (NMR) verwendet, um die CD4-VpU Wechselwirkung im Detail zu untersuchen. Teile von VpU und CD4, welche die für die CD4-VpU Bindung entscheidenden Regionen enthalten, wurden rekombinant im Milligramm-Maßstab in *Escherichia coli* hergestellt und lagen nach der Reinigung als homogene Produkte vor. Die Protein-Protein Wechselwirkung wurde mittels zweier komplementärer NMR Techniken untersucht, der Beeinflussung der chemischen Verschiebung infolge der Bindung („chemical shift perturbation“, CSP) und der Relaxationsverstärkung durch paramagnetische Sonden („paramagnetic relaxation enhancement“, PRE). Für die PRE-Experimente wurden drei Einzelcysteinvarianten des CD4 hergestellt und spezifisch mit der paramagnetischen Sonde MTSL markiert. Die CSP-Daten bestätigen die Beteiligung der beiden Helices 2 und 3 des VpU an der Bindung des CD4. Die PRE-Daten deuten darauf hin, dass die Bindung an VpU nicht ausschließlich über die bereits früher identifizierten Aminosäuren 414-419 (LSEKKT) des CD4 erfolgt, sondern ein größerer membrannaher Bereich der zytoplasmatischen Domäne des CD4 beteiligt ist. Zusammenfassend lässt sich feststellen, dass sich die CSP- und PRE-Ergebnisse gegenseitig ergänzen und bestätigen. Die Dissoziationskonstante (K_d) der Wechselwirkung der untersuchten VpU- und CD4-Fragmente liegt im millimolaren Bereich.

Im Mittelpunkt des zweiten Teils dieser Arbeit steht die Entwicklung und Anwendung eines Protokolls für die Charakterisierung der Wechselwirkungen von Membranproteinen mit Hilfe von Nanodisks und Thermophorese („microscale thermophoresis“, MST). Nanodisks sind besonders vorteilhafte Modellmembranen, welche bereits in verschiedenen Bereichen der Biophysik angewendet werden. MST ist eine relativ neue Methode zur Charakterisierung intermolekularer Wechselwirkungen, welche auf der differentiellen Bewegung von Proteinen und ihren Komplexen in einem Temperaturgradienten beruht. MST erfordert nur sehr

geringe Proteinmengen, hat eine sehr hohe Empfindlichkeit und erlaubt die Untersuchung von Wechselwirkungen in Lösung. Protokolle für MST-basierte Untersuchungen wurden für zwei unterschiedliche Typen von Nanodisks entwickelt, welche entweder POPC oder DMPC als Lipid-Hauptkomponente enthalten. Das allgegenwärtige Problem der Adsorption von Nanodisks an die Wände der im MST-Experiment verwendeten Kapillaren konnte durch zwei verschiedene Maßnahmen umgangen werden. Entweder wurden der Nanodisk-Probe bestimmte Additive wie Detergenzien oder BSA zugesetzt oder die Nanodisk-Probe wurde durch eine Kernspurmembran gefiltert. Mit Hilfe des entwickelten Protokolls wurde die Wechselwirkung von Nef mit CD4 sowie die Interaktion zwischen den HIV-Proteinen Vpr und p6 untersucht, wobei jeweils ein Interaktionspartner in der Nanodisk verankert war.

6 Appendix

Abbreviations

AIDS	Acquired immunodeficiency syndrome
βTrCP	B-transducin repeat containing protein
B_0	External magnetic field
CA	Capsid protein
CARA	Computer Aided Resonance Assignment
CCR5	Chemokine receptor type 5
CD4	Cluster of differentiation 4
CSP	Chemical shift perturbation
D_2O	Deuterium oxide
Da	Dalton (molecular mass unit for biopolymers)
DNA	Deoxyribonucleic acid
DPC	Dodecylphosphocholine
DTT	Dithiothreitol
E. coli	*Escherichia coli*
EDTA	Ethylenediamine tetraacetic acid
Env	Envelope
ER	Endoplasmic reticulum
ESI	Electrospray ionization
et al.	et allis
FCS	Fluorescence correlation spectroscopy

FA	Fluorescence anisotropy
FID	Free induction decay
FPLC	Fast protein liquid chromatography
g	Gravitational acceleration
gag	Group specific antigen
GPI	Glycosylphosphatidylinositol
GSH-sepharose	Glutathione sepharose
GST	Glutathione-S-transferase
His	Oligohistidine tag
HIV	Human immunodeficiency virus
HPLC	High performance liquid chromatography
HSQC	Heteronuclear single quantum coherence
Hz	Hertz
IN	Integrase
IMP	Integral membrane protein
IPTG	Isopropyl-β-D-thiogalactopyranoside
ITC	Isothermal titration calorimetry
K_d	Dissociation constant
kDa	Kilodalton
LB	Lysogeny broth
Lck	Lymphocyte-specific protein tyrosine kinase
M	Molar (mole/litre)
M9	Minimal medium for isotope labelling
mA	Milliampere
mAU	Milli-absorbance unit

MSP	Membrane scaffold protein
MST	Microscale thermophoresis
MWCO	Molecular weight cut off
Nef	Negative factor
NMR	Nuclear magnetic resonance
Ni-NTA	Nickel nitrilotriacetic acid
NC	Nucleocapsid protein
OD_{600}	Optical density at a wavelength of 600 nm
PAGE	Polyacrylamide gel electrophoresis
PDB	Protein data bank
POPC	1-palmitoyl-2-oleoyl-*sn*-glycero-3-phosphocholine
ppm	Parts per million
PRE	Paramagnetic relaxation enhancement
PR	Protease
Rev	Regulator of expression of virion proteins
RF	Radio frequency
RNA	Ribonucleic acid
rpm	Rotations per minute
RT	Reverse transcriptase
SDS	Sodium dodecyl sulphate
SPR	Surface plasmon resonance
Tat	Transactivator of transcription
TEV	Tobacco etch virus
TFA	Trifluoroacetic acid
TM	Transmembrane protein

Tris	Tris(hydroxymethyl)-aminomethane
UV	Ultraviolet
v/v	Volume per volume
vif	Viral infectivity factor
Vpr	Virus protein R
VpU	Virus protein U
w/v	Weight per volume

List of tables

Table	Description	Page Number
Table 1	List of chemicals used	19
Table 2	List of enzymes and synthetic peptides	21
Table 3	List of bacterial strains used	21
Table 4	List of vectors used for cloning and expression	22
Table 5	Composition of M9 medium	23
Table 6	List of standard laboratory and miscellaneous equipment	25
Table 7	List of consumables	26
Table 8	List of columns used	27
Table 9	List of software used	28
Table 10	Buffers used for DNA gel electrophoresis	30
Table 11	Components of SDS-PAGE	31
Table 12	List of additives used in MST experiments	43
Table 13	Types of nanodiscs produced, and their relevant properties	66
Table 14	List of optimized parameters established for studying POPC-Atto 647N and DMPC-Atto 488 nanodiscs	73

List of figures

Figure	Description	Page Number
Figure 1	Structure and genome organization of HIV-1	2
Figure 2	Solution NMR structure of VpUcyt	4
Figure 3	Schematic representation of a secondary and tertiary structure model of tetherin.	5
Figure 4	Thermogravitational column	10
Figure 5	Submarine hydrothermal vent; Schematic representation of thermal diffusion-induced concentration of oleic acid	11
Figure 6	Setup for recording microscale thermophoresis	15
Figure 7	A typical thermophoretic signal showing positive thermophoresis	16
Figure 8	Individual steps in MSP purification	34
Figure 9	Steps involved in the purification of CD4mut and HisUbiquitinCD4mut	36
Figure 10	Individual steps involved in Nef purification	38
Figure 11	Individual steps involved in VpUcyt purification	39
Figure 12	Positions of the spin labels in the CD4mut amino acid sequence	49
Figure 13	SDS page to track CD4mut purification	51
Figure 14	Chromatographic steps involved in CD4mut purification	52
Figure 15	Confirming MTSL labelling of the CD4 single cysteine mutants using ESI mass spectrometry	54
Figure 16	SDS-PAGE to track Nef purification	55
Figure 17	SDS-PAGE to track VpUcyt purification	56
Figure 18	Reverse phase chromatography to obtain pure VpUcyt	56
Figure 19	SDS-PAGE to track MSP purification	57

Figure 20	$^{1}H,^{15}N$ HSQC spectrum of ^{15}N VpUcyt, recorded in the presence of membrane mimicking DPC micelles	58
Figure 21	Chemical shift perturbation's (CSPs) of VpUcyt residues at maximum CD4 concentration (1 mM)	60
Figure 22	Shift of the E69 cross-peak of VpUcyt in $^{1}H,^{15}N$-HSQC spectra	61
Figure 23	$^{1}H,^{15}N$ HSQC spectrum of ^{15}N-VpUcyt showing the PRE effect.	62
Figure 24	Quantification of PRE effect	63
Figure 25	Size exclusion chromatography for the separation of CD4mut loaded POPC-Atto 647N nanodiscs	65
Figure 26	Adsorption of POPC-Atto 647N nanodiscs to standard capillaries	69
Figure 27	Effect of SDS on nanodisc adsorption to capillary walls	70
Figure 28	Effect of filtration on nanodisc adsorption to capillary walls	71
Figure 29	Effect of laser power on data quality	72
Figure 30	Interaction of Nef with HisUbiquitinCD4mut-loaded, and unloaded POPC-Atto 647N nanodiscs	75
Figure 31	Interaction of Vpr-loaded DMPC-Atto 488 nanodiscs and the soluble p6 peptide	76
Figure 32	Plot of chemical shift perturbation with respect to the secondary structure of VpUcyt	79
Figure 33	Solution NMR structure of VpUcyt in presence of membrane mimicking DPC micelles	80
Figure 34	Strategy for monitoring the interaction between CD4mut and VpUcyt in DPC micelles by PRE experiments	82
Figure 35	Comparison of intensities for VpUcyt peak resonances in the presence of reduced (Red) and oxidized (Blue) PRE labelled CD4, as a function of residue number	84
Figure 36	Possible model for VpU mediated CD4 degradation	89
Figure 37	MST-based binding isotherm recorded with 50 nM POPC-Atto 647N nanodiscs loaded with HisUbiquitinCD4mut and varying amounts of Nef.	95

Posters and Publications

Publications

Ma, P., Mohrluder, J., Schwarten, M., Stoldt, M., Singh, S. K., Hartmann, R., Pacheco, V., and Willbold, D. (2010). Preparation of a functional GABARAP-lipid conjugate in nanodiscs and its investigation by solution NMR spectroscopy, Chembiochem: a European journal of chemical biology 11, 1967-1970.

Singh, S K., Möckel, L., Thiagarajan, P., Wittlich, M., König, B.W., Willbold, D.,. Mapping the interaction between the cytoplasmic domains of HIV-1 VpU and human CD4 by NMR spectroscopy. *The FEBS journal 279*, 3705-3714.

Posters

Structural details of the interaction of human CD4 and the HIV-1 accessory protein VpU. Luis Möckel, Sameer K. Singh, Pallavi Thiagarajan, Marc Wittlich, Dieter Willbold, Bernd W. Koenig. Presented at the German Biophysical Society Meeting, Bochum, 2010

Characterizing the Interaction of Human CD4 and the HIV-1 Accessory Protein Vpu using Liquid State NMR. Sameer K. Singh, Luis Möckel, Marc Wittlich, Dieter Willbold, Bernd W. Koenig. Presented at the Annual Meeting of the Biophysical Society, Baltimore, 2011.

7 Bibliography

1. Briggs, J. A., Wilk, T., Welker, R., Krausslich, H. G., and Fuller, S. D. (2003) Structural organization of authentic, mature HIV-1 virions and cores, *The EMBO journal 22*, 1707-1715.
2. Coffin, J. M., Hughes, S. H., and Varmus, H. E. (1997) The Interactions of Retroviruses and their Hosts, In *Retroviruses* (Coffin, J. M., Hughes, S. H., and Varmus, H. E., Eds.), Cold Spring Harbor (NY).
3. Frankel, A. D., and Young, J. A. (1998) HIV-1: fifteen proteins and an RNA, *Annual review of biochemistry 67*, 1-25.
4. Watts, J. M., Dang, K. K., Gorelick, R. J., Leonard, C. W., Bess, J. W., Jr., Swanstrom, R., Burch, C. L., and Weeks, K. M. (2009) Architecture and secondary structure of an entire HIV-1 RNA genome, *Nature 460*, 711-716.
5. Malim, M. H., and Emerman, M. (2008) HIV-1 accessory proteins--ensuring viral survival in a hostile environment, *Cell host & microbe 3*, 388-398.
6. Veillette, A., Bookman, M. A., Horak, E. M., and Bolen, J. B. (1988) The CD4 and CD8 T cell surface antigens are associated with the internal membrane tyrosine-protein kinase p56lck, *Cell 55*, 301-308.
7. Rudd, C. E., Trevillyan, J. M., Dasgupta, J. D., Wong, L. L., and Schlossman, S. F. (1988) The CD4 receptor is complexed in detergent lysates to a protein-tyrosine kinase (pp58) from human T lymphocytes, *Proceedings of the National Academy of Sciences of the United States of America 85*, 5190-5194.
8. Dalgleish, A. G., Beverley, P. C., Clapham, P. R., Crawford, D. H., Greaves, M. F., and Weiss, R. A. (1984) The CD4 (T4) antigen is an essential component of the receptor for the AIDS retrovirus, *Nature 312*, 763-767.
9. Kwong, P. D., Wyatt, R., Robinson, J., Sweet, R. W., Sodroski, J., and Hendrickson, W. A. (1998) Structure of an HIV gp120 envelope glycoprotein in complex with the CD4 receptor and a neutralizing human antibody, *Nature 393*, 648-659.
10. Berger, E. A., Murphy, P. M., and Farber, J. M. (1999) Chemokine receptors as HIV-1 coreceptors: roles in viral entry, tropism, and disease, *Annual review of immunology 17*, 657-700.
11. Wyatt, R., and Sodroski, J. (1998) The HIV-1 envelope glycoproteins: fusogens, antigens, and immunogens, *Science 280*, 1884-1888.
12. Buonocore, L., and Rose, J. K. (1993) Blockade of human immunodeficiency virus type 1 production in CD4+ T cells by an intracellular CD4 expressed under control of the viral long terminal repeat, *Proceedings of the National Academy of Sciences of the United States of America 90*, 2695-2699.
13. Crise, B., Buonocore, L., and Rose, J. K. (1990) CD4 is retained in the endoplasmic reticulum by the human immunodeficiency virus type 1 glycoprotein precursor, *Journal of virology 64*, 5585-5593.
14. Jabbar, M. A., and Nayak, D. P. (1990) Intracellular interaction of human immunodeficiency virus type 1 (ARV-2) envelope glycoprotein gp160 with CD4 blocks the movement and maturation of CD4 to the plasma membrane, *Journal of virology 64*, 6297-6304.
15. Stevenson, M., Meier, C., Mann, A. M., Chapman, N., and Wasiak, A. (1988) Envelope glycoprotein of HIV induces interference and cytolysis resistance in CD4+ cells: mechanism for persistence in AIDS, *Cell 53*, 483-496.
16. Wildum, S., Schindler, M., Munch, J., and Kirchhoff, F. (2006) Contribution of Vpu, Env, and Nef to CD4 down-modulation and resistance of human immunodeficiency virus type 1-infected T cells to superinfection, *Journal of virology 80*, 8047-8059.

17. Cohen, E. A., Terwilliger, E. F., Sodroski, J. G., and Haseltine, W. A. (1988) Identification of a protein encoded by the vpu gene of HIV-1, *Nature 334*, 532-534.
18. Strebel, K., Klimkait, T., and Martin, M. A. (1988) A novel gene of HIV-1, vpu, and its 16-kilodalton product, *Science 241*, 1221-1223.
19. Park, S. H., De Angelis, A. A., Nevzorov, A. A., Wu, C. H., and Opella, S. J. (2006) Three-dimensional structure of the transmembrane domain of Vpu from HIV-1 in aligned phospholipid bicelles, *Biophys J 91*, 3032-3042.
20. Ma, C., Marassi, F. M., Jones, D. H., Straus, S. K., Bour, S., Strebel, K., Schubert, U., Oblatt-Montal, M., Montal, M., and Opella, S. J. (2002) Expression, purification, and activities of full-length and truncated versions of the integral membrane protein Vpu from HIV-1, *Protein Sci. 11*, 546-557.
21. Wittlich, M., Koenig, B. W., Stoldt, M., Schmidt, H., and Willbold, D. (2009) NMR structural characterization of HIV-1 virus protein U cytoplasmic domain in the presence of dodecylphosphatidylcholine micelles, *The FEBS journal 276*, 6560-6575.
22. Federau, T., Schubert, U., Flossdorf, J., Henklein, P., Schomburg, D., and Wray, V. (1996) Solution structure of the cytoplasmic domain of the human immunodeficiency virus type 1 encoded virus protein U (Vpu), *Int.J.Pept.Protein Res. 47*, 297-310.
23. Willbold, D., Hoffmann, S., and Rösch, P. (1997) Secondary structure and tertiary fold of the human immunodeficiency virus protein U (Vpu) cytoplasmic domain in solution, *Eur.J.Biochem. 245*, 581-588.
24. Wittlich M, K. B., Stoldt M, Schmidt H, Willbold D. (2009) PDB ID: 2k7y NMR structural characterization of HIV-1 virus protein U cytoplasmic domain in the presence of dodecylphosphatidylcholine micelles., *The FEBS journal 276*, 6560-6575

25. Lenburg, M. E., and Landau, N. R. (1993) Vpu-induced degradation of CD4: requirement for specific amino acid residues in the cytoplasmic domain of CD4, *J.Virol. 67*, 7238-7245.
26. Vincent, M. J., Raja, N. U., and Jabbar, M. A. (1993) Human immunodeficiency virus type 1 Vpu protein induces degradation of chimeric envelope glycoproteins bearing the cytoplasmic and anchor domains of CD4: role of the cytoplasmic domain in Vpu-induced degradation in the endoplasmic reticulum, *J.Virol. 67*, 5538-5549.
27. Willey, R. L., Buckler-White, A., and Strebel, K. (1994) Sequences present in the cytoplasmic domain of CD4 are necessary and sufficient to confer sensitivity to the human immunodeficiency virus type 1 Vpu protein, *Journal of virology 68*, 1207-1212.
28. Yao, X. J., Friborg, J., Checroune, F., Gratton, S., Boisvert, F., Sekaly, R. P., and Cohen, E. A. (1995) Degradation of CD4 induced by human immunodeficiency virus type 1 Vpu protein: a predicted alpha-helix structure in the proximal cytoplasmic region of CD4 contributes to Vpu sensitivity, *Virology 209*, 615-623.
29. Magadan, J. G., and Bonifacino, J. S. (2011) Transmembrane Domain Determinants of CD4 Downregulation, by HIV-1 Vpu, *J Virol*.
30. Binette, J., Dube, M., Mercier, J., Halawani, D., Latterich, M., and Cohen, E. A. (2007) Requirements for the selective degradation of CD4 receptor molecules by the human immunodeficiency virus type 1 Vpu protein in the endoplasmic reticulum, *Retrovirology 4*, 75.
31. Neil, S. J., Zang, T., and Bieniasz, P. D. (2008) Tetherin inhibits retrovirus release and is antagonized by HIV-1 Vpu, *Nature 451*, 425-430.
32. Van Damme, N., Goff, D., Katsura, C., Jorgenson, R. L., Mitchell, R., Johnson, M. C., Stephens, E. B., and Guatelli, J. (2008) The interferon-induced protein BST-2 restricts HIV-1 release and is downregulated from the cell surface by the viral Vpu protein, *Cell host & microbe 3*, 245-252.
33. Hammonds, J., Wang, J. J., Yi, H., and Spearman, P. (2010) Immunoelectron microscopic evidence for Tetherin/BST2 as the physical bridge between HIV-1 virions and the plasma membrane, *PLoS pathogens 6*, e1000749.

34. Fitzpatrick, K., Skasko, M., Deerinck, T. J., Crum, J., Ellisman, M. H., and Guatelli, J. (2010) Direct restriction of virus release and incorporation of the interferon-induced protein BST-2 into HIV-1 particles, *PLoS pathogens 6*, e1000701.
35. Dube, M., Roy, B. B., Guiot-Guillain, P., Binette, J., Mercier, J., Chiasson, A., and Cohen, E. A. (2010) Antagonism of tetherin restriction of HIV-1 release by Vpu involves binding and sequestration of the restriction factor in a perinuclear compartment, *PLoS pathogens 6*, e1000856.
36. Rong, L., Zhang, J., Lu, J., Pan, Q., Lorgeoux, R. P., Aloysius, C., Guo, F., Liu, S. L., Wainberg, M. A., and Liang, C. (2009) The transmembrane domain of BST-2 determines its sensitivity to down-modulation by human immunodeficiency virus type 1 Vpu, *Journal of virology 83*, 7536-7546.
37. Vigan, R., and Neil, S. J. (2010) Determinants of tetherin antagonism in the transmembrane domain of the human immunodeficiency virus type 1 Vpu protein, *Journal of virology 84*, 12958-12970.
38. Kobayashi, T., Ode, H., Yoshida, T., Sato, K., Gee, P., Yamamoto, S. P., Ebina, H., Strebel, K., Sato, H., and Koyanagi, Y. (2011) Identification of amino acids in the human tetherin transmembrane domain responsible for HIV-1 Vpu interaction and susceptibility, *Journal of virology 85*, 932-945.
39. Banning, C., Votteler, J., Hoffmann, D., Koppensteiner, H., Warmer, M., Reimer, R., Kirchhoff, F., Schubert, U., Hauber, J., and Schindler, M. (2010) A flow cytometry-based FRET assay to identify and analyse protein-protein interactions in living cells, *PloS one 5*, e9344.
40. Douglas, J. L., Viswanathan, K., McCarroll, M. N., Gustin, J. K., Fruh, K., and Moses, A. V. (2009) Vpu directs the degradation of the human immunodeficiency virus restriction factor BST-2/Tetherin via a {beta}TrCP-dependent mechanism, *Journal of virology 83*, 7931-7947.
41. Pardieu, C., Vigan, R., Wilson, S. J., Calvi, A., Zang, T., Bieniasz, P., Kellam, P., Towers, G. J., and Neil, S. J. (2010) The RING-CH ligase K5 antagonizes restriction of KSHV and HIV-1 particle release by mediating ubiquitin-dependent endosomal degradation of tetherin, *PLoS pathogens 6*, e1000843.
42. Hauser, H., Lopez, L. A., Yang, S. J., Oldenburg, J. E., Exline, C. M., Guatelli, J. C., and Cannon, P. M. (2010) HIV-1 Vpu and HIV-2 Env counteract BST-2/tetherin by sequestration in a perinuclear compartment, *Retrovirology 7*, 51.
43. Kupzig, S., Korolchuk, V., Rollason, R., Sugden, A., Wilde, A., and Banting, G. (2003) Bst-2/HM1.24 is a raft-associated apical membrane protein with an unusual topology, *Traffic 4*, 694-709.
44. Rollason, R., Korolchuk, V., Hamilton, C., Schu, P., and Banting, G. (2007) Clathrin-mediated endocytosis of a lipid-raft-associated protein is mediated through a dual tyrosine motif, *Journal of cell science 120*, 3850-3858.
45. Hinz, A., Miguet, N., Natrajan, G., Usami, Y., Yamanaka, H., Renesto, P., Hartlieb, B., McCarthy, A. A., Simorre, J. P., Gottlinger, H., and Weissenhorn, W. (2010) Structural basis of HIV-1 tethering to membranes by the BST-2/tetherin ectodomain, *Cell host & microbe 7*, 314-323.
46. Schubert, H. L., Zhai, Q., Sandrin, V., Eckert, D. M., Garcia-Maya, M., Saul, L., Sundquist, W. I., Steiner, R. A., and Hill, C. P. (2010) Structural and functional studies on the extracellular domain of BST2/tetherin in reduced and oxidized conformations, *Proceedings of the National Academy of Sciences of the United States of America 107*, 17951-17956.
47. Yang, H., Wang, J., Jia, X., McNatt, M. W., Zang, T., Pan, B., Meng, W., Wang, H. W., Bieniasz, P. D., and Xiong, Y. (2010) Structural insight into the mechanisms of enveloped virus tethering by tetherin, *Proceedings of the National Academy of Sciences of the United States of America 107*, 18428-18432.
48. Swiecki, M., Scheaffer, S. M., Allaire, M., Fremont, D. H., Colonna, M., and Brett, T. J. (2011) Structural and biophysical analysis of BST-2/tetherin ectodomains reveals an evolutionary conserved design to inhibit virus release, *The Journal of biological chemistry 286*, 2987-2997.

49. Dube, M., Bego, M. G., Paquay, C., and Cohen, E. A. (2010) Modulation of HIV-1-host interaction: role of the Vpu accessory protein, *Retrovirology 7*, 114.
50. Bentham, M., Mazaleyrat, S., and Harris, M. (2006) Role of myristoylation and N-terminal basic residues in membrane association of the human immunodeficiency virus type 1 Nef protein, *The Journal of general virology 87*, 563-571.
51. Gluck, J. M., Hoffmann, S., Koenig, B. W., and Willbold, D. (2010) Single vector system for efficient N-myristoylation of recombinant proteins in E. coli, *PloS one 5*, e10081.
52. Fackler, O. T., and Krausslich, H. G. (2006) Interactions of human retroviruses with the host cell cytoskeleton, *Current opinion in microbiology 9*, 409-415.
53. Aiken, C., Konner, J., Landau, N. R., Lenburg, M. E., and Trono, D. (1994) Nef induces CD4 endocytosis: requirement for a critical dileucine motif in the membrane-proximal CD4 cytoplasmic domain, *Cell 76*, 853-864.
54. daSilva, L. L., Sougrat, R., Burgos, P. V., Janvier, K., Mattera, R., and Bonifacino, J. S. (2009) Human immunodeficiency virus type 1 Nef protein targets CD4 to the multivesicular body pathway, *Journal of virology 83*, 6578-6590.
55. Choi, E. J., and Dimitriadis, E. K. (2004) Cytochrome c adsorption to supported, anionic lipid bilayers studied via atomic force microscopy, *Biophysical journal 87*, 3234-3241.
56. Boutin, J. A. (1997) Myristoylation, *Cellular signalling 9*, 15-35.
57. Zuiderweg, E. R. (2002) Mapping protein-protein interactions in solution by NMR spectroscopy, *Biochemistry 41*, 1-7.
58. Battiste, J. L., and Wagner, G. (2000) Utilization of site-directed spin labeling and high-resolution heteronuclear nuclear magnetic resonance for global fold determination of large proteins with limited nuclear overhauser effect data, *Biochemistry 39*, 5355-5365.
59. Jahnke, W. (2002) Spin labels as a tool to identify and characterize protein-ligand interactions by NMR spectroscopy, *Chembiochem : a European journal of chemical biology 3*, 167-173.
60. Ludwig, C. S. (1856) *Akad. Wiss. Wien: Math.-Naturwiss. 20*, 539.
61. Platten, J. K., and Costeseque, P. (2004) Charles Soret. A short biography on the occasion of the hundredth anniversary of his death, *The European physical journal. E, Soft matter 15*, 235-239.
62. Clusius K, D. G. (1938) *Naturwissenschaften 26*.
63. Duhr, S., and Braun, D. (2006) Why molecules move along a temperature gradient, *Proceedings of the National Academy of Sciences of the United States of America 103*, 19678-19682.
64. S. Iacopini, R. P. (2003) Thermophoresis in protein solutions, *Europhys. Lett. 63*, 247-253.
65. Jerabek-Willemsen, M., Wienken, C. J., Braun, D., Baaske, P., and Duhr, S. (2011) Molecular interaction studies using microscale thermophoresis, *Assay and drug development technologies 9*, 342-353.
66. Schmitt, R. W. (1995) The ocean's salt fingers, *Scientific American 272*, 70-75.
67. H., B. F. (1989) *Mantle Convection: Plate Tectonics and Global Dynamics edited by Peltier W. R., Gordon and Breach Science Publishers.*
68. Braun, D., and Libchaber, A. (2004) Thermal force approach to molecular evolution, *Physical biology 1*, P1-8.
69. Lippok, S., Seidel, S. A., Duhr, S., Uhland, K., Holthoff, H. P., Jenne, D., and Braun, D. (2012) Direct detection of antibody concentration and affinity in human serum using microscale thermophoresis, *Analytical chemistry 84*, 3523-3530.
70. Wienken, C. J., Baaske, P., Rothbauer, U., Braun, D., and Duhr, S. (2010) Protein-binding assays in biological liquids using microscale thermophoresis, *Nature communications 1*, 100.
71. van den Bogaart, G., Meyenberg, K., Diederichsen, U., and Jahn, R. (2012) Phosphatidylinositol 4,5-Bisphosphate Increases Ca2+ Affinity of Synaptotagmin-1 by 40-fold, *The Journal of biological chemistry 287*, 16447-16453.

72. Zillner, K., Jerabek-Willemsen, M., Duhr, S., Braun, D., Langst, G., and Baaske, P. (2012) Microscale thermophoresis as a sensitive method to quantify protein: nucleic acid interactions in solution, *Methods in molecular biology 815*, 241-252.
73. Baaske, P., Weinert, F. M., Duhr, S., Lemke, K. H., Russell, M. J., and Braun, D. (2007) Extreme accumulation of nucleotides in simulated hydrothermal pore systems, *Proceedings of the National Academy of Sciences of the United States of America 104*, 9346-9351.
74. Weinert, F. M., Mast, C. B., and Braun, D. (2011) Optical fluid and biomolecule transport with thermal fields, *Physical chemistry chemical physics : PCCP 13*, 9918-9928.
75. Budin, I., Bruckner, R. J., and Szostak, J. W. (2009) Formation of protocell-like vesicles in a thermal diffusion column, *Journal of the American Chemical Society 131*, 9628-9629.
76. Braun, D., and Libchaber, A. (2002) Trapping of DNA by thermophoretic depletion and convection, *Physical review letters 89*, 188103.
77. Mansy, S. S., Schrum, J. P., Krishnamurthy, M., Tobe, S., Treco, D. A., and Szostak, J. W. (2008) Template-directed synthesis of a genetic polymer in a model protocell, *Nature 454*, 122-125.
78. Duhr, S., Arduini, S., and Braun, D. (2004) Thermophoresis of DNA determined by microfluidic fluorescence, *The European physical journal. E, Soft matter 15*, 277-286.
79. Duhr, S., Braun, D. (2005) Two-dimensional colloidal crystals formed by thermophoresis and convection *Applied physics letters 86*, 131921.
80. Duhr, S., and Braun, D. (2006) Thermophoretic depletion follows Boltzmann distribution, *Physical review letters 96*, 168301.
81. Myszka, D. G., Jonsen, M. D., and Graves, B. J. (1998) Equilibrium analysis of high affinity interactions using BIACORE, *Analytical biochemistry 265*, 326-330.
82. Folker, E. S., Baker, B. M., and Goodson, H. V. (2005) Interactions between CLIP-170, tubulin, and microtubules: implications for the mechanism of Clip-170 plus-end tracking behavior, *Molecular biology of the cell 16*, 5373-5384.
83. GmbH, N. T. (2011) *Monolith NT.115 User Manual*.
84. Nanotemper Technologies, G. Some like it hot: Biomolecule Analytics using Microscale Thermophoresis.
85. Gluck, J. M., Wittlich, M., Feuerstein, S., Hoffmann, S., Willbold, D., and Koenig, B. W. (2009) Integral membrane proteins in nanodiscs can be studied by solution NMR spectroscopy, *Journal of the American Chemical Society 131*, 12060-12061.
86. Sanders, C. R., and Sonnichsen, F. (2006) Solution NMR of membrane proteins: practice and challenges, *Magnetic resonance in chemistry : MRC 44 Spec No*, S24-40.
87. Ujwal, R., and Bowie, J. U. (2011) Crystallizing membrane proteins using lipidic bicelles, *Methods 55*, 337-341.
88. Garrett, F. E., Goel, S., Yasul, J., and Koch, R. A. (1999) Liposomes fuse with sperm cells and induce activation by delivery of impermeant agents, *Biochimica et biophysica acta 1417*, 77-88.
89. Bailey, A. L., and Cullis, P. R. (1997) Membrane fusion with cationic liposomes: effects of target membrane lipid composition, *Biochemistry 36*, 1628-1634.
90. Denisov, I. G., Grinkova, Y. V., Lazarides, A. A., and Sligar, S. G. (2004) Directed self-assembly of monodisperse phospholipid bilayer Nanodiscs with controlled size, *Journal of the American Chemical Society 126*, 3477-3487.
91. Bayburt, T. H., Grinkova, Y. V., and Sligar, S. G. (2006) Assembly of single bacteriorhodopsin trimers in bilayer nanodiscs, *Archives of biochemistry and biophysics 450*, 215-222.
92. Mi, L. Z., Grey, M. J., Nishida, N., Walz, T., Lu, C., and Springer, T. A. (2008) Functional and structural stability of the epidermal growth factor receptor in detergent micelles and phospholipid nanodiscs, *Biochemistry 47*, 10314-10323.
93. Baas, B. J., Denisov, I. G., and Sligar, S. G. (2004) Homotropic cooperativity of monomeric cytochrome P450 3A4 in a nanoscale native bilayer environment, *Archives of biochemistry and biophysics 430*, 218-228.

94. Kijac, A. Z., Li, Y., Sligar, S. G., and Rienstra, C. M. (2007) Magic-angle spinning solid-state NMR spectroscopy of nanodisc-embedded human CYP3A4, *Biochemistry 46*, 13696-13703.
95. Gluck, J. M., Koenig, B. W., and Willbold, D. (2011) Nanodiscs allow the use of integral membrane proteins as analytes in surface plasmon resonance studies, *Analytical biochemistry 408*, 46-52.
96. Frauenfeld, J., Gumbart, J., Sluis, E. O., Funes, S., Gartmann, M., Beatrix, B., Mielke, T., Berninghausen, O., Becker, T., Schulten, K., and Beckmann, R. (2011) Cryo-EM structure of the ribosome-SecYE complex in the membrane environment, *Nature structural & molecular biology 18*, 614-621.
97. Katayama, H., Wang, J., Tama, F., Chollet, L., Gogol, E. P., Collier, R. J., and Fisher, M. T. (2010) Three-dimensional structure of the anthrax toxin pore inserted into lipid nanodiscs and lipid vesicles, *Proceedings of the National Academy of Sciences of the United States of America 107*, 3453-3457.
98. Meyer, O., and Schlegel, H. G. (1983) Biology of aerobic carbon monoxide-oxidizing bacteria, *Annual review of microbiology 37*, 277-310.
99. Delaglio, F., Grzesiek, S., Vuister, G. W., Zhu, G., Pfeifer, J., and Bax, A. (1995) NMRPipe: a multidimensional spectral processing system based on UNIX pipes, *Journal of biomolecular NMR 6*, 277-293.
100. Keller, R. L. J. (1996) The Computer Aided Resonance Assignment Tutorial.
101. Sambrook, J., Russel, D.W. (2001) *Molecular Cloning: A Laboratory Manual,*, Cold Spring Harbor Laboratory Press.
102. Laemmli, U. K. (1970) Cleavage of structural proteins during the assembly of the head of bacteriophage T4, *Nature 227*, 680-685.
103. Bayburt, T. H., Grinkova, Y. V., and Sligar, S. G. (2002) Self-assembly of discoidal phospholipid bilayer nanoparticles with membrane scaffold proteins, *Nano Lett 2*, 853-856.
104. Kapust, R. B., Tozser, J., Fox, J. D., Anderson, D. E., Cherry, S., Copeland, T. D., and Waugh, D. S. (2001) Tobacco etch virus protease: mechanism of autolysis and rational design of stable mutants with wild-type catalytic proficiency, *Protein Eng 14*, 993-1000.
105. Glück JM. (2010) Ligand Interaction Analysis of Membrane-anchored Proteins, p 87, Heinrich Heine University, Düsseldorf.
106. Wittlich, M., Wiesehan, K., Koenig, B. W., and Willbold, D. (2007) Expression, purification, and membrane reconstitution of a CD4 fragment comprising the transmembrane and cytoplasmic domains of the receptor, *Protein expression and purification 55*, 198-207.
107. Wittlich, M., Koenig, B. W., Hoffmann, S., and Willbold, D. (2007) Structural characterization of the transmembrane and cytoplasmic domains of human CD4, *Biochimica et biophysica acta 1768*, 2949-2960.
108. Wittlich, M., Koenig, B. W., and Willbold, D. (2008) Structural consequences of phosphorylation of two serine residues in the cytoplasmic domain of HIV-1 VpU, *Journal of peptide science : an official publication of the European Peptide Society 14*, 804-810.
109. Jacobsen, N. E. (2007) *NMR Spectroscopy Explained: Simplified Theory, Applications and Examples for Organic Chemistry and Structural Biology*, Wiley-Interscience; 1 edition.
110. Bodenhausen, G., Ruben, D.J. (1980) Natural abundance nitrogen-15 NMR by enhanced heteronuclear spectroscopy, *Chem Phys Lett. 69*, 185-189.
111. Thielmann, Y., Mohrluder, J., Koenig, B. W., Stangler, T., Hartmann, R., Becker, K., Holtje, H. D., and Willbold, D. (2008) An indole-binding site is a major determinant of the ligand specificity of the GABA type A receptor-associated protein GABARAP, *Chembiochem : a European journal of chemical biology 9*, 1767-1775.
112. Stevens, S. Y., Sanker, S., Kent, C., and Zuiderweg, E. R. (2001) Delineation of the allosteric mechanism of a cytidylyltransferase exhibiting negative cooperativity, *Nature structural biology 8*, 947-952.

113. Arumugam, S., Hemme, C. L., Yoshida, N., Suzuki, K., Nagase, H., Berjanskii, M., Wu, B., and Van Doren, S. R. (1998) TIMP-1 contact sites and perturbations of stromelysin 1 mapped by NMR and a paramagnetic surface probe, *Biochemistry 37*, 9650-9657.
114. Vaynberg, J., and Qin, J. (2006) Weak protein-protein interactions as probed by NMR spectroscopy, *Trends in biotechnology 24*, 22-27.
115. Zuiderweg, E. R. (2002) Mapping protein-protein interactions in solution by NMR spectroscopy, *Biochemistry 41*, 1-7.
116. Tiganos, E., Yao, X. J., Friborg, J., Daniel, N., and Cohen, E. A. (1997) Putative alpha-helical structures in the human immunodeficiency virus type 1 Vpu protein and CD4 are involved in binding and degradation of the CD4 molecule, *J.Virol. 71*, 4452-4460.
117. Margottin, F., Bour, S. P., Durand, H., Selig, L., Benichou, S., Richard, V., Thomas, D., Strebel, K., and Benarous, R. (1998) A novel human WD protein, h-beta TrCp, that interacts with HIV-1 Vpu connects CD4 to the ER degradation pathway through an F-box motif, *Mol.Cell. 1*, 565-574.
118. Battiste, J. L., and Wagner, G. (2000) Utilization of site-directed spin labeling and high-resolution heteronuclear nuclear magnetic resonance for global fold determination of large proteins with limited nuclear overhauser effect data, *Biochemistry 39*, 5355-5365.
119. Bour, S., Schubert, U., and Strebel, K. (1995) The human immunodeficiency virus type 1 Vpu protein specifically binds to the cytoplasmic domain of CD4: implications for the mechanism of degradation, *Journal of virology 69*, 1510-1520.
120. Lenburg, M. E., and Landau, N. R. (1993) Vpu-induced degradation of CD4: requirement for specific amino acid residues in the cytoplasmic domain of CD4, *Journal of virology 67*, 7238-7245.
121. Vincent, M. J., Raja, N. U., and Jabbar, M. A. (1993) Human immunodeficiency virus type 1 Vpu protein induces degradation of chimeric envelope glycoproteins bearing the cytoplasmic and anchor domains of CD4: role of the cytoplasmic domain in Vpu-induced degradation in the endoplasmic reticulum, *Journal of virology 67*, 5538-5549.
122. Yao, X. J., Friborg, J., Checroune, F., Gratton, S., Boisvert, F., Sekaly, R. P., and Cohen, E. A. (1995) Degradation of CD4 induced by human immunodeficiency virus type 1 Vpu protein: a predicted alpha-helix structure in the proximal cytoplasmic region of CD4 contributes to Vpu sensitivity, *Virology 209*, 615-623.
123. Wittlich, M., Thiagarajan, P., Koenig, B. W., Hartmann, R., and Willbold, D. (2010) NMR structure of the transmembrane and cytoplasmic domains of human CD4 in micelles, *Biochim Biophys Acta 1798*, 122-127.
124. Mahoney, N. M., Rastogi, V. K., Cahill, S. M., Girvin, M. E., and Almo, S. C. (2000) Binding orientation of proline-rich peptides in solution: Polarity of the profilin-ligand interaction, *Journal of the American Chemical Society 122*, 7851-7852.
125. Mal, T. K., Ikura, M., and Kay, L. E. (2002) The ATCUN domain as a probe of intermolecular interactions: Application to calmodulin-peptide complexes, *Journal of the American Chemical Society 124*, 14002-14003.
126. Chen, M. Y., Maldarelli, F., Karczewski, M. K., Willey, R. L., and Strebel, K. (1993) Human immunodeficiency virus type 1 Vpu protein induces degradation of CD4 in vitro: the cytoplasmic domain of CD4 contributes to Vpu sensitivity, *J.Virol. 67*, 3877-3884.
127. Bour, S., Schubert, U., and Strebel, K. (1995) The human immunodeficiency virus type 1 Vpu protein specifically binds to the cytoplasmic domain of CD4: implications for the mechanism of degradation, *J.Virol. 69*, 1510-1520.
128. Margottin, F., Benichou, S., Durand, H., Richard, V., Liu, L. X., Gomas, E., and Benarous, R. (1996) Interaction between the cytoplasmic domains of HIV-1 Vpu and CD4: role of Vpu residues involved in CD4 interaction and in vitro CD4 degradation, *Virology 223*, 381-386.
129. Schubert, U., Schneider, T., Henklein, P., Hoffmann, K., Berthold, E., Hauser, H., Pauli, G., and Porstmann, T. (1992) Human-immunodeficiency-virus-type-1-encoded Vpu protein is phosphorylated by casein kinase II, *European journal of biochemistry / FEBS 204*, 875-883.

130. Schubert, U., and Strebel, K. (1994) Differential activities of the human immunodeficiency virus type 1-encoded Vpu protein are regulated by phosphorylation and occur in different cellular compartments, *Journal of virology 68*, 2260-2271.
131. Schubert, U., Henklein, P., Boldyreff, B., Wingender, E., Strebel, K., and Porstmann, T. (1994) The human immunodeficiency virus type 1 encoded Vpu protein is phosphorylated by casein kinase-2 (CK-2) at positions Ser52 and Ser56 within a predicted alpha-helix-turn-alpha-helix-motif, *Journal of molecular biology 236*, 16-25.
132. Butticaz, C., Michielin, O., Wyniger, J., Telenti, A., and Rothenberger, S. (2007) Silencing of both beta-TrCP1 and HOS (beta-TrCP2) is required to suppress human immunodeficiency virus type 1 Vpu-mediated CD4 down-modulation, *Journal of virology 81*, 1502-1505.
133. Nakayama, K. I., and Nakayama, K. (2006) Ubiquitin ligases: cell-cycle control and cancer, *Nature reviews. Cancer 6*, 369-381.
134. Margottin, F., Bour, S. P., Durand, H., Selig, L., Benichou, S., Richard, V., Thomas, D., Strebel, K., and Benarous, R. (1998) A novel human WD protein, h-beta TrCp, that interacts with HIV-1 Vpu connects CD4 to the ER degradation pathway through an F-box motif, *Molecular cell 1*, 565-574.
135. Stevens, T. J., and Arkin, I. T. (2000) Do more complex organisms have a greater proportion of membrane proteins in their genomes?, *Proteins 39*, 417-420.
136. Mirza, S. P., Halligan, B. D., Greene, A. S., and Olivier, M. (2007) Improved method for the analysis of membrane proteins by mass spectrometry, *Physiological genomics 30*, 89-94.
137. Krogh, A., Larsson, B., von Heijne, G., and Sonnhammer, E. L. (2001) Predicting transmembrane protein topology with a hidden Markov model: application to complete genomes, *Journal of molecular biology 305*, 567-580.
138. McMullen, T. P. W., Lewis, R.N.A.H., McElhaney, R.N. (2004) Cholesterol–phospholipid interactions, the liquid-ordered phase and lipid rafts in model and biological membranes, *Current Opinion in Colloid and Interface Science 8*, 459-468.
139. Kamal, M. M., Mills, D., Grzybek, M., and Howard, J. (2009) Measurement of the membrane curvature preference of phospholipids reveals only weak coupling between lipid shape and leaflet curvature, *Proceedings of the National Academy of Sciences of the United States of America 106*, 22245-22250.
140. Gerlach, H., Laumann, V., Martens, S., Becker, C. F., Goody, R. S., and Geyer, M. (2010) HIV-1 Nef membrane association depends on charge, curvature, composition and sequence, *Nature chemical biology 6*, 46-53.
141. Szilluweit, R., Boll, A., Lukowski, S., Gerlach, H., Fackler, O. T., Geyer, M., and Steinem, C. (2009) HIV-1 Nef perturbs artificial membranes: investigation of the contribution of the myristoyl anchor, *Biophysical journal 96*, 3242-3250.
142. Preusser, A., Briese, L., Baur, A. S., and Willbold, D. (2001) Direct in vitro binding of full-length human immunodeficiency virus type 1 Nef protein to CD4 cytoplasmic domain, *Journal of virology 75*, 3960-3964.
143. Selig, L., Pages, J. C., Tanchou, V., Preveral, S., Berlioz-Torrent, C., Liu, L. X., Erdtmann, L., Darlix, J., Benarous, R., and Benichou, S. (1999) Interaction with the p6 domain of the gag precursor mediates incorporation into virions of Vpr and Vpx proteins from primate lentiviruses, *Journal of virology 73*, 592-600.
144. Salgado, G. F., Marquant, R., Vogel, A., Alves, I. D., Feller, S. E., Morellet, N., and Bouaziz, S. (2009) Structural studies of HIV-1 Gag p6ct and its interaction with Vpr determined by solution nuclear magnetic resonance, *Biochemistry 48*, 2355-2367.
145. Jenkins, Y., Pornillos, O., Rich, R. L., Myszka, D. G., Sundquist, W. I., and Malim, M. H. (2001) Biochemical analyses of the interactions between human immunodeficiency virus type 1 Vpr and p6(Gag), *Journal of virology 75*, 10537-10542.

8 Acknowledgement

I would firstly like to thank Prof. Dr. Dieter Willbold, for giving me the opportunity to work in his group. It's been a great learning experience for me, and for this I am truly grateful.

I would like to thank my supervisor Dr. Bernd König for his constant guidance and support. His knowledge on biophysics has been a real eye opener for me.

I thank Julian for supervising me when I joined the group and for all the help over the years. I thank Justin for all his help with my computer, as well as his assistance with various NMR concepts. Along with Julian and Justin, I would also like to thank Susanne and Dirk for all the good times in the office.

I am especially grateful to Yeliz for the immeasurable amount of help she's given me these past three years...Thank you!

A special thanks to Luis Mökel, for the beer soaked evenings in the Altstadt, Düsseldorf. Let's hope they continue.

I would like to thank Esther, Nicole, Markus and Rene for the great support in the lab. I thank Rudy, Victor, Matthias and Philip for their help with the NMR experiments. I'd like to thank Matteo and Axel from ICS-5, for help with the experiments and also the occasional chats. I thank Pallavi for her immense support and encouragement, and also for bringing a constant cheer to the lab. I'd like to thank Amine, Ellen, Lei, Stephan, Carsten, Silke; it's been very nice getting to know you guys. Off course, there are so many others in the institute that have helped and supported me, and for that I am very thankful. I've also been lucky to have made some good friends in Jülich these past three years. Thank you guys for everything.

I'd like to thank my parents, my brother and my close friends Akshay and Girish.

Finally, I'd like to thank circumstances, luck, karma, or whatever one wants to call them. They have always been helpful.

9 EIDESSTATTLICHE ERKLÄRUNG

Hiermit versichere ich, dass ich meine Dissertation ohne Hilfe Dritter und ohne Benutzung anderer als der angegebenen Quellen und Hilfsmittel angefertigt und die den benutzten Quellen wörtlich oder inhaltlich entnommenen Stellen als solche kenntlich gemacht habe. Diese Arbeit hat in gleicher oder ähnlicher Form noch keiner Prüfungsbehörde vorgelegen.

Jülich, den

_____

(Sameer Kumar Singh)